

CALIFORNIA STATE UNIVERSITY, NORTHRIDGE

STUDY OF ELASTIC THICKNESS FROM SEAMOUNT LOADING OF OLD
OCEANIC LITHOSPHERE: IMPLICATIONS FOR LITHOSPHERE STABILITY

Thesis submitted in partial fulfillment of the requirements
for the degree of Master of Science in
Geophysics

By
Cristo Ramirez
December 2011

December 2011

The thesis of Cristo Ramirez is approved by:

Gerry Simila, Ph. D.

Date

Doug Yule, Ph. D.

Date

Dayanthie S. Weeraratne, Ph. D., Chair

Date

California State University Northridge

TABLE OF CONTENTS

Signature Page	ii
List of Figures	v
List of Tables	vii
List of Equations	ix
Abstract	x
Chapter 1: Introduction	1
1.1 Oceanic Lithosphere Characterization	1
Chapter 2: Seafloor Geomorphology	8
2.1 Seamounts	8
2.1.1 Seamounts Used in This Study	8
2.1.2 Small and Clustered Seamounts	11
2.1.3 Large Seamounts	11
2.2 Abyssal Hills	12
2.2.1 Abyssal Hill Geomorphology	12
2.2.2 Hybrid Seamount/Abyssal Hill	15
Chapter 3: Methodology	19
3.1 Map Generation	19
3.2 Seamount Selection	22
3.3 Data Model Parameters	22
3.4 Parameters Obtained	23
3.5 Calculations	25

3.5.1 Volume Calculation	25
3.5.2 Deflection Method	27
3.5.3 Topography Method	31
3.5.4 Error Analysis	32
Chapter 4: Results	34
4.1 Seamount Maps and Volume	34
4.2 Plate Deflection Depth	38
4.3 Elastic Thickness Calculation	39
4.4 Elastic Thickness Observation	41
4.5 Deflection Depths and Other Graphs	42
4.5.1 Deflection Depth	42
4.5.2 Volume and Moat Radius	43
Chapter 5: Discussion	45
5.1 Age Determination	45
5.2 Abyssal Hill Integrity	46
5.3 Larger Perimeter Seamounts	46
Chapter 6: Conclusions	48
6.1 Conclusions	48
6.2 Implications for PLATE Study	48
References	50
APPENDIX A: Seamount Maps	52

APPENDIX B: Deflection Profiles	64
APPENDIX C: Theoretical Seamounts	76
APPENDIX D: Table of Values	88

LIST OF FIGURES

1. Figure 1.1 Regional Map	1
2. Figure 1.2 Seafloor Age	2
3. Figure 1.3 Seafloor Depth	2
4. Figure 1.4 Bathymetry of the Field Area	4
5. Figure 1.5 Western Array	6
6. Figure 1.6 Eastern Array	6
7. Figure 2.1 Small Seamounts	10
8. Figure 2.2 Clustered Seamounts	11
9. Figure 2.3 Large Seamounts	12
10. Figure 2.4 Abyssal Hills	13
11. Figure 2.5 Hill Cross Section	14
12. Figure 2.6 Hybrid Seamounts	15
13. Figure 2.7 Abyssal Hill Formation Models	17
14. Figure 3.1 Single Beam Bathymetry	20
15. Figure 3.2 Schematic Crossection	23
16. Figure 3.3 Moat Detection Extremes	24
17 3.4 Figure 3.4 Cross Section for Volume Calculation	26
18. Figure 3.5 Area for Volume Calculation	27
19. Figure 3.6 Deflection Profile of Seamount #2	28
20. Figure 3.7 Calculated Seamount #2	33
21. Figure 4.1 Seamount #7	35
22. Figure 4.2 Seamount #1	37

23. Figure 4.3 Deflection Profile of Seamount #7	38
24. Figure 4.4 Deflection Profile of Seamount #1	39
25. Figure 4.5 Calculated Seamount #1	40
26. Figure 4.6 Calculated Seamount #7	41
27. Figure 4.7 Volume vs. Elastic Thickness	42
28. Figure 4.8 Volume vs. Deflection Depth	43
30. Figure 4. 10 Moat Radius vs. Deflection Depth	44
31. Figure 5.1 Age Calculation	46

LIST OF TABLES

1. Table 1. Program Parameters

25

LIST OF EQUATIONS

1. Equation 3.1 Deflection Depth	29
2. Equation 3.2 Three Dimensional Parameter	29
3. Equation 3.3 Three Dimensional Parameter II	29
4. Equation 3.4 Load	30
5. Equation 3.5 Moat Radius Error	30
6. Equation 3.6 Deflection Profile	30
7. Equation 3.7 Flexural Parameter	30
8. Equation 3.8 Flexural Rigidity	31
9. Equation 3.9 Seamount Height	31
10. Equation 3.10 Calculated Seamount Profile	32
11. Equation 3.11 Seamount Area Error	32

ABSTRACT

STUDY OF ELASTIC THICKNESS FROM SEAMOUNT LOADING OF OLD OCEANIC LITHOSPHERE: IMPLICATIONS FOR LITHOSPHERE STABILITY

By

Cristo Ramirez

Master of Science in Geophysics

The PLATE (Pacific Lithosphere Anisotropy and Thickness Experiment) study will employ several marine geophysical methods to investigate the natural and undisturbed growth of the lithosphere. The field area was chosen in order to obtain an ideal location where minimal volcanic and tectonic activity had occurred. However, during the field work for the project, several seamounts were found within the area using high resolution shiptrack bathymetry, suggesting volcanic activity. Determining the timing of these volcanic events is crucial to understand the stability over time of the lithosphere.

Calculations from twelve seamounts in the area yielded elastic thicknesses that range from 1.5 to 3.5 km. These elastic thicknesses (T_e) were used to estimate the age of the seafloor at the time in which the seamounts formed. I obtained a lithosphere age of less than 10 m.y. at time of seamount loading. The abyssal hill geomorphology and magnetic lineations provide further support for these results and suggest no major tectonic event. The early loading of the seamounts supports the idea that the lithosphere has grown in a normal undisturbed fashion consistent with conductive cooling for the past 140 Ma, making it an ideal location to study lithospheric growth and test the conductive cooling model in old seafloor. This study provides support for the field area's integrity.

Chapter 1 INTRODUCTION

1.1 Oceanic Lithosphere Characterization

The primary purpose of the PLATE (Pacific Lithosphere Anisotropy and Thickness Experiment) project is to use seismic, gravity, magnetics and geomorphology data to study the way in which the lithosphere forms and thickens over time. The location of the project (Fig. 1.1) on 150 Ma seafloor was chosen because it occurs on lithosphere that is older than 80 Ma (Fig. 1.2), where the square root of age curve for lithospheric cooling and seafloor observations diverge from the observed bathymetry (Fig. 1.3). To study the natural growth and cooling of oceanic lithosphere, the ideal location should be undisturbed by external dynamics such as melting or unusual fracturing during its entire history.

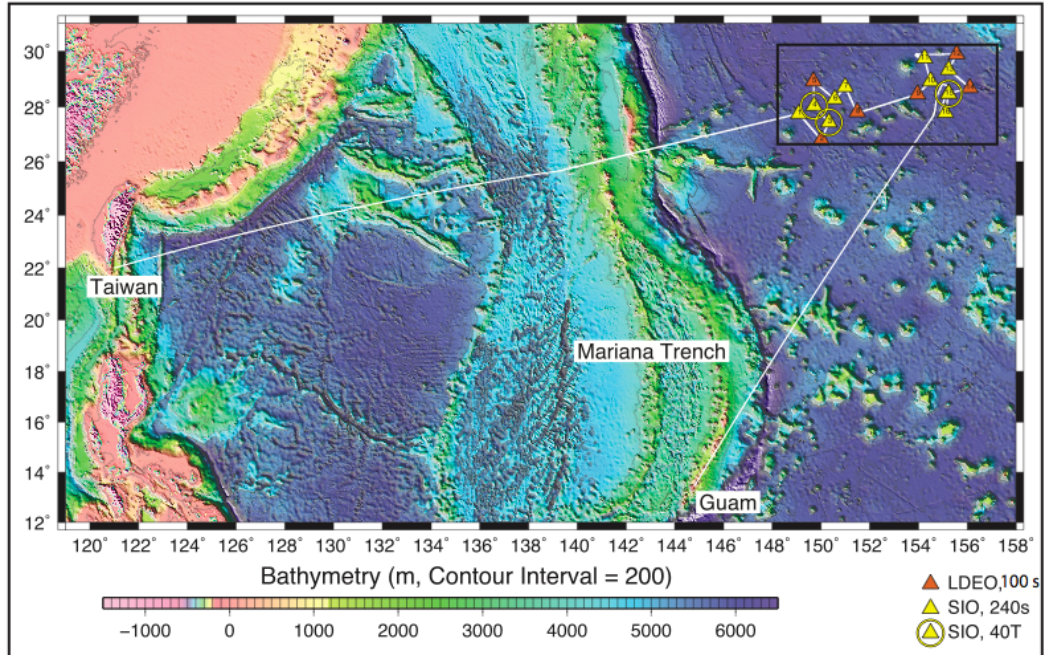


Figure 1.1 Bathymetric map of West Pacific Ocean floor near Mariana trench. The yellow and red triangles represent the two different arrays in which seismometers were deployed and the area where the seamounts used for the study are located. Guam and Taiwan are indicated for easier geographic orientation. The black box indicates the location that is shown in Figure 1.4. White lines indicate our travel path in the deployment cruise. Bathymetric data obtained from Smith and Sandwell, 1997.

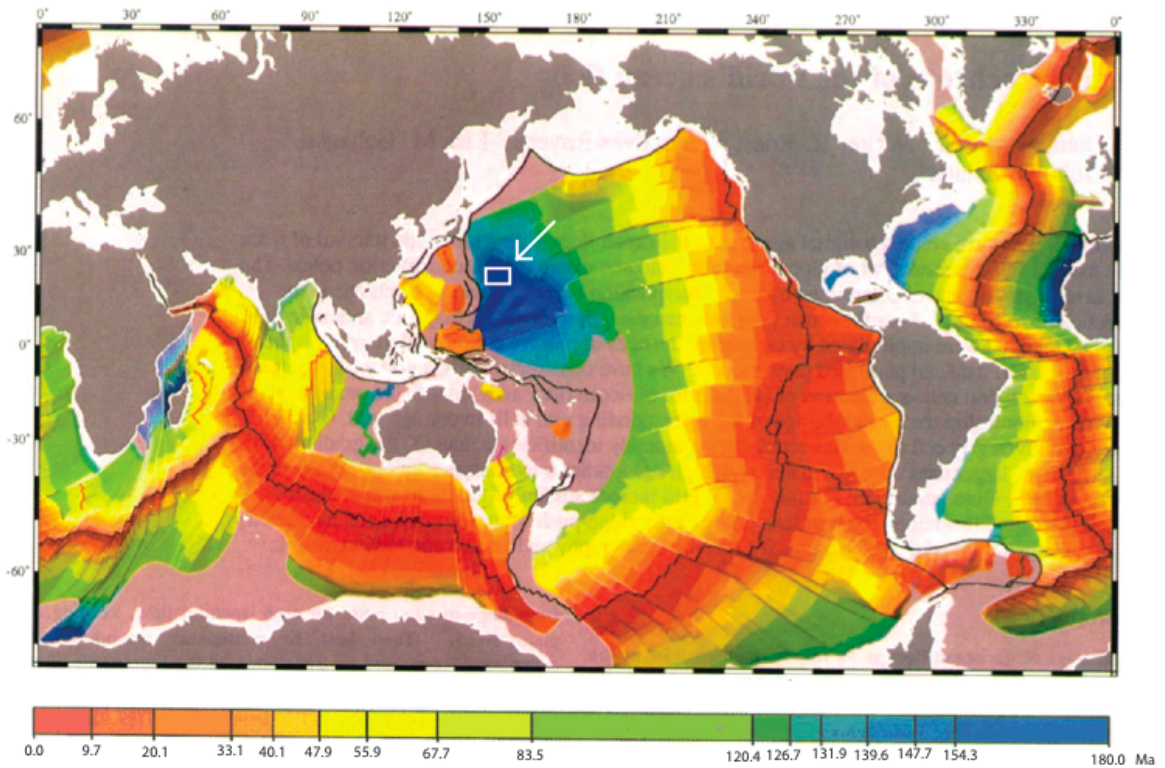


Figure 1.2 World map with colors corresponding to the age of the seafloor. Data was compiled using magnetic anomalies aided by gravity anomalies. The square shows the location of the field area, which corresponds to an age of more than 155Ma. Figure modified from Muller, et al. 1997.

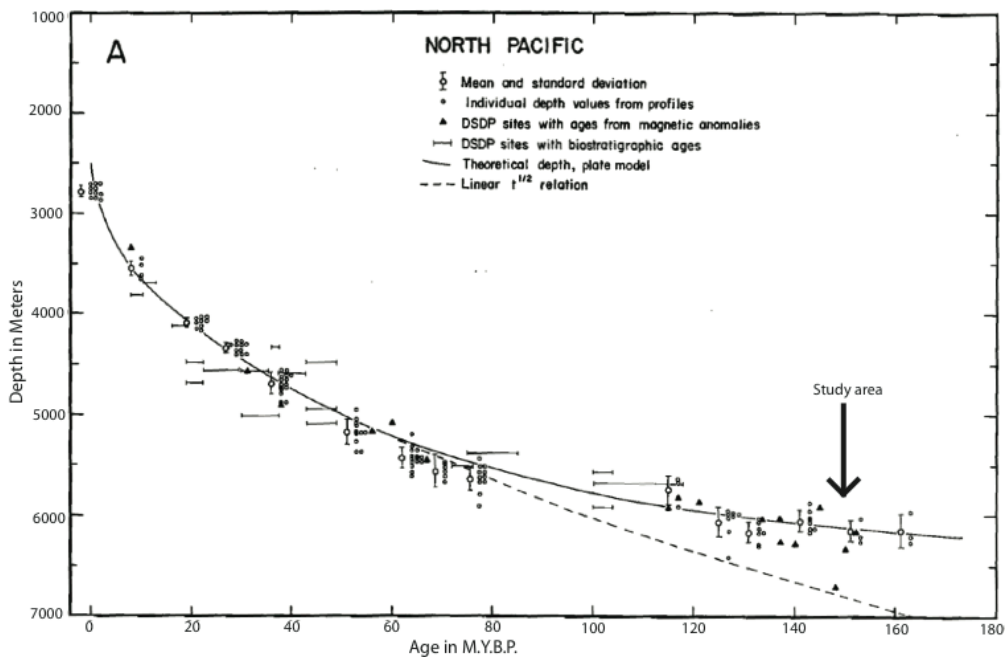


Figure 1.3 The graph shows the relationship between age and depth of the seafloor. Notice that the measured data points begin to stray from the $t^{1/2}$ Ma. Figure modified from Parsons and Sclater, 1997.

High resolution shiptrack bathymetry data were obtained during two research cruises. The objectives of these cruises were to collect geophysical data and to deploy sixteen ocean bottom seismometers. Our chosen location was closest to international ports in Taiwan, Guam and Hawaii. The shiptracks and location of OBS from our deployment and recovery cruises are shown in Figure. 1.4. The chosen study area is located on seafloor older than 80 Ma. High resolution bathymetry coverage revealed two groups of seamounts that suggest volcanic activity in the area (Fig. 1.4). The group of larger seamounts is on the perimeter of our focus study area. These seamounts do not show a flexural moat, thus they cannot be used to determine the elastic thickness. The lack of moat around the large seamounts indicates that these likely formed when the lithosphere was rigid enough to support the load and therefore did not flex. The second group of seamounts is observed throughout our area and consists of significantly smaller seamounts. These smaller seamounts, however, do show flexural moats indicating that these seamounts were emplaced on younger seafloor and thinner lithosphere that responded to the applied load. The goal of my study is to analyze the impact of the seamounts on lithospheric growth over time. I will use loading and plate flexure to determine the elastic thickness of the lithosphere at the time of seamount formation and a range of time in which they were emplaced.

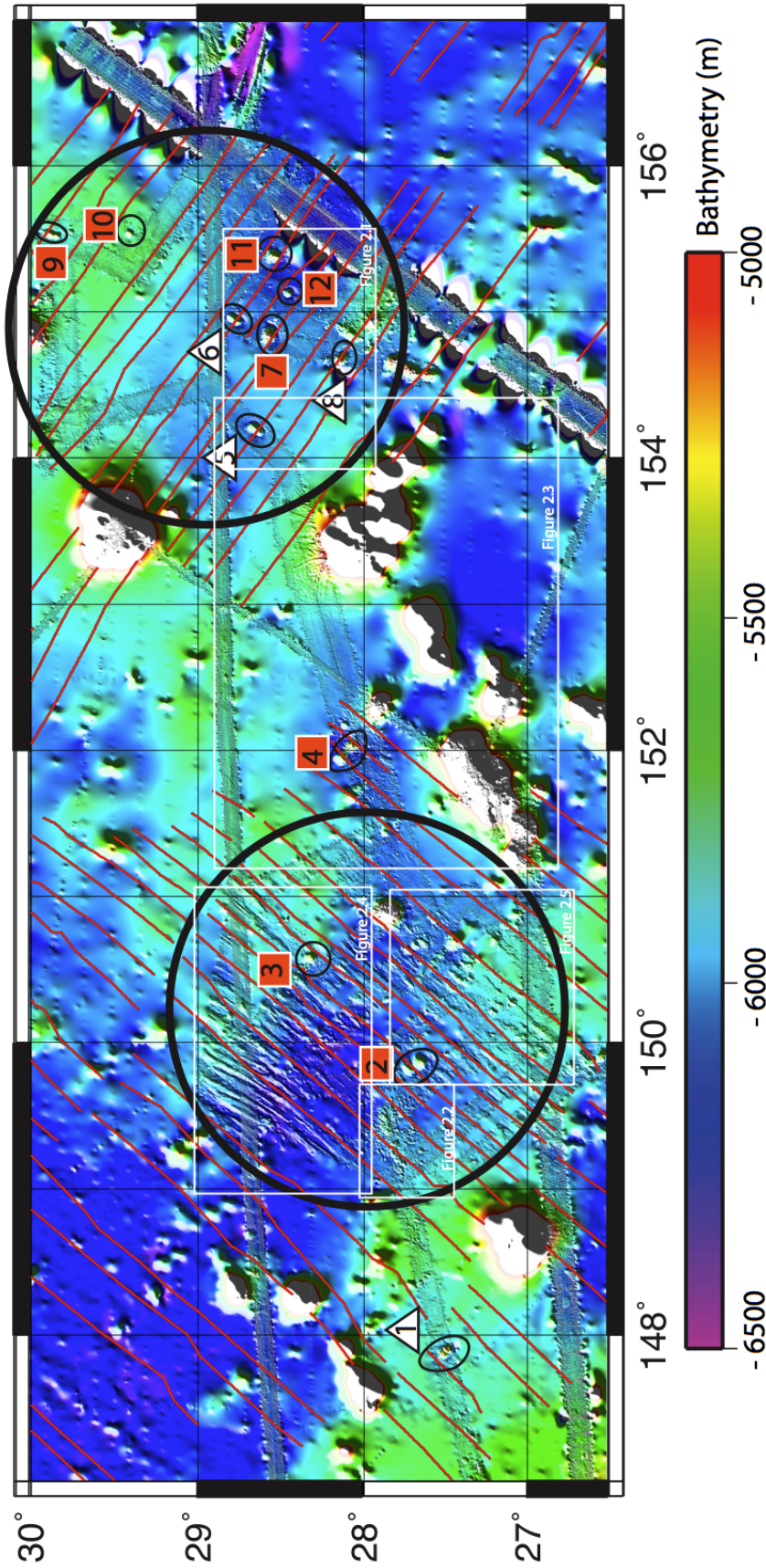


Figure 1.4 Bathymetry of the study area. The large circles indicate the locations where seismometers were deployed. Seamounts used for this study include conical and elliptical (red squares and white triangle respectively). Notice the greater number of seamounts found within the eastern array. Magnetic lineations modified from Nakanishi et al., (1992).

There exist few methods that can help us test the lithospheric cooling hypothesis, and even fewer are easily accessible where seafloor age is old enough to manifest the discrepancy between theory and observation. I use geomorphology of the seafloor along transects of the marine vessel as a means to determine plate loading and flexural response. Seismic data are also available, both active source experiments from previous studies (Oikawa et al., 2010; Shinohara et al., 2008) and passive seismic data recently collected from the ongoing PLATE project. Gravity and geomagnetic data from ship tracks and satellite instruments are also available for this location. Shiptrack bathymetry data provide the highest resolution seafloor data available, but is limited to precision in relatively small and narrow locations dictated by shiptrack swath lines. Bathymetry data can also be inverted from satellite gravity data providing widespread, but imprecise resolution that is dependent on the gravity observations (Smith and Sandwell, 1997). For admittance studies, gravity data from satellite instruments are sufficient, but must be an independent observation from the bathymetry data. Thus, I focus on seamount loading and plate flexure techniques to determine elastic thickness.

In order to maximize the amount of information extracted from the data, the high resolution shiptrack bathymetry was selected and analyzed to obtain the information required by the project. A close look into the geomorphology of the area revealed moats (Appendix A) around some of the seamounts that are within the field area (Fig. 1.4). The moats provide a very important clue to the timing of volcanism and relatively stability of the lithosphere at this location.

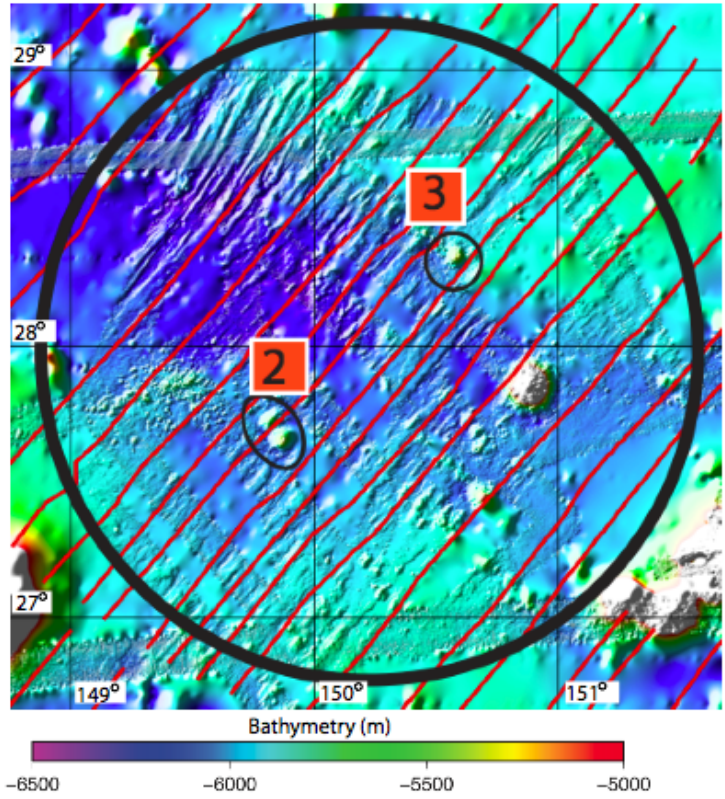


Figure 1.5 Close up view of the western array. Abyssal hills and magnetic lineations are parallel trending NE-SW.

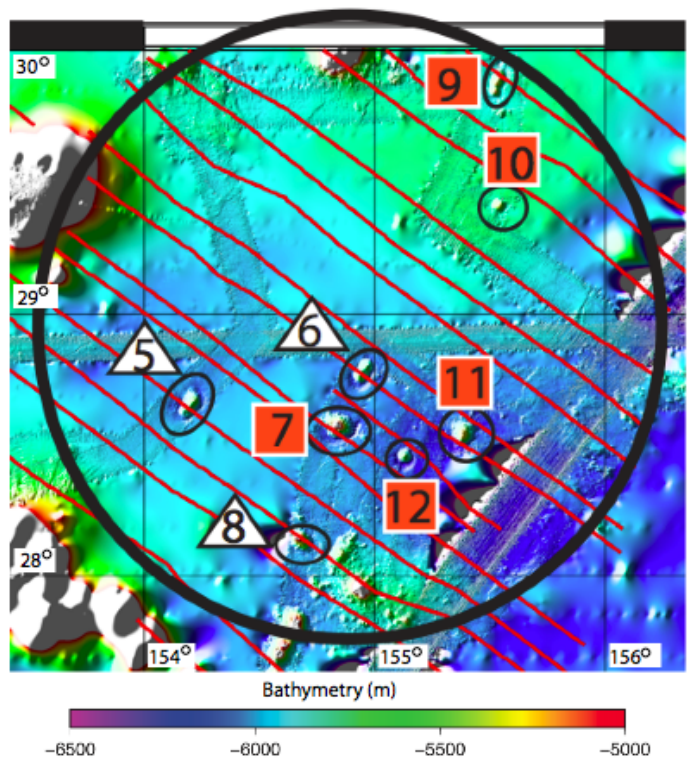


Figure 1.6 Close up version of the eastern array. Notice that most of the seamounts used in this study are located within this part of the field area.

The measured moats were used to calculate the amount of flexing of the lithosphere due to the loading of seamounts on top of it. The flexure created by seamounts is then used to calculate the rigidity and thickness of the plate at the time of loading. The thickness of the lithosphere is of particular importance to the project since an age of the formation of the seamounts can be estimated. The age of the seamounts is significant because it indicates a time in which there was volcanic activity on the plate.

Another objective for this project will be to provide support to the hypothesis that the area has remained tectonically and magmatically inactive for most of its lifespan. I will also be able to determine the extent of flexing and volume filling the depression (w_0 ; Figure, 3.2) of the lithosphere for each seamount, which will be used for crustal thickness assumptions made in the tomographic calculations.

Chapter 2

SEAFLOOR GEOMORPHOLOGY

The field area is located among the oldest oceanic lithosphere in the world with ages circa 150 to 160 Ma based on maps presented by Muller et al. 1997 (Fig. 1.2). The age of the oceanic lithosphere in this area could allow for a long history of many magmatic and tectonic episodes of deformation within the field area. I present results showing that this is not the case. The geomorphology provides clues into the relative stability of the lithosphere in this portion of the Pacific Ocean.

The geomorphology of the area is subdivided into several main features. Each one of these components was derived from careful scrutiny of the high resolution bathymetric data obtained during the field work of the PLATE study. Most of the features provide valuable information indicating uncomplicated magmatic and structural history of this portion of ocean floor.

2.1 Seamounts

I focus on the loading from seamount in this study. To do this, I identify several classes or groups of seamounts in our field area including the focus seamounts of study, large seamounts, and very small, clustered seamounts. I attempt to determine the relative age of each and the impact on lithospheric growth and stability during cooling. I focus our study on group one.

2.1.1 Seamounts Used in This Study

The most important subdivision used was the seamounts that were isolated for the purpose of this study. These seamounts are observed in Figure, 1.4. All twelve of these

seamounts show a prominent moat around them (Figure 2.1). I also find that the shape of the seamounts is not always conical. Geomorphological observations indicate that the seamounts vary from a mostly circular to an elliptical shape. The seamounts that are circular include 2, 3, 4, 7, 9, 10, 11 and 12; whereas, seamounts 1, 5, 6 and 8 show a more elliptical figure (Fig. 1.4). It is clear that most of the elliptical seamounts have at least two distinct peaks instead of a connected ridge as a summit. One peak is usually significantly larger than the other. In this study, I considered elliptical seamounts as a single seamount and therefore their volume was obtained including the mass of both (or multiple) peaks within the seamount with the exception of seamount #9. Seamounts that are more or less circular, but are extremely close to a second seamount, appear to be a single seamount combined with its nearest neighbor. Seamounts 2, 4 and 9 are considered to be circular, but each appears jointly with a small adjacent seamount. In these cases, the main peak is separated from the adjacent neighbor by bathymetry that is at the depth or lower than the base of the seamount (Appendix A, seamounts 2, 4, 9).

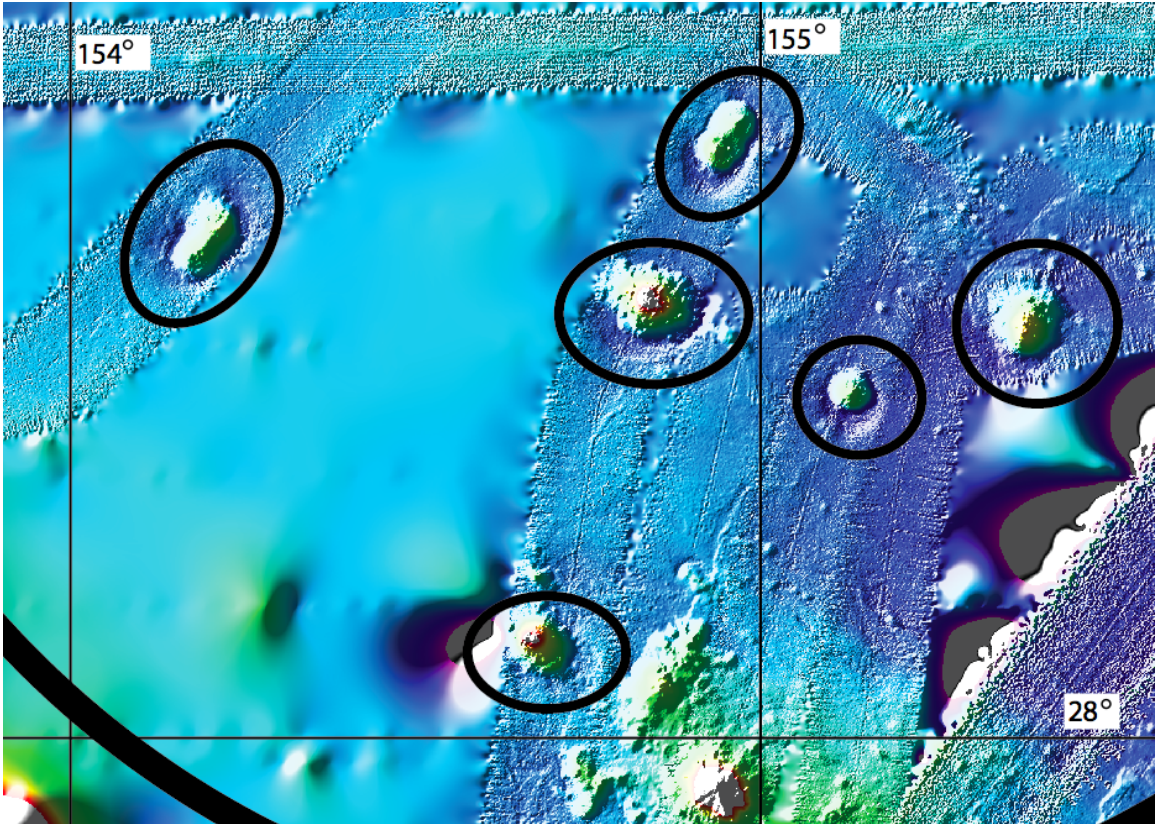


Figure 2.1 Six seamounts out of the twelve used in the study are shown here. They are located within the eastern array. The moats around the seamounts are observed in the darker blues around the seamounts.

The location of the seamounts is highly correlated to the shiptrack bathymetric coverage of the seafloor. The long wavelengths of satellite data coverage simply do not detect the topographic variations from these small seamount features. Though the coverage was limited, it was clear that the seamounts were more abundant in the eastern array (Fig. 1.6) of the seismometers rather than on the western one (Fig. 1.5). The eastern array contains eight of the twelve seamounts and has six of them being in close proximity to each other. The western array contains only four of them and none are in close proximity.

2.1.2 Small and Clustered Seamounds

An interesting portion of the seafloor geomorphology in the westernmost section of the West array of seismometers (~Lat 27.75 N, Lon 149.3 E). There is a small patch of what appears to be very small and clustered seamounds (Fig. 2.2). These seamounds are roughly one tenth of the size of the seamounds used for this study. They do not appear to have a moat around them and would be too small to use in this study regardless of moat presence. This feature is small enough to be observed only with the help of the shiptrack bathymetry.

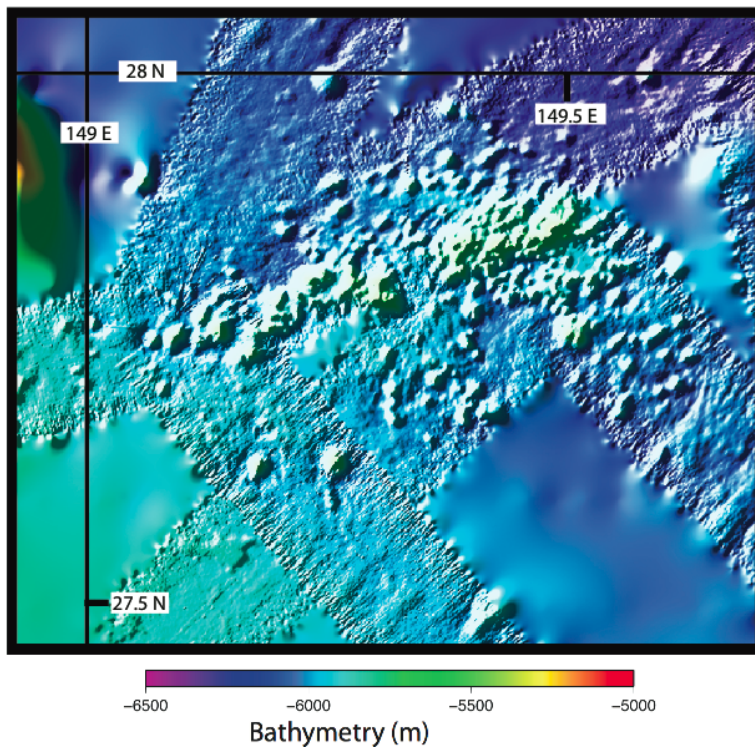


Figure 2.2 The small seamounds shown here do not show a moat around each individual one. This type of cluster is not observed anywhere else in the field area.

2.1.3 Large Seamounds

The most obvious features that are on the seafloor at this location are the large seamounds (Figure, 2.3). These seamounds are located throughout the field area and encompass a relatively large amount of the surface area. They are more abundant in the

western section of the field area, but are not uncommon in the eastern part. These seamounts were purposefully avoided for the location of the seismometers and most of the surveying. The large amount of volcanism that they entail would disrupt the natural growth of the lithosphere and would provide an inadequate location for the PLATE study. Since they are located outside of the main area of interest, they had little effect on the growth of the lithosphere within the two arrays.

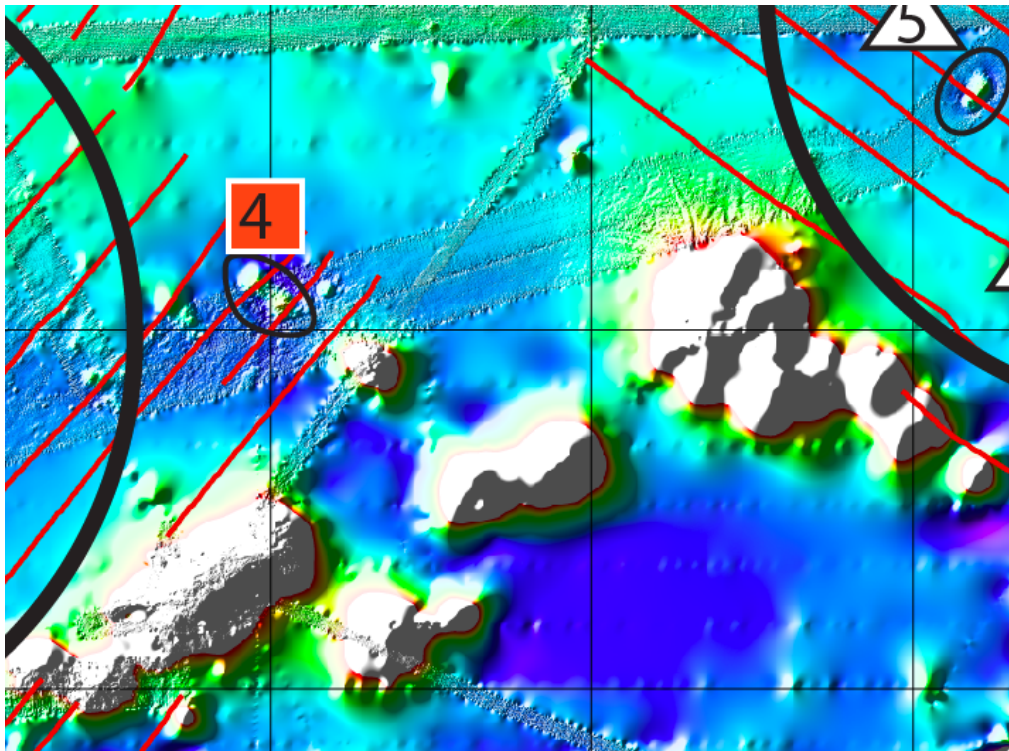


Figure 2.3 Large seamounts found in the study area are located outside the two arrays (black circle segments) where the most interest lies for the study.

2.2 Abyssal Hills

2.2.1 Abyssal Hill Geomorphology

One of the most striking features that can be observed within the field area is the abyssal hills located within the eastern array (Figure 2.4). The abyssal hills on the western array, are oriented roughly NNW along the same orientation as the magnetic

lineations. On the eastern array, much more faint abyssal hills can be observed. I suspect that this is due to higher rates of sedimentation in the eastern array. Uneven sedimentation is also prominent in the seamounts within the eastern array. The moats are clearly observed on the southern portion of the seamounts, whereas the northern parts show a very small and ill-defined moat. The moats are partially covered with sediments on their northern side. Potential sources for this uneven include the cold and bottom water current coming from the Sea of Kohtz (general NS current) and uneven moat formation. The DSD site 52 and DSDP sites 196, 197 and 198 are all located within the general area, but none is located either array. The true cause for the unevenness of the moat is unknown.

There are many models explaining the formation of these abyssal hills (McDonald, et al., 1996; Buck and Poliakov, 1998) involving magmatism, tectonism and the combined influence of both. Abyssal hills, regardless of the method of formation, are created within 2-5 km off the ridge axis. (McDonald et al., 1996). The timing of formation of these features is therefore relatively soon after the formation of the seafloor in which they occur, including slow spreading ridges.

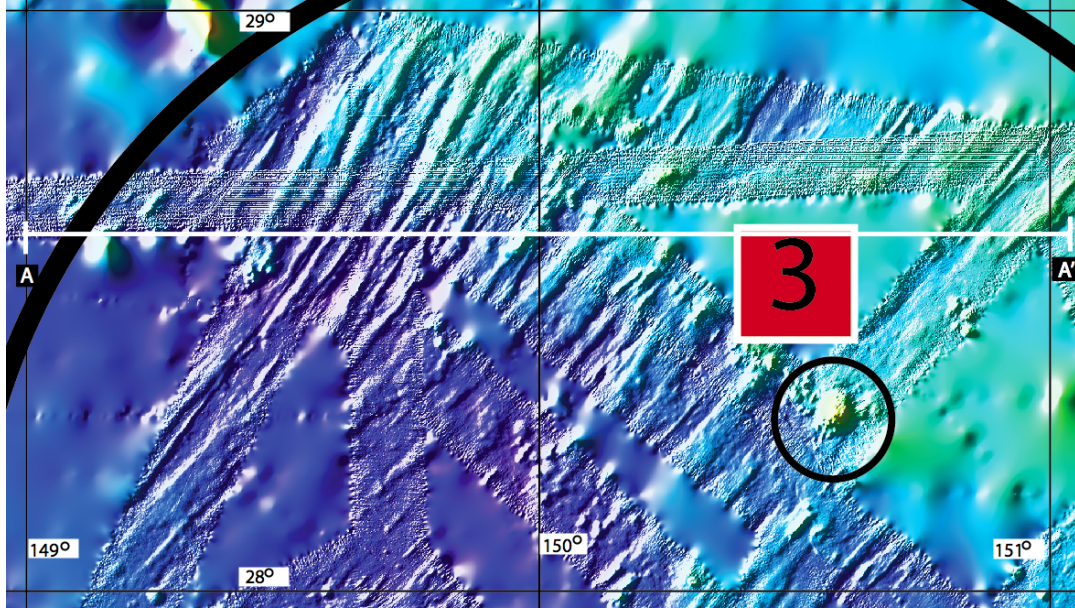


Figure 2.4 The most prominent abyssal hills in the field area are shown. The hills are parallel to the magnetic lineations in this area. A – A' line is shown in figure 2.5.

The high-resolution bathymetry obtained during this study allowed us to clearly observe abyssal hills in the field area. The area covered by the abyssal hills is not too extensive as a percentage of the entire map area (Fig. 1.4). Though this area is not very large, it only represents the portion that was surveyed with the shiptrack bathymetry, and likely encompasses most of the area in which I am concerned with. The level of detail necessary in order to be able to observe the abyssal hills is completely non-existent with the satellite bathymetry as well as with the “surface” routine used in GMT (see Map Making Procedures section). The difference in resolution can be observed in the cross section A-A'. The distance from -100,000 to 0 m was created using the shiptrack bathymetry, whereas the surface routine plots the distance from 0 to ~50,000 m.

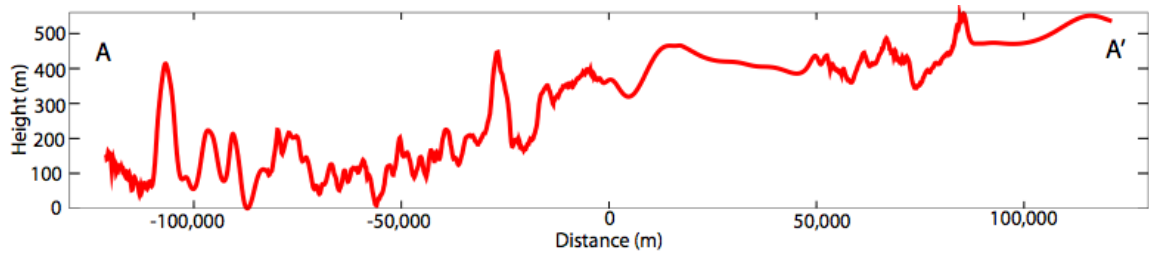


Figure 2.5 Cross-section of the abyssal hills along the Lat 28.612° N line reaching from Lon. 149° E to Lon. 151.05° E. The abyssal hill fabric is more apparent in the western portion of the graph. A – A' line is shown in figure 2.4.

The portion of the field area that has been surveyed using shiptrack bathymetry is in the order of 25% of the total area. This indicates some uncertainty regarding the actual area that is covered with abyssal hills. The locations where no surveying was done are in part located in zones where large seamounts are present. These large seamounts prevent the observation of abyssal hills, as the hills either have been destroyed by the seamounts or were never present.

2.2.2 Hybrid Seamount/Abyssal Hills

Abyssal hills and seamounts are for the most part easy to identify. There is one instance within the field area where it becomes difficult to clearly determine which of these two features it is that is being observed (Fig. 2.4).

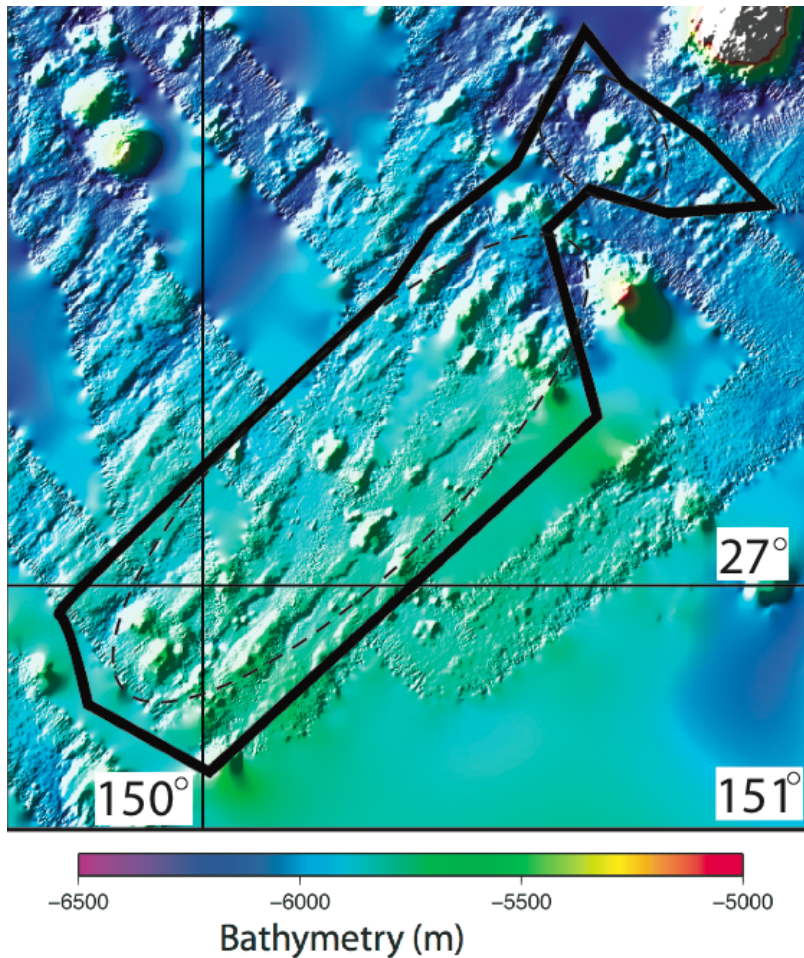


Figure 2.6 The black outline represents the location of the hybrid seamounts. The shapes of the three peaks in the northeastern section show more characteristics of a seamount than an abyssal hill, whereas the features of the southwest resemble abyssal hills.

At Lat 27.4 N, Lon 150.5 E, there are thirteen distinct seamounts or abyssal hill sections that can be observed. Out of these thirteen, three of them appear to be seamounts that are slightly elongate. These three are located at the farthest northeastern portion of the outline in Figure, 2.2. Though these seamounts are slightly elongate, they lack one of the characteristic features that are observed in most of the elongate seamounts. They do not have a visible secondary or minor peak in them. This by itself would not be very suggestive; however, the fact that their elongation is parallel to the abyssal hill direction and they are not segmented perpendicular to the abyssal hill elongation direction, suggests some linkage between the two. One possibility is that the abyssal hills possess

fractures or normal faults that are sites of reactivation when magma or stress is introduced.

The remaining ten peaks (Lat 20.2 N, Lon 150.2 E in Fig. 2.5) that are observed resemble abyssal hills more than they do seamounts. They are very elongate and aligned with the general direction of the other abyssal hills. The features that distinguish them from the other abyssal hills are their relative segmentation. Other abyssal hills in the area are more continuous along their long axis. Another feature that sets them apart from most abyssal hills is the maximum height that they reach. These hybrid hills are slightly taller than the ones that are observed in other locations and they also have more defined peaks.

Though a much more in detail study would be required, this feature might be a transition between seamounts and abyssal hills. The seamounts appear to be being replaced by a more abyssal hill fabric. This type of growth would be consistent with some of the models proposed as the method for abyssal hill genesis, as is the case of the whole and/or split volcanoes in McDonald et al., 1996 (Fig. 2.5). The larger seamounts found in the northeastern section of the figure can represent the whole volcanoes, whereas the split volcanoes are observed in the southwestern parts of Figure 2.5.

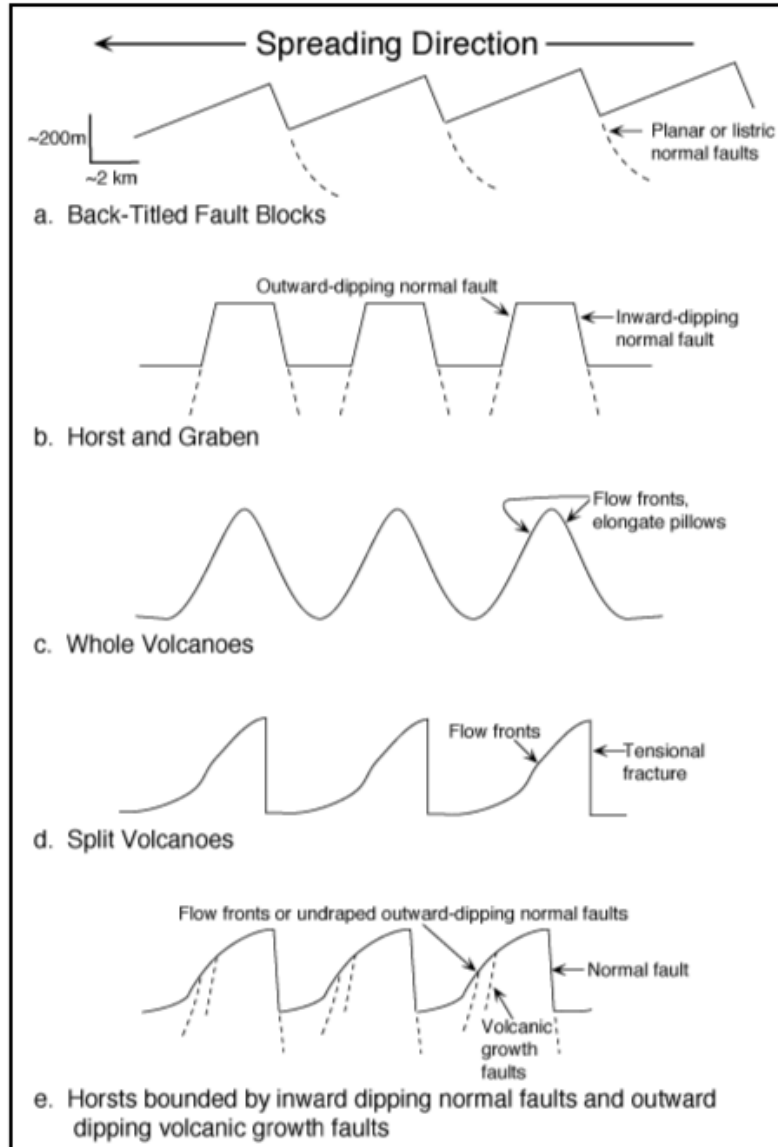


Figure 2.7 The figure shows five different ways in which abyssal hills can be created. Ultimately, the most prevalent way in which they form is the split volcano, where a tensional fracture creates one side, and volcanic draping occurs in the other one. Figure obtained from McDonald, 1996.

Chapter 3.0

METHODOLOGY

3.1 Map Generation

In order to make the field area map (Fig. 1.4), three different sources of data were used. As discussed earlier, the first dataset acquired was the shipboard bathymetry. Though this data set is very high quality, it is by no means a complete survey of the field area and was supplemented with previous datasets. The National Geophysical Data Center (NGDC) provided two datasets from previous ship tracks through the area that complemented the bathymetry. I do not use publicly available Smith and Sandwell, 1997 global data to avoid using gravity dependent bathymetry.

The first dataset consisted of shipboard multi-beam measurements. It seems that only few swaths of data were collected during these cruises while in transit to another destination. Despite the high resolution of the data, it was not thoroughly processed and contained data points that had to be manually edited out as they yielded erratic and unreasonably deep bathymetry (some points yielded up to 9 km depth).

The second dataset (Fig 3.1) used was also obtained through the NGDC website. This dataset consisted of single-beam bathymetry collected by older instrument systems. The data collected dates back to the 1950's prior to the use of GPS for positioning of the collecting vessel. Therefore, the single beam data sets were split into two parts: data collected before and after 1985. The year 1985 was chosen due to the fact that GPS technology was no longer restricted to military use was finally very widespread in research vessels.

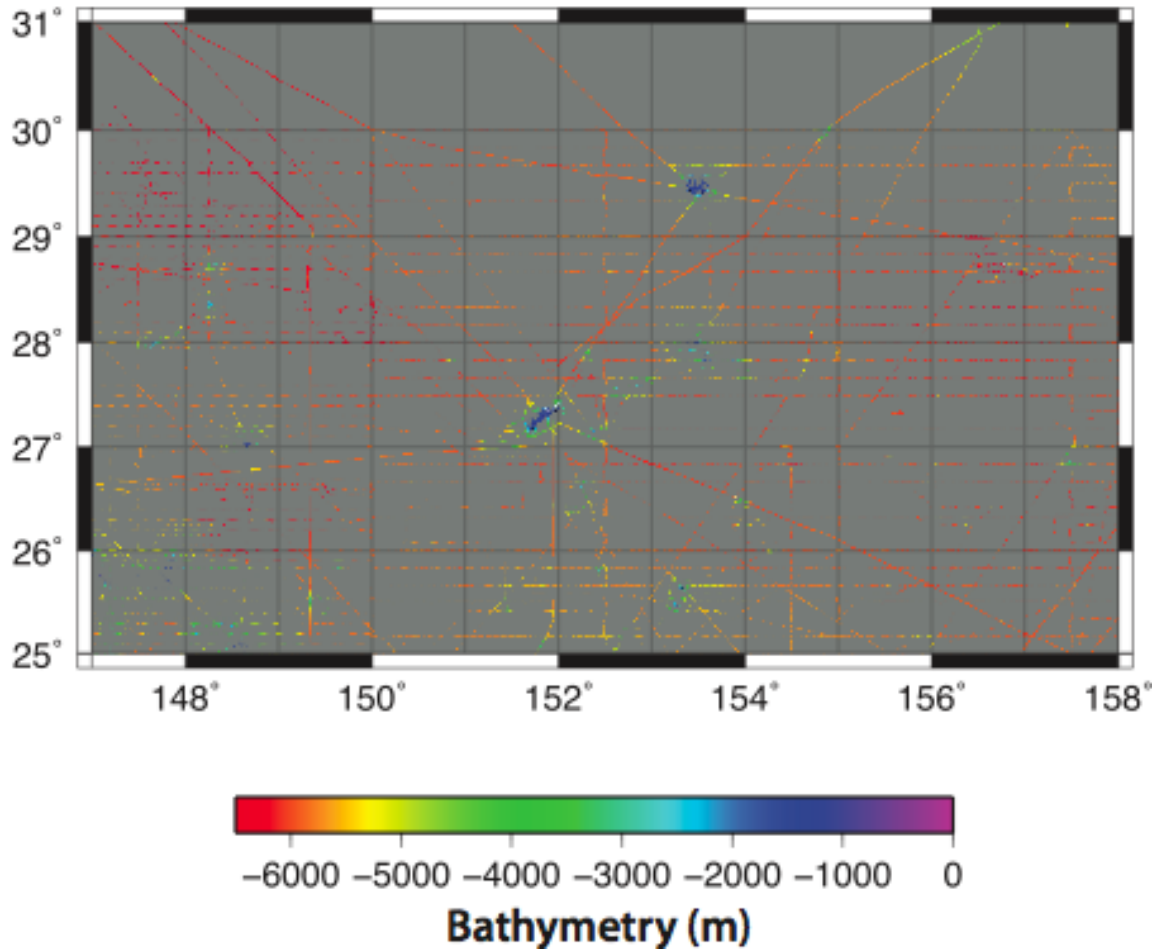


Figure 3.1 Map of the publicly available single beam bathymetry collected after 1985. The data was collected at roughly 10' of latitude and 2' of longitude. Also, transects at diverse angles were collected en route to other projects. Data obtained from NGDC.

This secondary dataset (Fig. 3.1) is much more ubiquitous in terms of area covered by the survey. It spans the entire field area. The wide coverage, however, comes at a price of resolution. As mentioned before, this is a single-beam dataset. The measurements are taken at very evenly at 10' increments of latitude up to the 30° N line. In every transect parallel to the equator, one data point was collected at about every 2'. Single beam survey of most of the larger seamounts in the area added a great deal of data. Data are much more clustered on the seamounts. It is also observed that it was collected at random orientations and has focus on “interesting” parts of the seamount such as the

summit and their edges. There are also several transects in random directions throughout the area that most likely are the product of vessels that did not have this location as a main destination, but collected data as they passed through.

After obtaining these three different datasets, they were combined together. This was a challenging task as all three datasets were in different format and plotted at different resolutions. The combining process took three steps. The program Generic Mapping Tools (GMT) was the program used to plot the data in map format.

First, each individual dataset was plotted separately. Both the shipboard multi-beam bathymetry from the PLATE project and the data obtained from NGDC were made into a grid of 100 by 100 m. Every value of bathymetry that the multi-beam collected was assigned to an area of 100 m². These same criteria were applied to the single beam data; however, it was unsuccessful as the data were not visible due to the small number of points in the dataset. The grid spacing for this dataset was increased incrementally reaching a 3 km by 3 km grid (Figure 3.1). This proved to be satisfactory and improved the quality of the data. This step was required in order to obtain all three different data sets in the same format in order to be combined, and to estimate the quality of the data.

The second step consisted of combining all three datasets into one. The grid spacing chosen for this step was 100 m by 100 m. Though the single beam data are visible only in areas of high density, all the data points were still incorporated into the final grid. After this step, the grid file was converted into an xyz file in order for it to be re-processed.

The final step in combining the data consisted of reprocessing all the data and plotting a surface map. In order to reprocess the data, the newly created xyz file was run

through pre-made routine in GMT called “blockmean”. This routine averages out every single data point with respect to its closest neighboring point, therefore creating a smoother representation. This process also determines the amount of data points required in order to process the plotting surface at a much faster pace. This step reduced the plotting time by about 1500 times. Finally, after this preprocessing, the final map was created by interpolating using a “minimum curvature” algorithm in between gaps of data. The “surface” routine built into GMT produced the final map that was used to observe all of the geomorphologic features in the field area (Fig. 1.4).

3.2 Seamount Selection

I used very general geomorphology criteria to choose the seamounts that were used for this study. Only twelve seamounts were chosen for this study. Most of these are very similar to one another despite the fact that they were chosen by using only one parameter. The only criterion that was used in order to select the seamounts was the fact that they had a moat around them or partially around them. The seamounts were selected in two different locations. Since the high resolution bathymetric coverage of the area was concentrated where the seismic instruments were deployed, it was no surprise that the seamounts were also found in two relative clusters. The western array includes seamounts #1 - 4, and the eastern array contains the remainder (#9-12).

3.3 Data and Model Parameters

The Young’s modulus and the Poisson’s ratio for basalt were used for both seamounts and the lithosphere. The lack of segmentation of the lithosphere into its crust

and upper mantle (both of the layers were assumed to be one uniform layers) components was used to avoid a multilayer model in the program that would be exponentially more complicated to compute. The parameters that are obtained from the seamounts and their surroundings are depicted in Figure, 3.2, and shown in Table 1. The height of the seamount (h_o) is defined as the difference between maximum bathymetric height and the average baseline. The moat radius (xb) is measured from the center of the seamount to the top of the bulge on the outer margins of the moat. The deflection depth (w_o) is defined by the maximum amount of bending of the lithosphere under the load of the seamount. The wavelength of a periodic load (λ) is obtained by multiplying the diameter of the seamount by two. Lithospheric thickness is interchangeably used with elastic thickness (Te) in this study. Table 1 shows all of the constants and parameters that were calculated and measured from the bathymetry and used for data input into the programs.

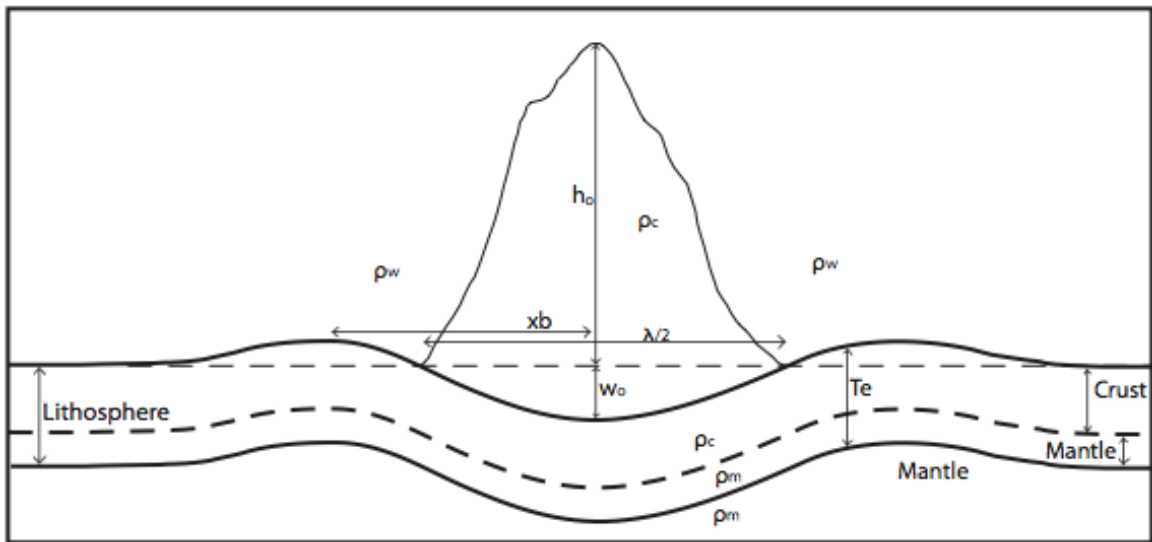


Figure 3.2 Schematic cross-section of the seamounts showing the parameters obtained from the map.

3.4 Parameters Obtained

The high resolution bathymetry data allowed for very detailed observation of relatively small scale features of the seafloor. The moat radius (xb) is the most important

parameter that was used for the elastic thickness calculations. This parameter was used to obtain a depth of deflection of the seafloor caused by the applied force of the seamount's mass. The moats are not uniformly shaped and are extrapolated by visual means at several points around the seamounts. Seamounts two and twelve (Fig. 3.3) exemplify the two extremes of difficulty for delineating the moat radius on the seamounts. Seamount number 3 (Fig. 3.3a) shows a moat that is interrupted by several other features on the seafloor. The moat is very obscured, however careful study of the morphology allowed for a measurement of the radius. In the figure 3.3b, it is easy to observe a semi-circular depression around the seamount just south of it. While the depression is not continuous all around the seamount itself, the portion of it that extends the farthest from the seamount center just south-southeast was used as the measurement.

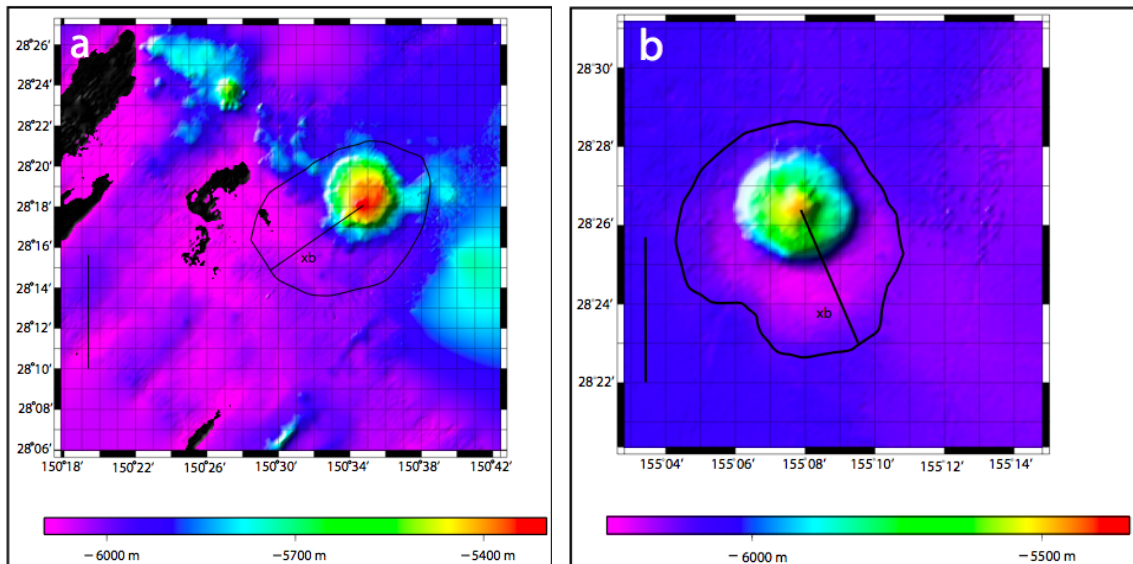


Figure 3.3 a) Seamount 3 where abyssal hills disrupt the seamount moat making it difficult to see where exactly it lies. Figure 3.3 b shows a seamount on relatively smooth seafloor showing a moat that is partially covered, but easy to identify.

Symbol	Value	Units	Name
ρ_c	2950	kg/m ³	Crustal density
ρ_m	3250	kg/m ³	Mantle density
ρ_w	1030	kg/m ³	Water density
ρ_i	2950	kg/m ³	Infill density
E	7×10^{10}	Pa	Young's modulus
ν	0.225	*	Poisson's ratio
g	9.81	m/s ²	Gravity
h _o	*	m	Seamount height
w _o	*	m	Deflection Depth
T _e	*	m	Elastic Thickness
x _b	*	m	Moat Radius
m _x _b	*	m	Measured moat radius
V	*	m ³	Volume
P	*	N	Load
B	*	m	3 dimensional flexural parameter
D	*	N m	Flexural rigidity

Table 1. The parameters used in the calculations with their units and representative symbol.

Although for the most part it was easy to observe the moats around the seamounts, it was equally easy to observe that none of the seamounts had a perfectly symmetrical and complete moat around it. The irregular geometry of the seamounts is attributed to the locally higher rate of sedimentation in the area. The obscured moats on the northern side of the seamounts suggest preferential sedimentation. Seamounts on the western array appear to have a lower rate of deposition.

3.5 Calculations

3.5.1 Volume Calculation

The first program I use calculates the total volume for each individual seamount. The input for the calculations made in this program is a single xyz file with latitude, longitude and bathymetry. The input file was gridded and point extrapolated to produce

even 100 m spacing between grid points (Fig. 3.4a). To obtain the appropriate volume of the seamount from its average base point, the bathymetry data values that were below the average base depth were omitted and a new xyz file was created (Fig. 3.5b). This new xyz file contains the data for the calculation of the seamount volume.

In order to calculate the total volume of the seamount, the program sums multiple square prisms (Figure 3.4), where each prism has a square base at 100 m by 100 m and a height that depends on the bathymetry value at that point. As bathymetry is defined as depth below sea level, the values are negative numbers. First, the values are changed to positive in order to determine the total magnitude. The lowest bathymetry value in the file was subtracted from all other points, therefore obtaining a relative height of the seamount (rather than a bathymetry value). Once all of the values for the seamount “height” are obtained, they are multiplied by the area of the base. This yields a volume for each individual prism. Finally, all of the volumes of the prisms are summed together to give the total volume of the entire seamount.

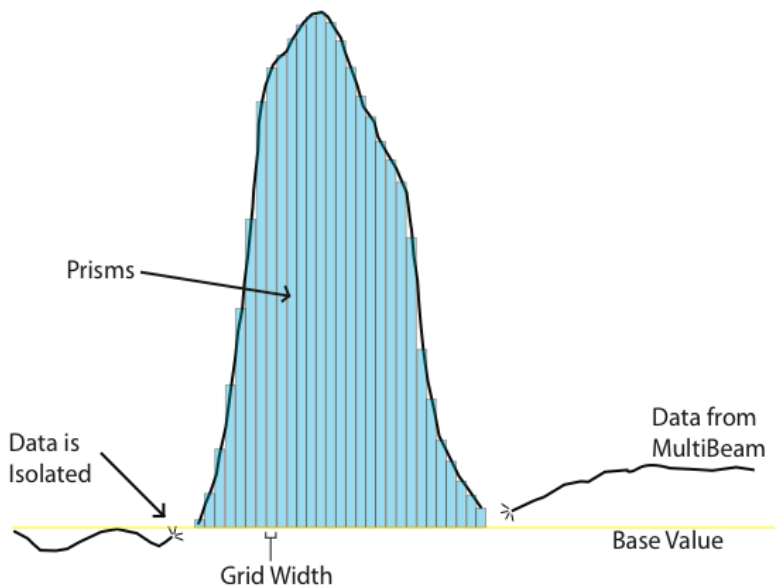


Figure 3.4 Two dimensional view of the volume calculation. The blue rectangles represent the square prisms that are used to calculate the volume of the seamounts.

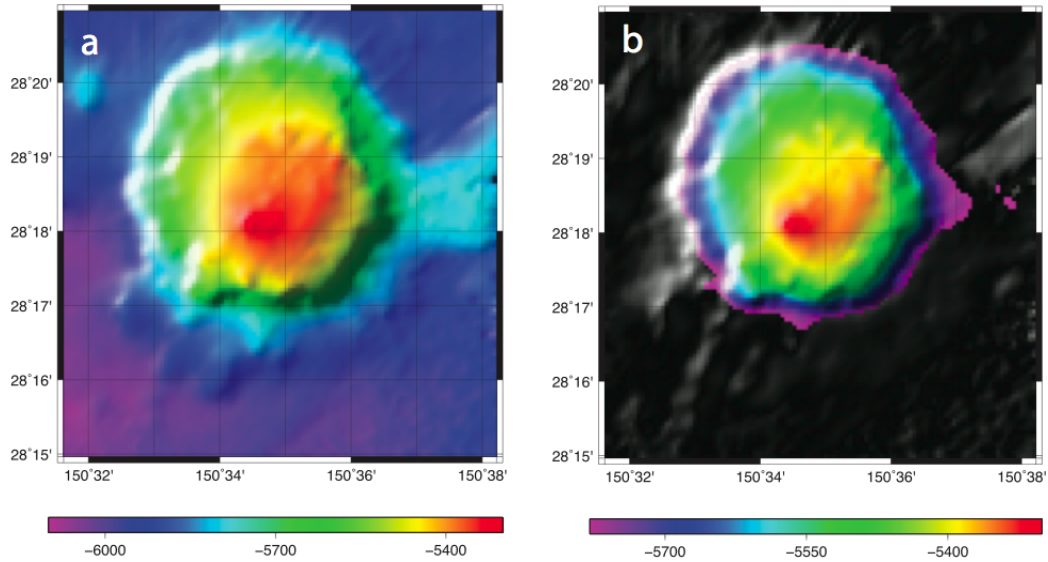


Figure 3.5 a) Zoomed in area which was chosen for the volume calculation in seamount #2 is shown. The small area was chosen to avoid nearby structures that have similar bathymetries. b) The values that were separated from the map are plotted in

3.5.2 Deflection Method

To determine plate flexure from the seamount load, two physical parameters must be determined, 1) the deflection and 2) the total seamount volume. Although I calculate the seamount volume above which includes the mass above an average base line, this does not include any of the volume that fills the deflected portion of the lithosphere. Thus once the amount of deflection of the plate is determined, I must calculate the volume of material infilling this deflection as well the seamount, which together make up the total volume of the seamount. Both the “deflection method” and the topography method” (described here and below) are modeled as an infinitely long beam overriding an inviscid fluid. This model is assumed true for most of the oceanic lithosphere due to its uncomplicated thermal history (Wessel, 1996). The Deflection Method was applied to each of the seamounts to calculate the total deflection or bending that the lithosphere underwent as a result of the seamount’s mass.

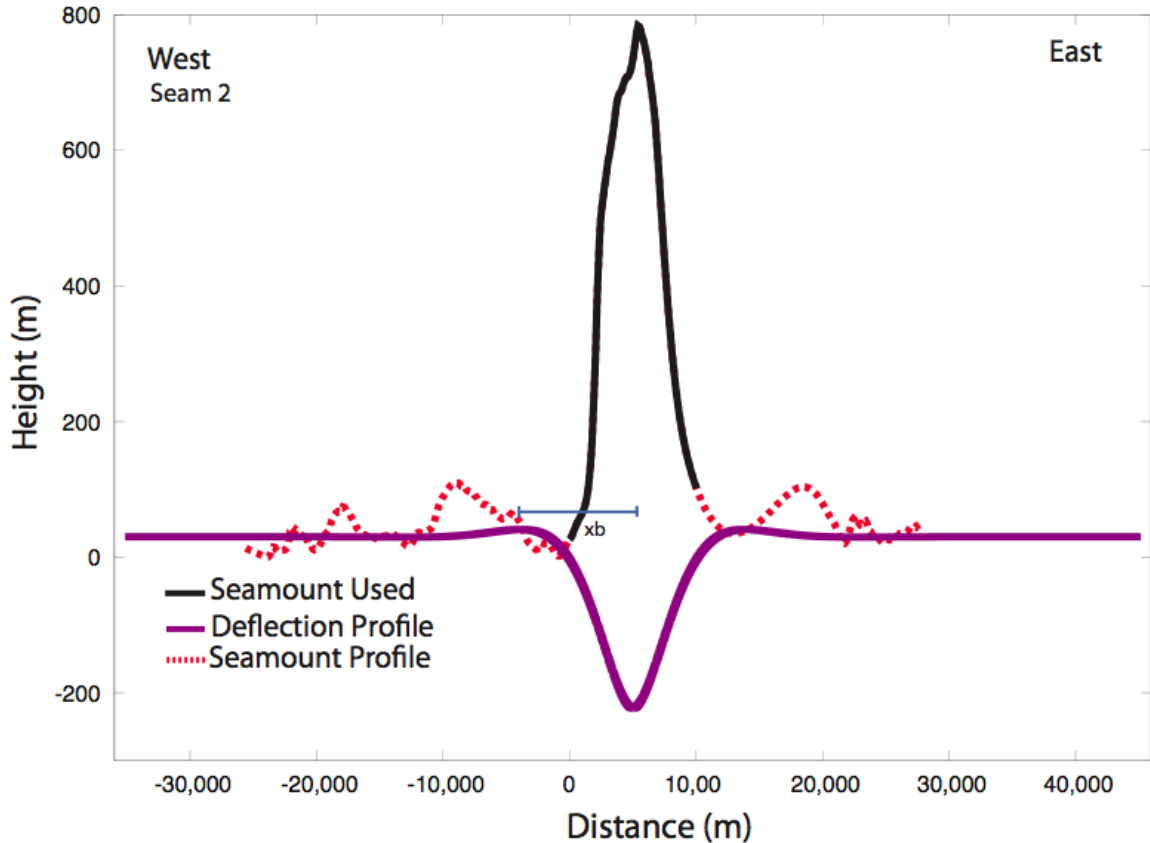


Figure 3.6 Seamount #2. The deflection profile caused by the load of the seamount is shown in the purple solid line. The calculations are based on the solid black line, which represent the seamount obtained from the profile. The dotted red line represents the seamount profile including its surroundings.

The first input for the program is an xyz file that contains the latitude, longitude and bathymetry of the specific seamount. The program uses the input file to extract all the data points that are along a user specified latitude or longitude. The profile chosen for the program is always along the peak of the seamount. These points are paired with their respective bathymetry values. The combined values produce a profile. In order to produce a more useful and visually informative profile, their respective base value for the seamounts, which was used to obtain seamount volumes, is added to the all of the bathymetry values of each seamount. Then, the latitude and/or longitude grid values are converted to meters giving a lateral distance that is centered at the southernmost portion of the seamount.

The dotted red line shown in figure 3.5 is the profile of the seamount (# 2). The solid black line represents the points that isolate the seamount and exclude the moat and surrounding region. This second profile contains the actual values that are used to calculate the maximum deflection and deflection profile for the seamount. There are a number of constants and variables obtained from the maps, which can be seen in Table 1.

The basis for calculating the deflection depth in this program is an equation (Watts, 2001 p. 67)

$$w_o = \frac{P}{8\beta^2 (\rho_m - \rho_i) g} \quad (\text{eq. 3.1})$$

where w_o is the deflection depth, P is the total load that the seamount exerts on the seafloor, ρ_m is the density of the mantle; ρ_i is the density of the material that occupies the displaced lithosphere and β is the three dimensional flexural parameter. The three dimensional flexural parameter (Watts, 2001) is defined by

$$\beta = \left[\frac{D}{(\rho_m - \rho_i) g} \right]^{1/4} \quad (\text{eq. 3.2})$$

The three dimensional flexural parameter is related to the moat radius (xb) as

$$\beta = \frac{xb}{2.905} \quad (\text{eq. 3.3})$$

where xb in this equation represents the moat radius measured from the seamount map (see table 1). The D in the equation represents the flexural rigidity of the lithosphere (see eq. 3.8 for a complete definition of the parameter).

The deflection calculation utilizes equation 3.3 to obtain a three dimensional flexural parameter. In order to obtain the deflection depth, an initial deflection depth is set *a priori* at 35% of the maximum height of the seamount. The total volume of the seamount is recalculated to include the added material within the deflection. Equation 3.4 calculates the total load of the new seamount volume using the user input of the previous

volume calculation, the density of the crust, and gravity using the relationship

$$P = V \rho_c g \quad (\text{eq. 3.4})$$

The moat radius (xb) and deflection depth (w_o) are the model parameters I solve for in this calculation. A calculated moat radius is obtained from the calculation at the end of the program. This calculated moat radius is compared to the measured moat radius (from our maps) and the difference between the two is obtained. If the difference exceeds 1% the size of the measured moat, the program iterates the process and calculates everything once more using an updated deflection depth and an updated seamount volume until the 1% difference requirement is satisfied. To calculate this difference I used:

$$err = \left(\left(\frac{xb}{mxb} \right) / mxb \right) 100 \quad (\text{eq. 3.5})$$

where mbx is the measured moat radius and err is the percent error. I then obtain the final deflection depth (w_o), which provides the best fit between the observed and predicted moat radius. Once the deflection depth is calculated, a profile for the deflection underneath the seamount is plotted (yellow line in fig. 3.5) using a theoretical curve from Turcotte and Schubert, 2002:

$$w = w_o e^{-x/4} \left(\cos \frac{x}{\alpha} + \sin \frac{x}{\alpha} \right), \quad (\text{eq. 3.6})$$

where x represents horizontal distance points and α is the flexural parameter defined by the following equation:

$$\alpha = \frac{xb}{\pi} \quad (\text{eq. 3.7})$$

Thus this calculation provides the estimated deflection profile obtained from the final deflection depth, which considered the seamount height with updated seamount volume

as constrained by the best fit between the measured and calculated moat radius.

3.5.3 Topography Method

The topography method utilizes the deflection depth obtained in the first program to solve for the elastic thickness of the lithosphere at the time of loading. The initial processes of the program are to obtain an xyz file that contains the data of the seamount. The selected profile line (which should coincide with the seamount peak) is user defined. The program then obtains all of the data points that are located within that defined latitude or longitude depending on which profile is chosen. Once this is obtained, the seamount section without the moat or its surroundings is separated (solid black line in figure 3.5) for all of the future calculations. The measured moat radius, seamount height and the calculated volume are input into this program at this time. The constants that are pertinent for this final step of the calculations include gravity, Poisson's ratio, Young's modulus (for basalt) and, the density of both the mantle and crust (Table 1) are also included in this step.

This program utilizes an *a priori* elastic thickness (of 5000 m) as a starting model. In the first iteration, the total mass of the seamount, obtained from the deflection method is used as an input data parameter. The flexural rigidity is calculated from the relation below using the constants given above

$$D \equiv \frac{E T e^3}{12 (1 - \nu^2)} \quad (\text{eq. 3.8})$$

Where $T e$ is the elastic thickness, E is the Young's modulus and ν is Poisson's ratio (see Table 1). The flexural rigidity is in turn utilized in conjunction with the deflection depth, (both data parameters) to calculate a model of a theoretical seamount height using

$$h_o = w_o \left(\frac{\rho_m}{\rho_c} - 1 + \frac{D}{\rho_c g} \left(\frac{2\pi}{\lambda} \right)^4 \right) \quad (\text{eq. 3.9})$$

where h_o represents the maximum height of the seamount and λ is the characteristic wavelength of the load and deflection (Fig. 3.2). Once the predicted seamount height is obtained, a cross-section incorporating h_o is modeled by applying the following equation from Turcotte and Schubert, 2002:

$$h = h_o \sin 2\pi \frac{x}{\lambda} \quad (\text{eq. 3.10})$$

I then compare the predicted seamount to the real seamount as shown in figure 3.6. The best fit is determined by comparing the area below each 1D profile. The area is obtained by multiplying the height of each data point in the profile by the distance between points. The percent error between the measured and predicted area profiles is achieved by a process similar to what is discussed above but using the following formula

$$\left(\left(\frac{\sum_{i=1}^n (L/n) h_i}{\sum_{i=1}^m (L2/m) h_i} \right) / \sum_{i=1}^m (L2/m) h_i \right) 100 \quad (\text{eq. 3.11})$$

where L is the total length of the profile of the theoretical seamount, L2 is the length of the measured seamount, n is the number of data points in the theoretical seamount, m is the number of data points in the measured seamount. The acceptable error between the two areas is 1%. If this error is exceeded, the program initiates the process again and iterates using an updated elastic thickness until the fit between the observed and predicted bathymetry profile is smaller than 1%. Once this is obtained, the profiles of the theoretical and measured seamounts are plotted (figure 3.6). And finally, the final updated variables used are listed in the output file.

3.5.4 Error Analysis

The errors obtained in the volume calculations are derived from the measurements of the bathymetry data. The errors in the measurements come from creating the grid of the data into a 100 by 100 m, where the accuracy of each side 50 m. The bathymetry data

is extremely accurate and contains errors of 15 m only. The errors found in the volumes calculated range from 0.09 km³ to 0.30 km³ (Figure, 4.7, 4.8, and 4.9). The largest source of error in all of the data comes from the measuring of the moat radius (mx_b). The potential overestimation of the measured radii ranges from 680 m to 4110 m, and the underestimation for the radii is from 1570 m to 4900 m. The range of measurements creates a widespread range in the calculations of the elastic thickness. The errors in the elastic thickness range from 600 m to 1670 km.

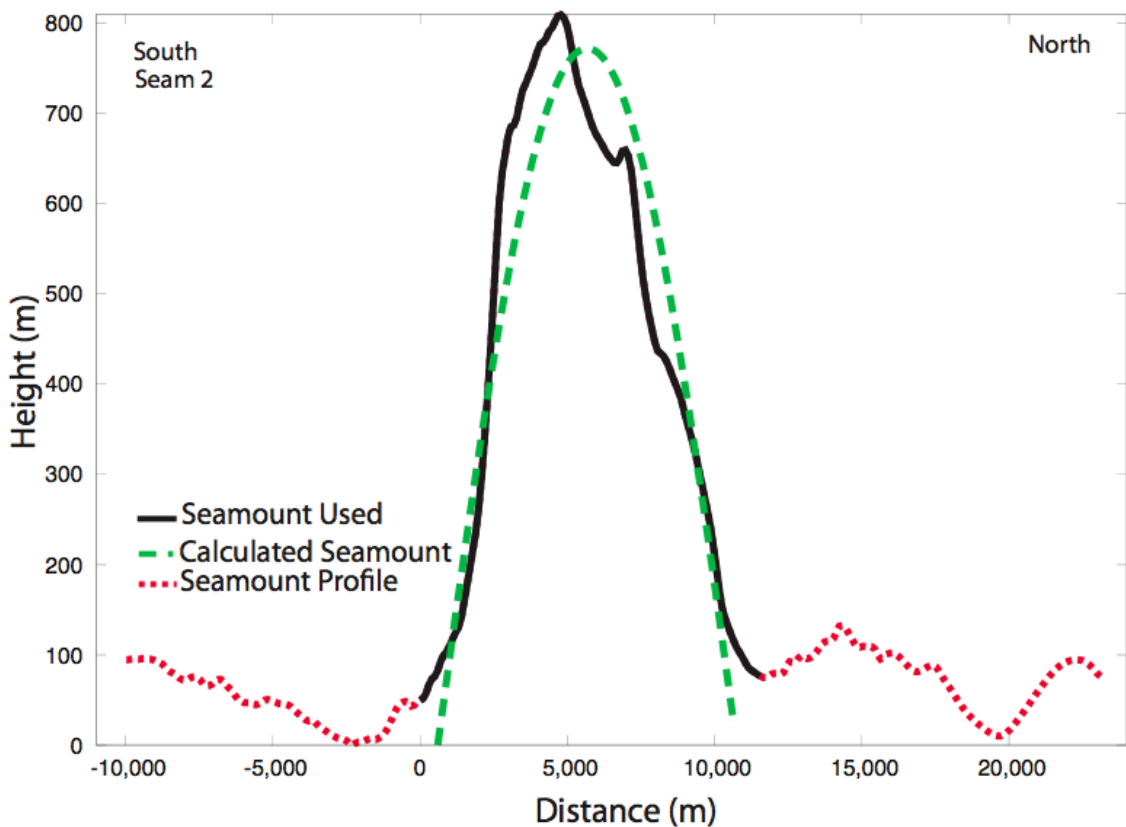


Figure 3.7 Profile of seamount #2. The areas under the curve defined by the green dashed line and the one defined by the solid black line (predicted and real seamount profile, respectively) differ by less than 1%. The dotted red line indicates the profile of the seamount and its immediate surroundings.

Chapter 4.0 RESULTS

4.1 Seamount Maps and Volumes

The seamount (# 7) shown in Figure 4.1 is an example of a conical seamount. More than $\frac{3}{4}$ of the map shown contains high resolution bathymetry from shiptrack. The northwest corner of the map shows smoothing produced by the interpolation of more sparse or single beam shiptrack points. The seamount is very circular with only one peak at its center. This is the largest seamount that I use in this study standing at roughly 4700 m below sea level. The seamount height is about 1377 m above the average background bathymetry. The circle at its base has a radius of 4.3 km (***xb*** shown by red line) . The heavy black outline circling the seamount in figure 4.1a delineates the observable moat radius. Notice that the radius is largest in the southwest section of the map. Thus I model a moat that extends equally in all directions (dashed circle) of the seamount based on the radius observed south of the seamount. This is predominantly observed in the seamounts that are within the eastern array. I calculate the volume of the seamount using the grid file in figure 4.1c. The colored points in figure 4.1c represent the values used from 4.1b to obtain the volume. The volume obtained for this seamount is $2.82 \times 10^{10} \text{ m}^3$. This volume does not include the added volume in below the base of the seamount due to flexure underneath the seamount.

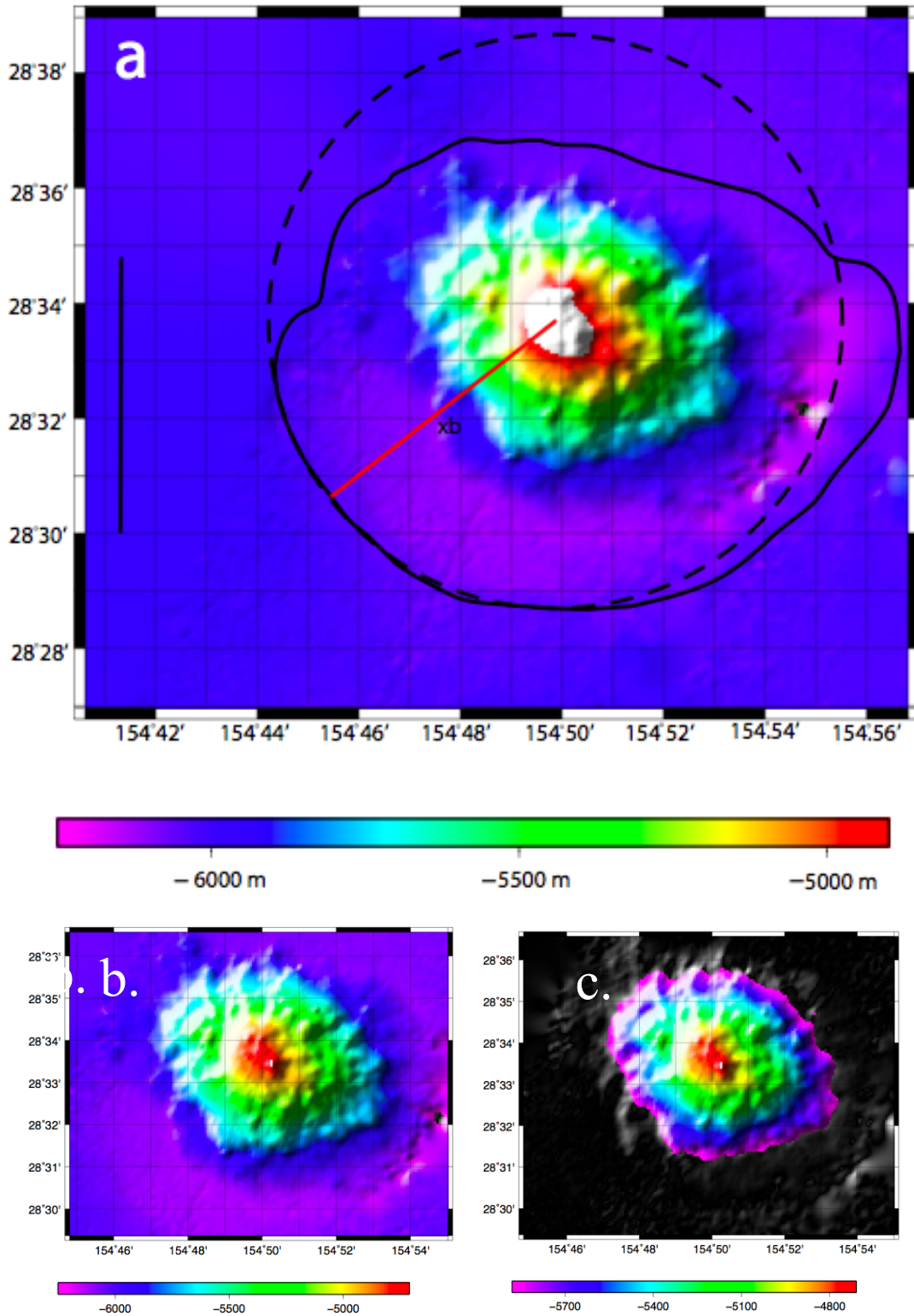


Figure 4.1. a) Seamount #7 is the largest seamount found in the area. The black outline defines the observable parts of the moat. The line "xb" indicates the moat radius measured for this seamount. Dashed line represents the inferred moat around the seamount. b) The map portion that was used for volume calculation. c) In color are the values extracted from the map that were used for the volume calculation.

The seamount #1 in Figure, 4.2 is located on the western most portion of the field area. This seamount is one example of an elliptical seamount with a visible “main peak” and secondary plateau trailing it. The edges of rough bathymetry that are observed north and south of the seamount that trends ENE are the edges of the shiptrack Multibeam swath. The edges create an artificially rough bathymetry due to the roll of the ship. The regions north and south of the shiptrack are smooth where the data are interpolated between more sparse or single beam shiptrack points. The black solid area in the lower right corresponds to bathymetry values that are deeper than the scale bar and is an artifact of the interpolation of the lower resolution bathymetry data. The maximum height of the main peak is 5100 m below sea level and the plateau elevation is approximately 5350 m. The seamount height is about 1029 m above the average background bathymetry. The major axis of the seamount is about 9.3 km in length and the minor axis is 5.5 km wide. I select the moat around it shown by the heavy dark outline (Fig. 4.2a). The area surrounding the seamount is very flat and possibly sediment filled.. I calculate the volume of the seamount using the grid file in figure 4.2c. The colored points in figure 4.2c represent the values used from 4.2b to obtain the volume. The volume obtained for this seamount is $1.99 \times 10^{10} \text{ m}^3$. This volume does not include the volcanic material found where the flexure of the lithosphere occurred.

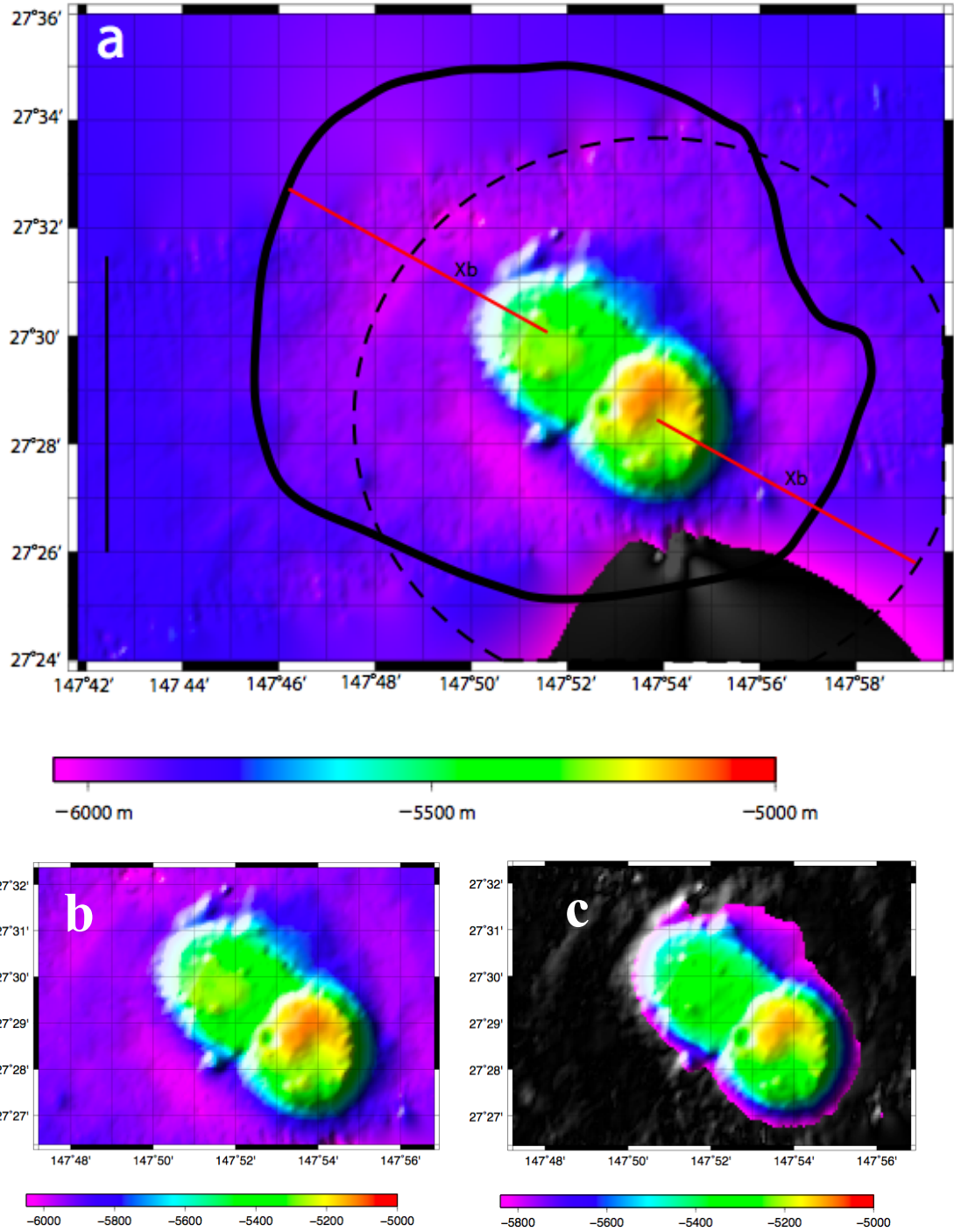


Figure 4.2 Seamount #1. a.) Seamount shown with surrounding bathymetry. The thicker dark line outlines the flexural moat. Dashed line indicates inferred moat. The moat radius selected is indicated by xb. b.) Close up view of seamount 1. This grid file was used to obtain the volume of the seamount. c.) Grid values that were used for the volume calculation are shown in color

4.2 Plate Deflection Depth

The two dimensional bathymetry of seamount #7 and #1 is shown in figure 4.3 and 4.4 respectively by the red dashed line. These data points are obtained from the grid points in figure 4.1a and 4.2a extending from south to north. The solid black line represents the data points that encompass the width of the seamount that was used to obtain the deflection profile. A calculated moat radius (xb) was compared to the observed radius (mx , shown by red line in Figure 4.1a) in order to solve for a maximum deflection depth (wo) consistent with equation 3.1. Note that the larger seamount #7 (Fig. 4.3) produces a larger deflection depth of 657 m compared to seamount #1 (Fig. 4.4) which has a value of 363 m. The observed moat radius is 10,100 m for seamount #1 and 9,145 m for seamount #7. The deflection value (wo) is used to update the total volume of the seamount to include the material that is within the infill yielding volumes of $2.3 \times 10^{10} \text{ m}^3$ for seamount #1 and $3.5 \times 10^{10} \text{ m}^3$ for seamount #7.

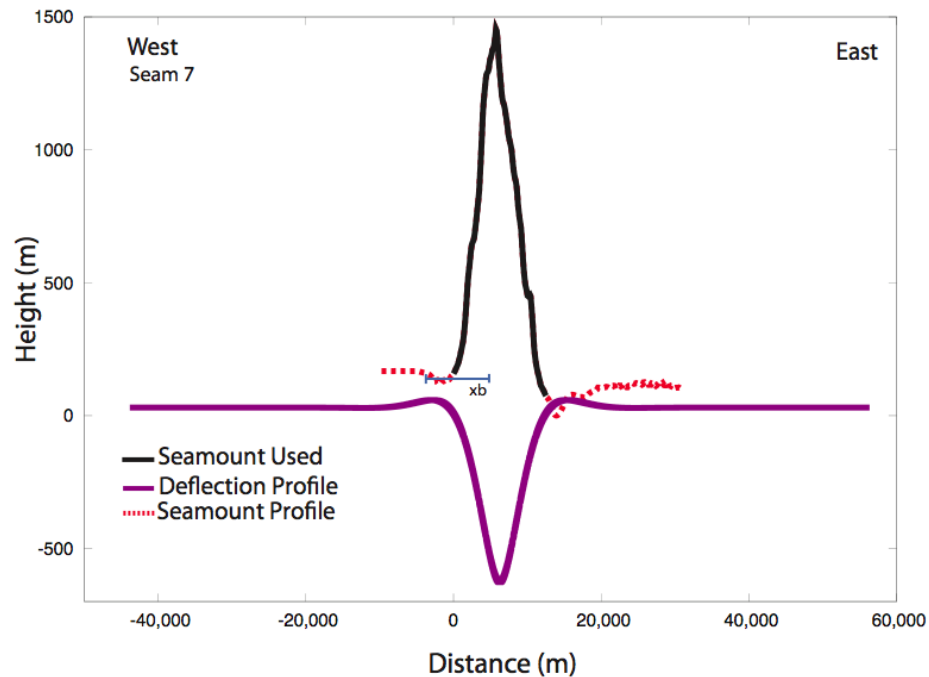


Figure 4.3 a) Seamount #7 profile of the seamount and its surroundings, the black line shows the portion of the seamount that was used for all the calculations.

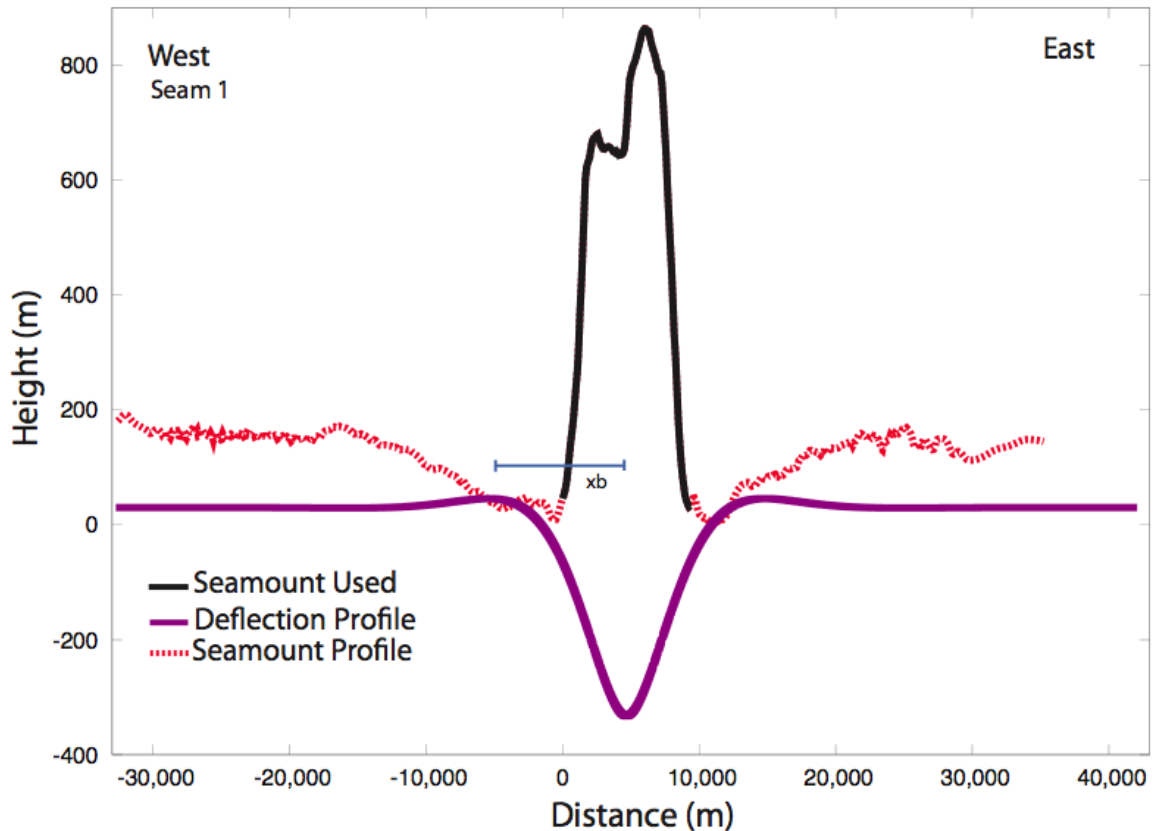


Figure 4.4 Seamount #1 profile of the seamount and its surroundings, the solid black line shows the portion of the seamount that was used for all the calculations.

4.3 Elastic Thickness Calculation

In this calculation, I fix the volume as the total volume of the seamount that includes the deflected volume obtained from the deflection method in the previous step. The red dotted line in figures 4.5 and 4.6 represents the bathymetry profile for seamount #7 and #1 along an east-west transect through their peaks obtained from figures 4.1a and 4.2a. The solid black line represents the seamount profile used to compare with the predicted seamount profile (shown as a green dashed line). The best fit of the areas under both, the real seamount (solid black line) and the calculated theoretical seamount (green dashed line) gives us the basis to determine the resulting elastic thickness using the

relation given by equations 3.8, 3.9, and 3.10. I perform this calculation on profiles that are east-west as well as north-south. The final elastic thickness value was obtained from the average of the two. The elastic thickness obtained for seamount # 7 is 3403 m and the elastic thickness for seamount # 1 is 3330 m. These elastic thickness values are quite similar for seamounts with two very different sizes; an observation that will be explained below.

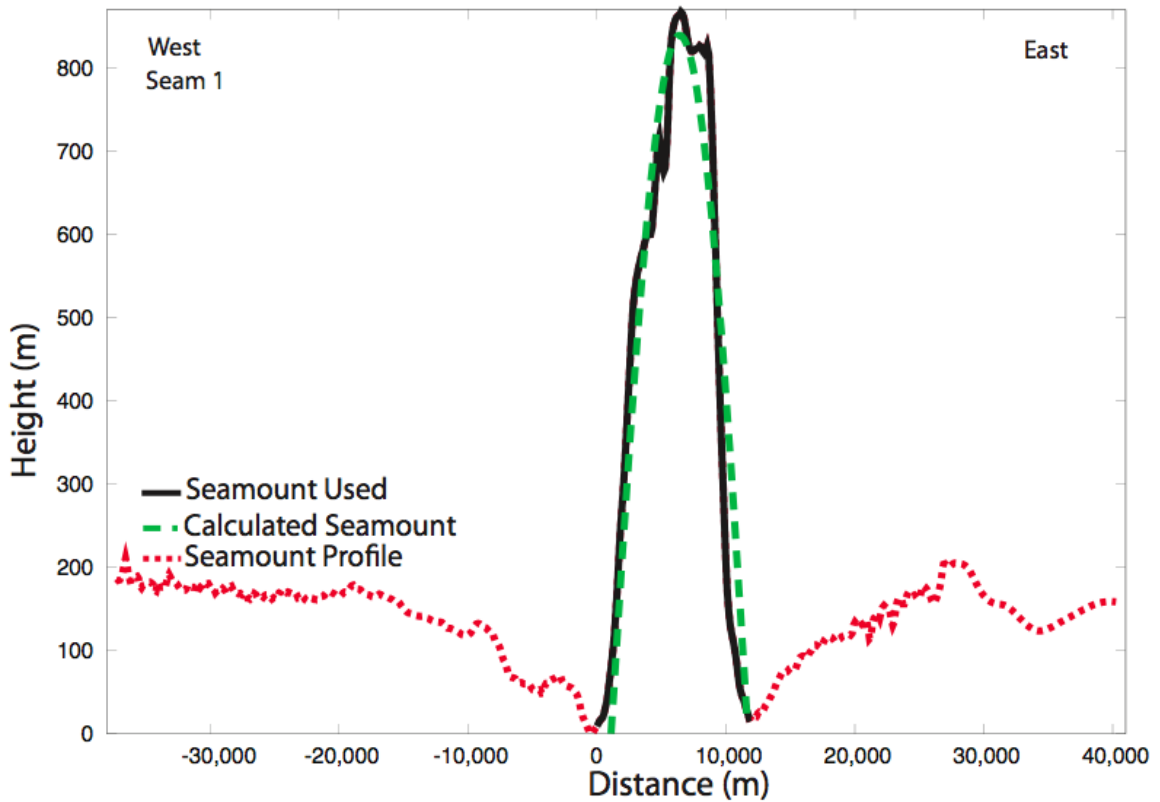


Figure 4.5. The profile of the seamount #1 is show in the red dotted outline along the 27.48 latitude profile. Theoretical seamount calculated is shown with the green dashed line, whereas the black solid line shows real seamount used in the calculations. The seamount area.

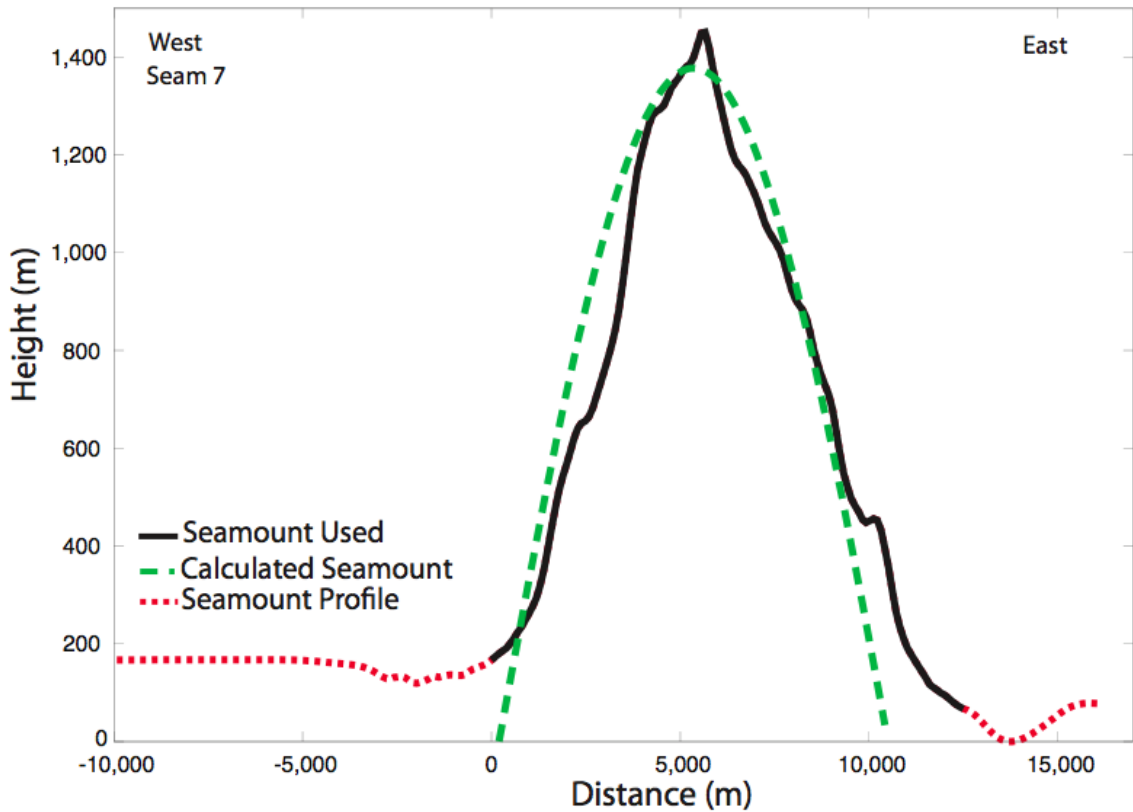


Figure 4.6. The cross-section of seamount #7 (dotted red line) is obtained from the 28.56 latitude line. The portion of the seamount that was used to calculate the total load and the seamount width is outlined by the solid black line. The green dashed line shows the theoretical seamount that was calculated.

4.4 Elastic Thickness Observations

The topography method was used to calculate the elastic thickness for all 12 of the seamounts. Figure 4.7 shows a graph that compares the volume of the seamounts with the elastic thickness obtained. The elastic thicknesses obtained for each seamount are within 1.5 km of each other giving an average value of 2.6 km. The maximum elastic thickness is 3158 m using seamount #1. The smallest elastic thickness in the area is 1605 m calculated from seamount #9. Seamount #7 has an elastic thickness of 3108 m. The median elastic thickness of all the seamounts is 2871 m and the average is 2640 m with a standard deviation of 519 m including both north-south and east-west profiles.

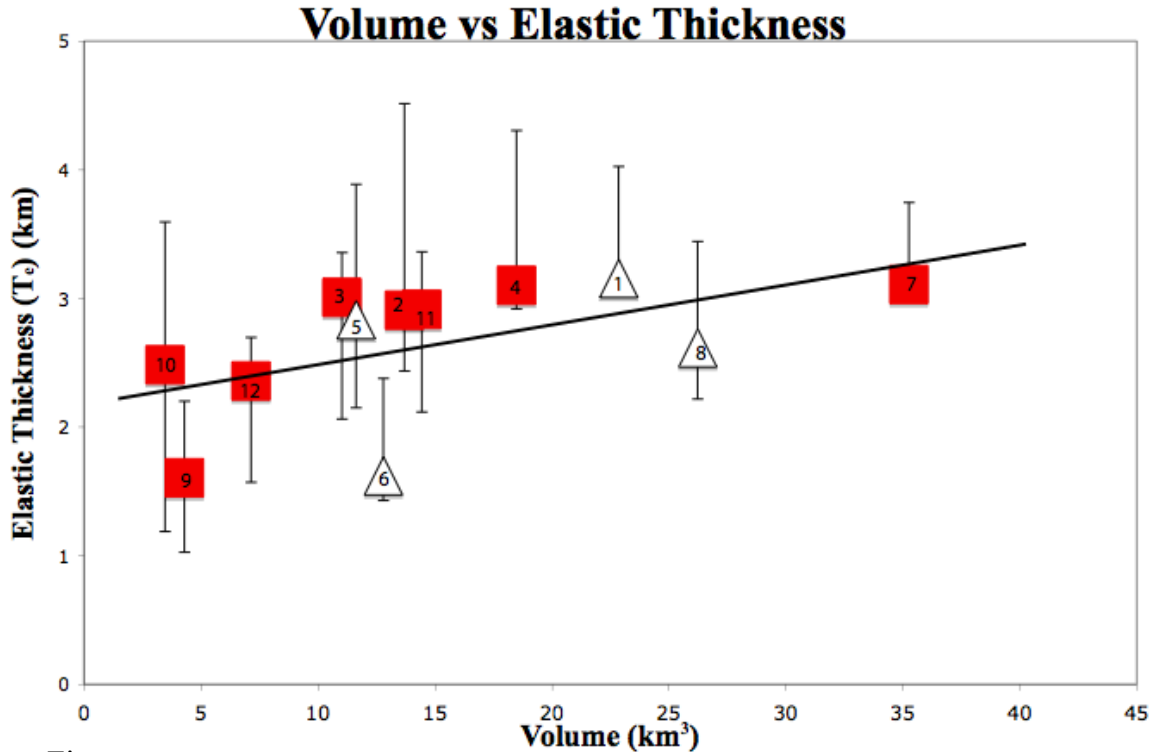


Figure 4.7. The elastic thickness obtained for each seamount as a function of the total volume. White triangles represent the seamounts that are elliptical in shape and the red squares indicate conical seamounts. Best fit for all points is given by black line. Error in the volume are smaller than the data point.

4.5 Deflection Depth and Other Graphs

4.5.1 Deflection Depth

I evaluate the deflection depth (w_0) with respect to the total volume of the seamount, which is plotted in Figure 4.8. The Deflection of the lithosphere increases linearly as a result of an increase in the volume of the seamount that produces the load. This reinforces the result in figure 4.7 above, which shows that T_e is within 1500 – 3500 m. If this is the case, then increasing the load should produce an increase in w_0 .

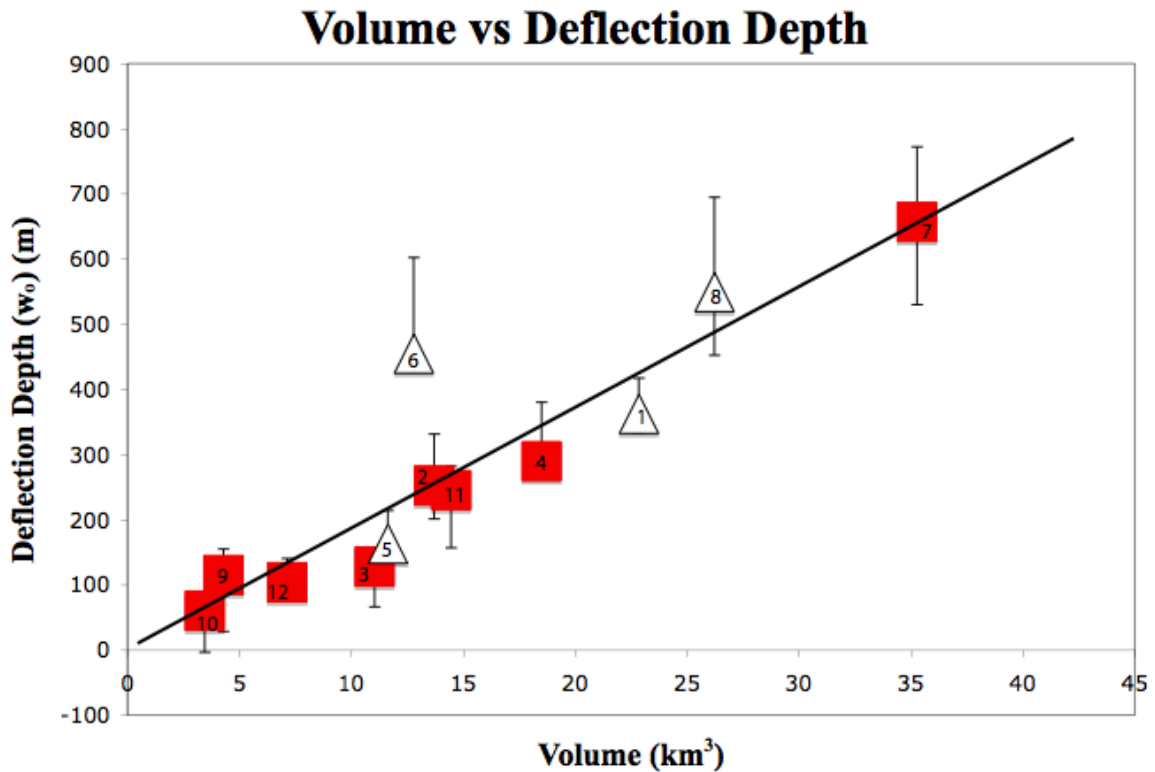


Fig 4.8. The deflection depth, w_0 is plotted as a function of total volume. The red boxes represent the conical seamounts whereas the white triangles are elliptical ones. Error in the volume are smaller than the data point.

4.5.2 Volume and Moat Radius

In general, the moat radius (mx_b) is observed to increase with increasing seamount volume as shown in Figure 4.9. The graph shows some scatter in the data with mx_b varying from 7 km to 10.5 km for a single volume at 12 km³. The symbols (designated by seamount shape for conical and elongated seamounts) do not seem to correlate with the different slopes. However, with the exception of a few points, seamounts in the western array seem to plot higher giving higher moat radii for a given volume compared to the eastern array. One possible explanation is that I have underestimated the measured moat radius (mx_b) due to sedimentation, which obscure our view of the bathymetry. There exists a possibility that the volume estimations for the seamount have been underestimated due to the lack of incorporation of sediments present

in the moats. However, the sediment loading would occur at a much slower rate and would not affect the loading of the seamount. If the loading of the sediments were to be included, the deflection of the lithosphere would be greater than I have calculated in this study, thus reducing the elastic thicknesses that are computed. The two possible groups of moat radius may be indistinguishable with the error bars shown.

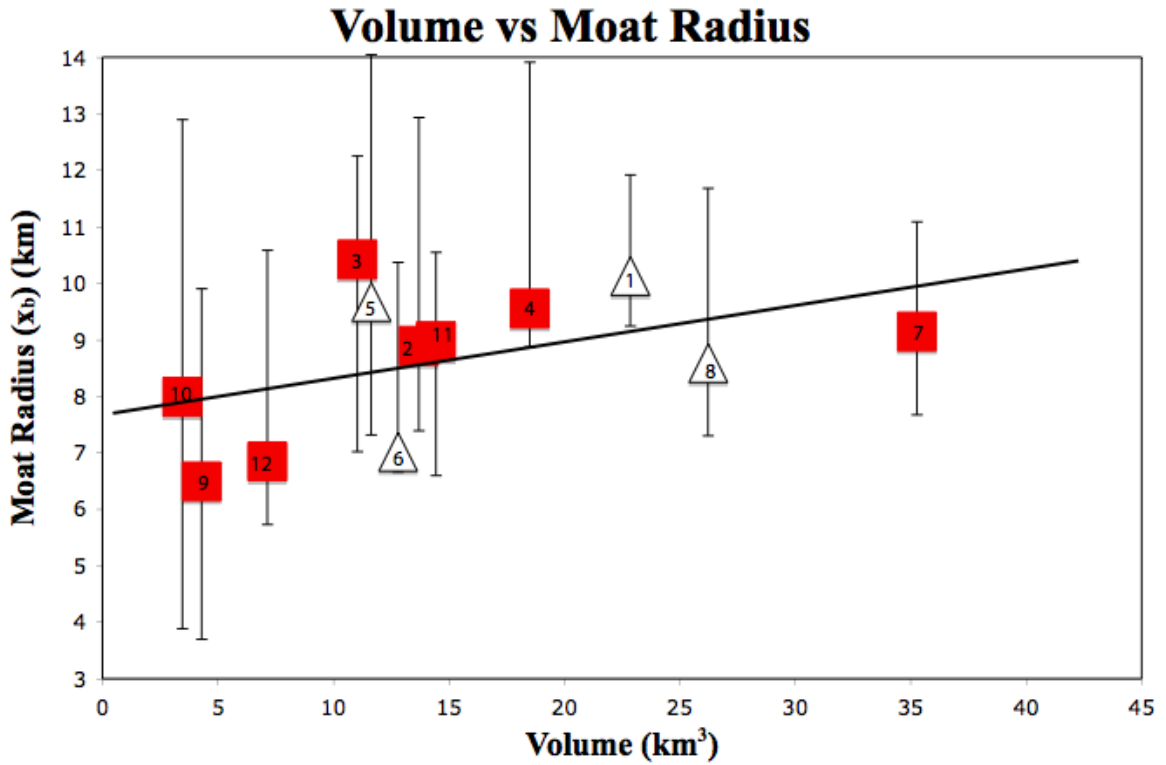


Figure 4.9 The measured moat radius (x_b) is shown as a function of total volume of the seamount. There is an increase in the moat radius with increasing volume. Red squares represent circular seamounts and white triangles are elliptical. The error of the volume is smaller than the points

Chapter 5 DISCUSSION

5.1 Age Determination

Our results indicate that the elastic thickness, T_e , for all 12 of the seamounts in our study area varies from 1.5 to 3.5 km. Values of elastic thickness should not change based solely on changes in mass or load. I observe a slight increase in our elastic thickness in comparison as a response to volume. This suggests that all the seamounts in this study formed at the same time period on seafloor that was less than 10 Ma. The seafloor age at the time of seamount formation was much younger than where they are observed today.

I estimate the age of the seafloor in which these seamounts formed based on cooling models for the lithosphere (Parsons and Sclater, 1977). The age estimate of the lithosphere is based on elastic thickness estimated from a compilation of many studies of seamounts and loading throughout the Pacific and other global ocean basins (Watts, 2001; m Kalinins and Watts, 2009). These empirical data have been used to establish a robust correlation between these two variables. The elastic thickness can be estimated by the 300-600° C isotherms for young seafloor in the oceanic mantle, with more than 75% of all data points plot in this range (Watts, 2001). Using this relationship, I infer that the seamounts were emplaced on lithosphere that was less 10 Ma. Our results are clearly shown in figure 5.1 between 150° and 300 °C isotherms. The ages obtained using this relationship are illustrated in figure 5.1.

The age of the lithosphere at time of loading was 10 Ma, and its present age is roughly 150 Ma. This suggests that the lithosphere has cooled and thickened in a normal manner for approximately 140 million years.

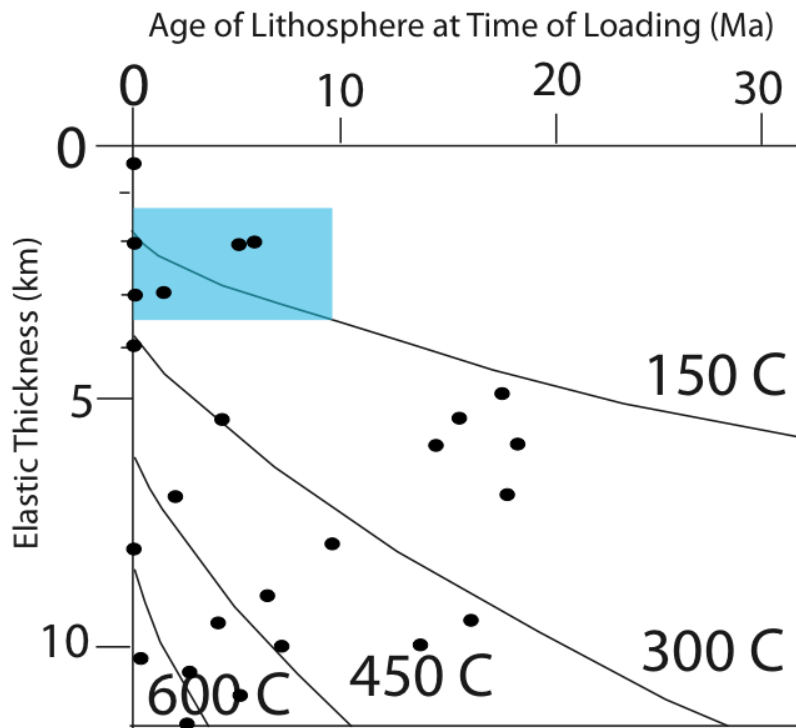


Figure 5.1 The elastic thicknesses obtained are thin (1.5 – 3.5 km). The ages that these thicknesses represent ocean floor 10 Ma. at time of emplacement. The black dots represent elastic thicknesses vs. ages obtained from different studies compiled in Watts, 2001. Figure modified from Watts, 2001.

5.2 Abyssal Hill Integrity

The abyssal hills observed are undisturbed in the western array. On the eastern array they are less noticeable. Based on the hill geomorphology inside the arrays, the ocean floor has not been disturbed by magmatism or large events of tectonism. The only episode of magmatism observed are the small seamounts for which I show results here. The young age of the lithosphere at which the seamounts formed has allowed normal growth of the lithosphere after the formation of the seamounts.

5.3 Larger Perimeter Seamounts

The focus of our study was the small seamounts found within the two arrays. However, the bathymetry in figure 1.4 shows several large seamounts (explained in section 2.1.2) that are located outside of the perimeters that bind our study area. Although

these seamounts are three times as tall than the ones observed within the arrays, they do not show a visible moat around them. This implies that the seamounts were formed at a later time when the lithosphere was strong enough to support the load and not flex.

The age of the seafloor at the time of loading of these seamounts must be old enough to support their load as opposed to the seamounts found within the area. This implies that episodes of volcanism occurred after the formation of the small seamounts. However, these events are sufficiently removed from our area that these anomalies did not influence our study area.

CHAPTER 6 CONCLUSIONS

5.1 Conclusions

This study presents evidence that the elastic thickness of the lithosphere was in the range of 1500 m to 3500 m at the time in which the loading of the seamounts occurred. I then inferred an age of loading based on these elastic thicknesses calculated. All of the seamounts used in this study have an age of emplacement that is younger than 10 Ma. I also observed larger seamounts that are found outside the two main areas of interest. However, these seamounts are sufficiently far from the area that they would not disrupt the natural cooling and growth of the lithosphere within the two arrays.

Abyssal hills found on the field area are a very pronounced feature of the ocean floor in the western array, and more faint in the eastern array. The hills are continuous and well formed. No major faulting or offsets of the hills is observable. McDonald, et al., 1996 found that the abyssal hills form within 2-5 km from the ridge making them an early feature of the ocean floor. The abyssal hills in the study area parallel the magnetic lineations found their respective locations. The magnetic lineations are one of the earliest features that are formed on the ocean floor. As observed in Figure 1.4, the magnetic lineations are continuous within the two main areas of interest.

5.2 Implications for PLATE Study

The most important implication for the PLATE study is that I addressed all of the features of the ocean floor that could potentially disrupt the natural growth of the lithosphere. The seamounts used here, were found to be emplaced 10 Ma and therefore, they have not interfered with the growth of the lithosphere for the past 140 m.y. The large

seamounts in the area are found outside of the main areas of interest for the PLATE study and do not immediately interfere with the normal progression of the lithosphere. Clear abyssal hills were found on the western array of the study area and more obscured (buried?) in the eastern array. The hills parallel the magnetic lineations in their respective area. Both of these features are formed at a very early stage after the ocean floor forms. The great conditions in which both of these features are found are a testament to the relative tectonic and volcanic inactivity found in the field area. I then propose that the field area is an ideal place in which normal lithospheric growth can be studied.

REFERENCES

- Buck, W. Roger and Poliakov, Alexei, N. B. , 1998. Abyssal Hills Formed by Stretching Oceanic Lithosphere. *Letters to Nature*. Vol. 392, pp. 272-275
- Calmant, S., Francheteau, J., and Cazenave A., 1990. Elastic Layer Thickening With Age of the Oceanic Lithosphere: a Tool For Prediction of the Age of Volcanoes or Oceanic Crust. *Geophysical Journal International*. Vol. 100, pp. 59-67
- Kalnins, L.M. and A. B. Watts, 2009. Spatial Variations in Effective Elastic Thickness in the Western Pacific Ocean and Their Implications for Mesozoic Volcanism. *Earth and Planetary Science Letters*. Vol. 286, pp. 89-100
- Mcdonald, Ken C., Fox, P. J., Alexander, Russ T., Pockanly, Robert and Gente Pascal, 1996. Volcanic Growth Faults and the Origin of Pacific Abyssal Hills. *Letters to Nature*. Vol. 380, pp. 125-129.
- Muller, R. Dietmar, Roest, Walter R., Royer, Jean-Yves, Gahagan, Lisa M. and Sclater, John G., 1997. Digital Isochrons of the World's Ocean. *Journal of Geophysical Research*. Vol. 102, No. B2, pp. 3211-3214.
- Nakanishi, M., Tamaki, K. and Kobayashi, K., 1992. Magnetic Anomaly Lineations from Late Jurassic to Early Cretaceous in the West-Central Pacific Ocean. *Geophysical Journal International*. Vol. 109, pp. 701-719.
- Oikawa, M., Kaneda, K., Nishizawa, A., 2010. Seismic Structures of the 154–160 Ma Oceanic Crust and Uppermost Mantle in the Northwest Pacific Basin. *Earth Planets Space*. Vol. 62, pp. e13-e16.
- Parsons, Barry and Sclater, John G., 1977. An Analysis of Ocean Floor Bathymetry and Heat Flow with Age. *Journal of Geophysical Research*. Vol. 82, No. 5, pp. 803-827.
- Shinohara, M., Fukano, T., Kanazawa, T., Araki, E., Suyehiro, K., Mochizuki, M., Nakahigashi, K., Yamada, T. and Mochizuki, K., 2008. Upper Mantle and Crustal Seismic Structure Beneath the Northwestern Pacific Basin Using a Seafloor Borehole Broadband Seismometer and Ocean Bottom Seismometers. *Physics of the Earth and Planetary Interiors*. Vol. 170, pp. 95-106.
- Smith, Walter H. F. and Sandwell, David T., 1997. Global Sea Floor Topography from Satellite Altimetry and Ship Depth Soundings. *Science*. Vol. 277, pp. 1956-1952.
- Turcotte, Donald L., and Schubert, Gerald, 2002. *Geodynamics*: New York, Cambridge University Press, 456 p.

Watts, A. B. 2001, *Isostasy and Flexure of the Lithosphere*: New York, Cambridge University Press, 459 p.

Wessel, Pal, 1996. Analytical Solutions for 3-D Flexural Deformation of Semi-Infinite Elastic Plates. *Geophysical Journal International*.

APPENDIX A

Maps of seamounts (a) that have the moat radius (x_b) inferred moat (dashed line) and visible moat (solid line). The portion of the map that was used for volume calculations is shown (b and c).

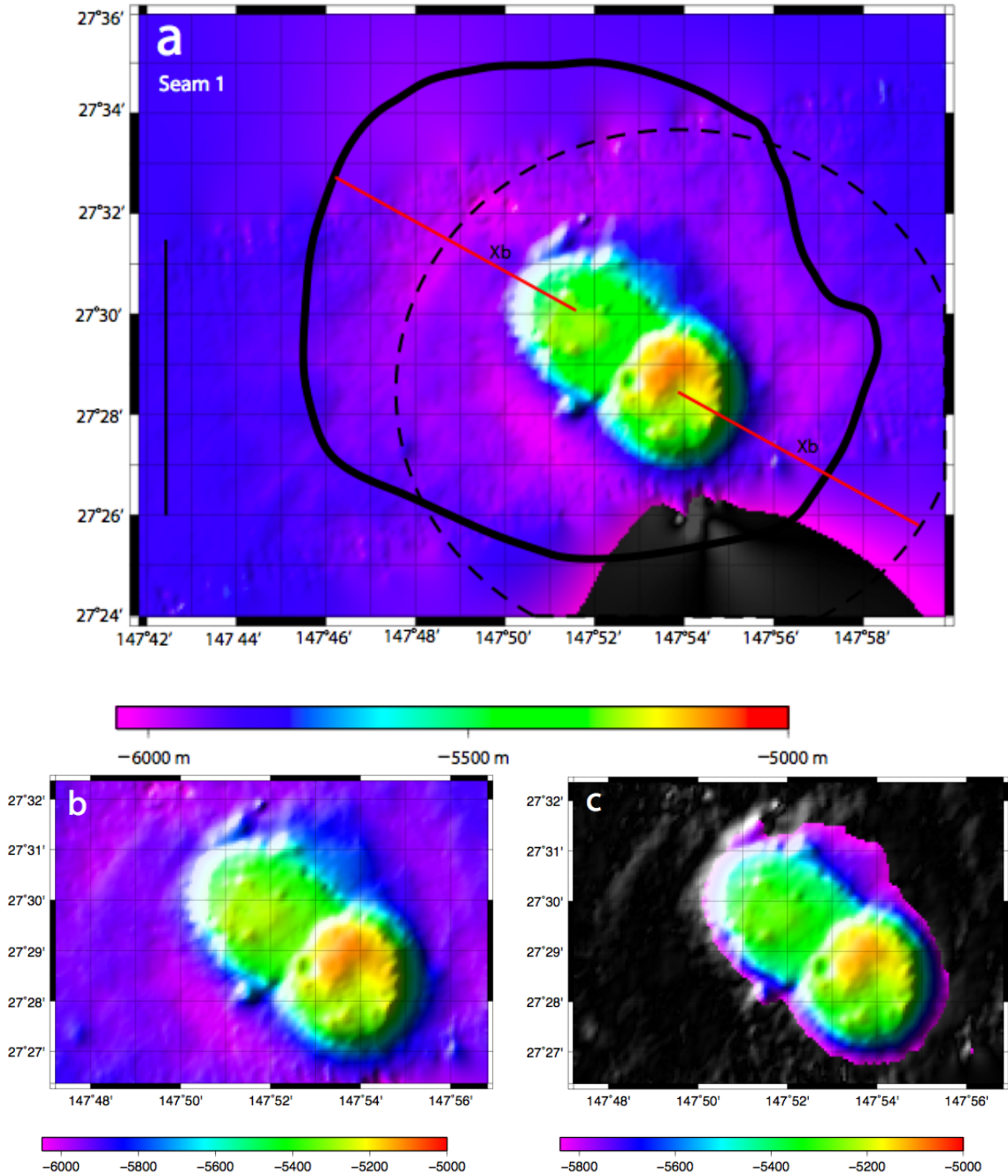


Figure A.1

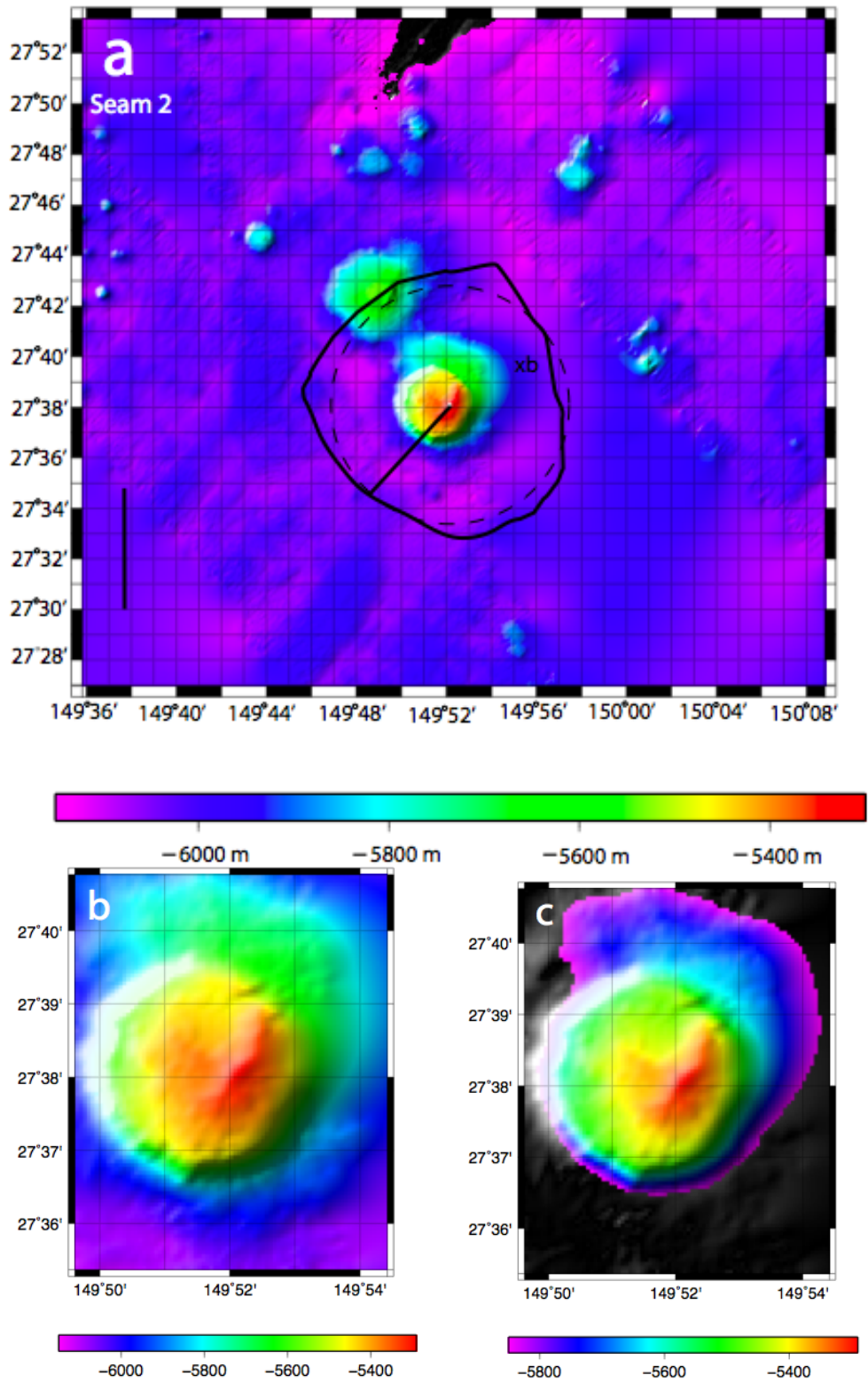


Figure A.2

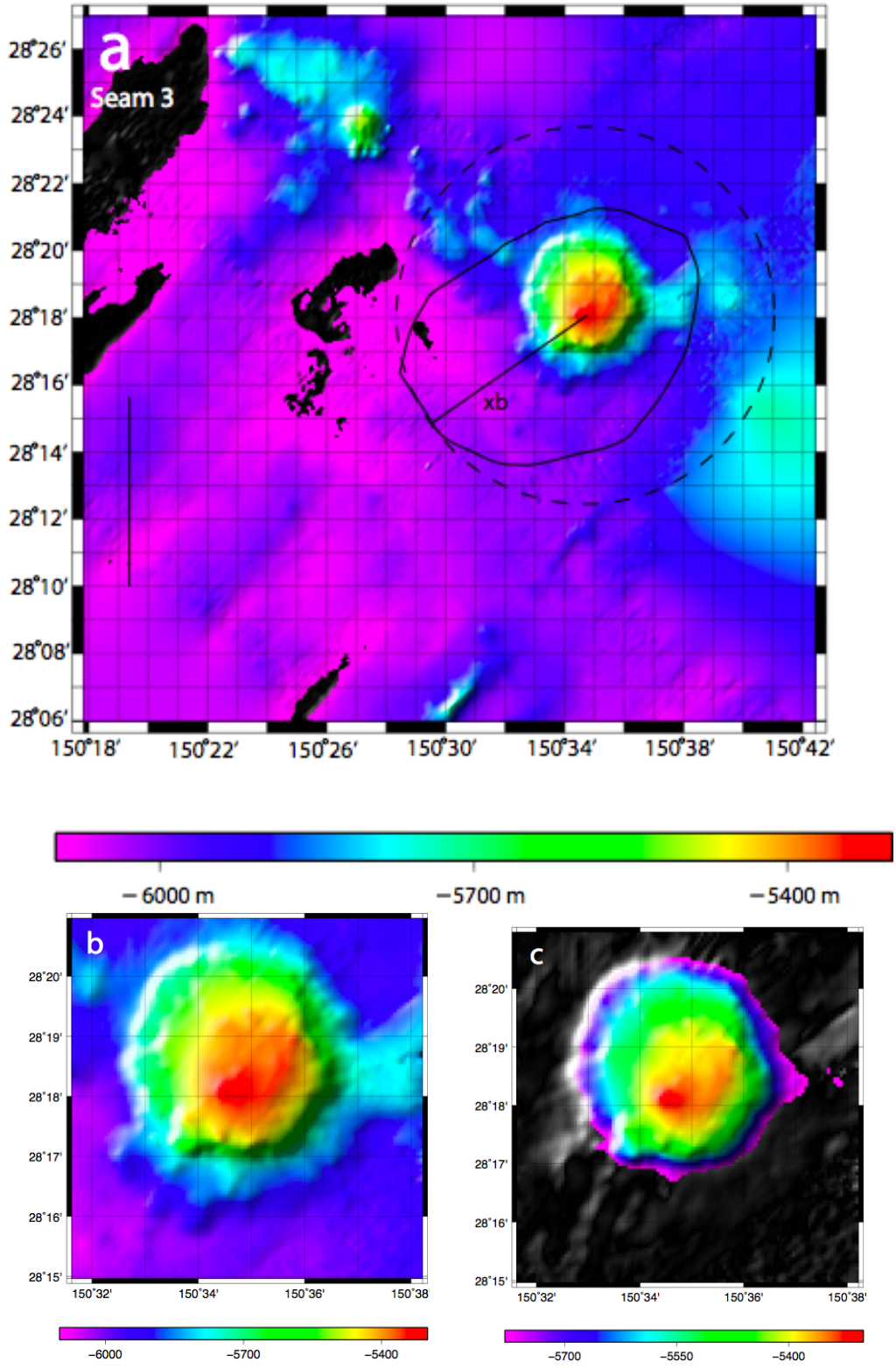


Figure A.3

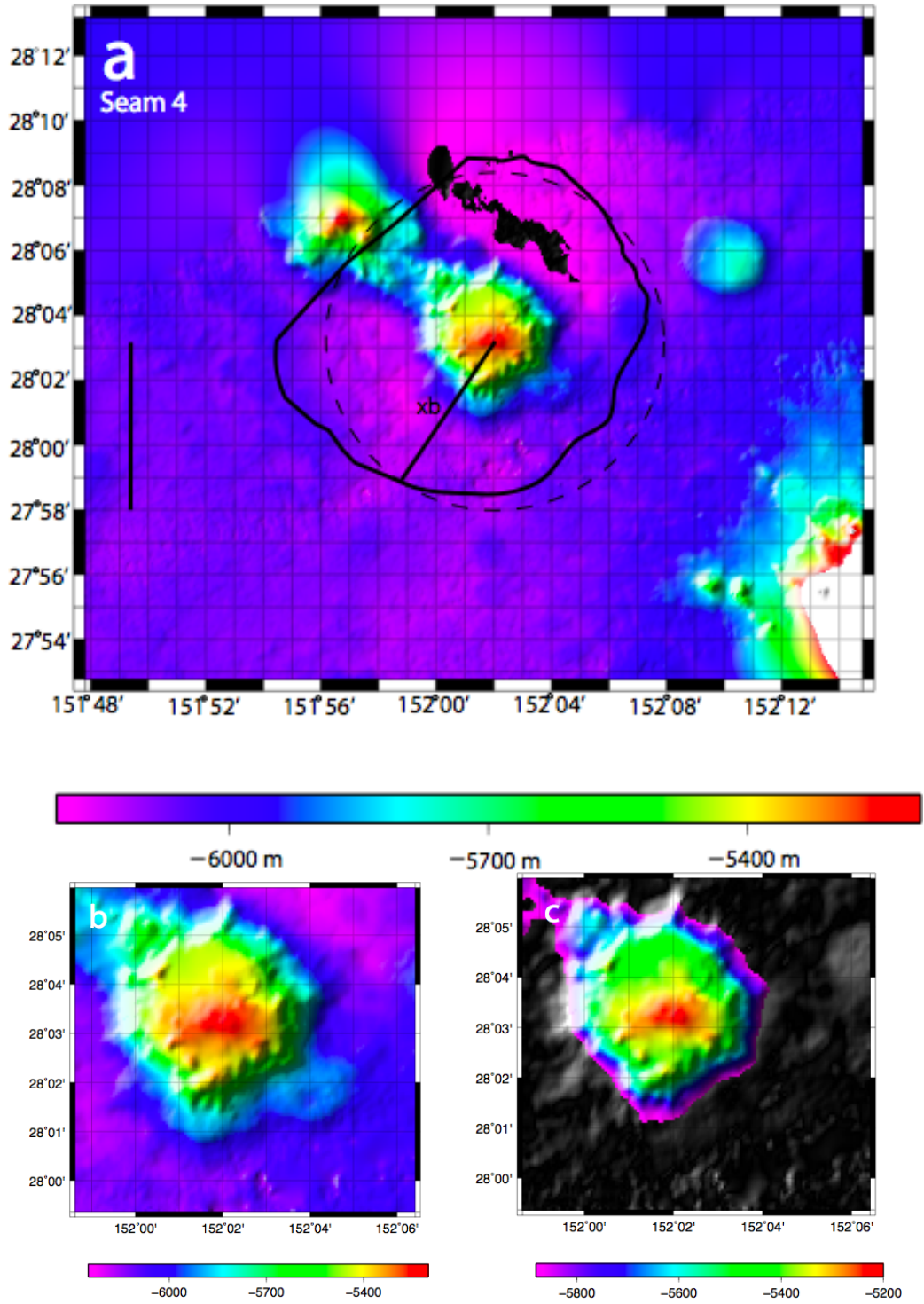


Figure A.4

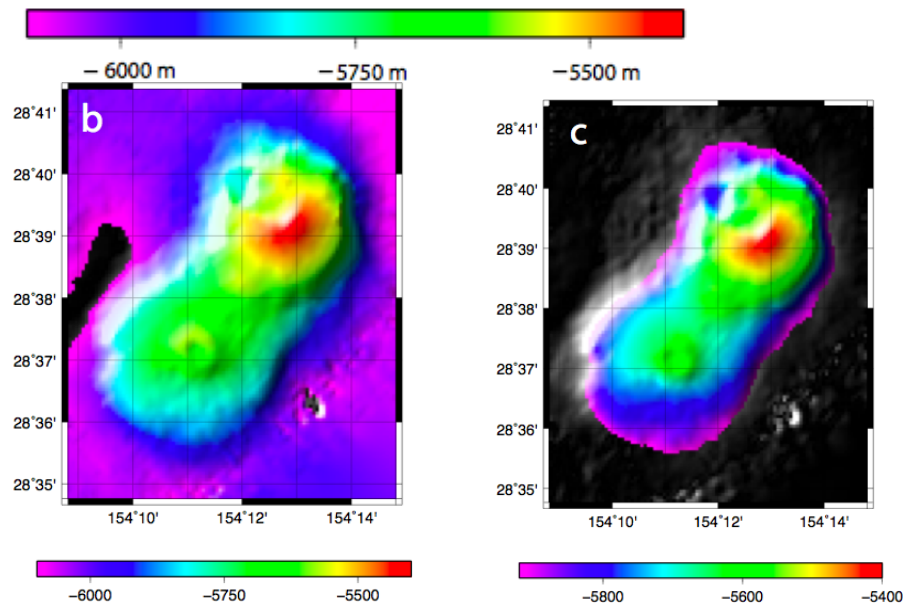
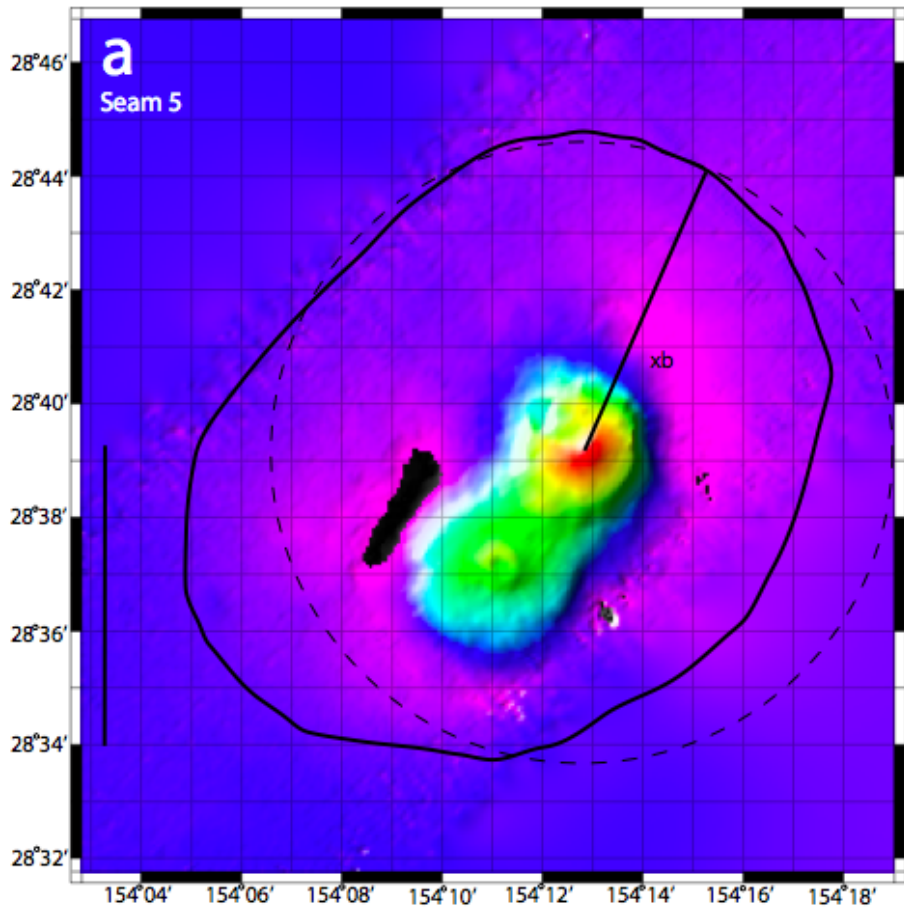


Figure A.5

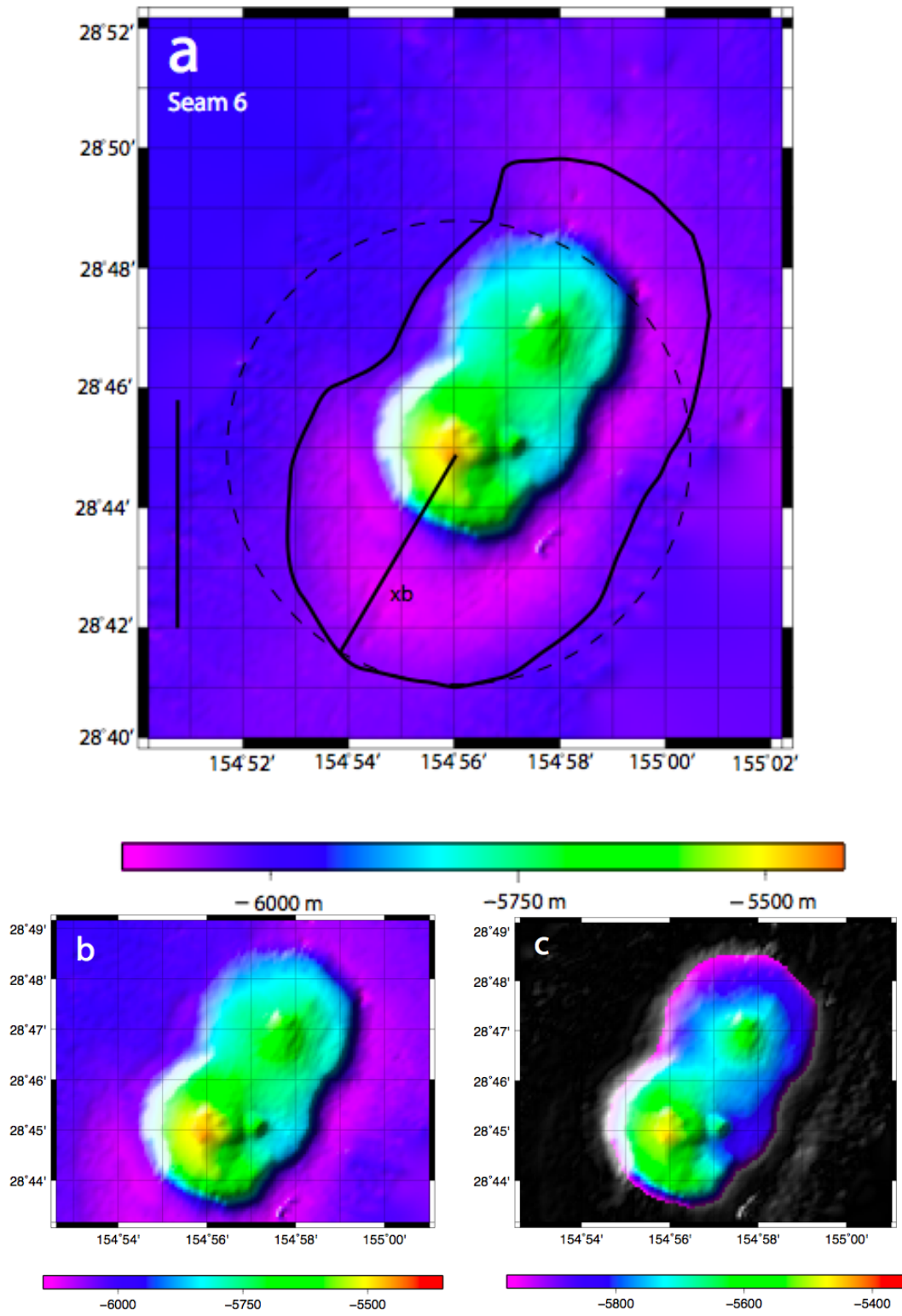


Figure A.6

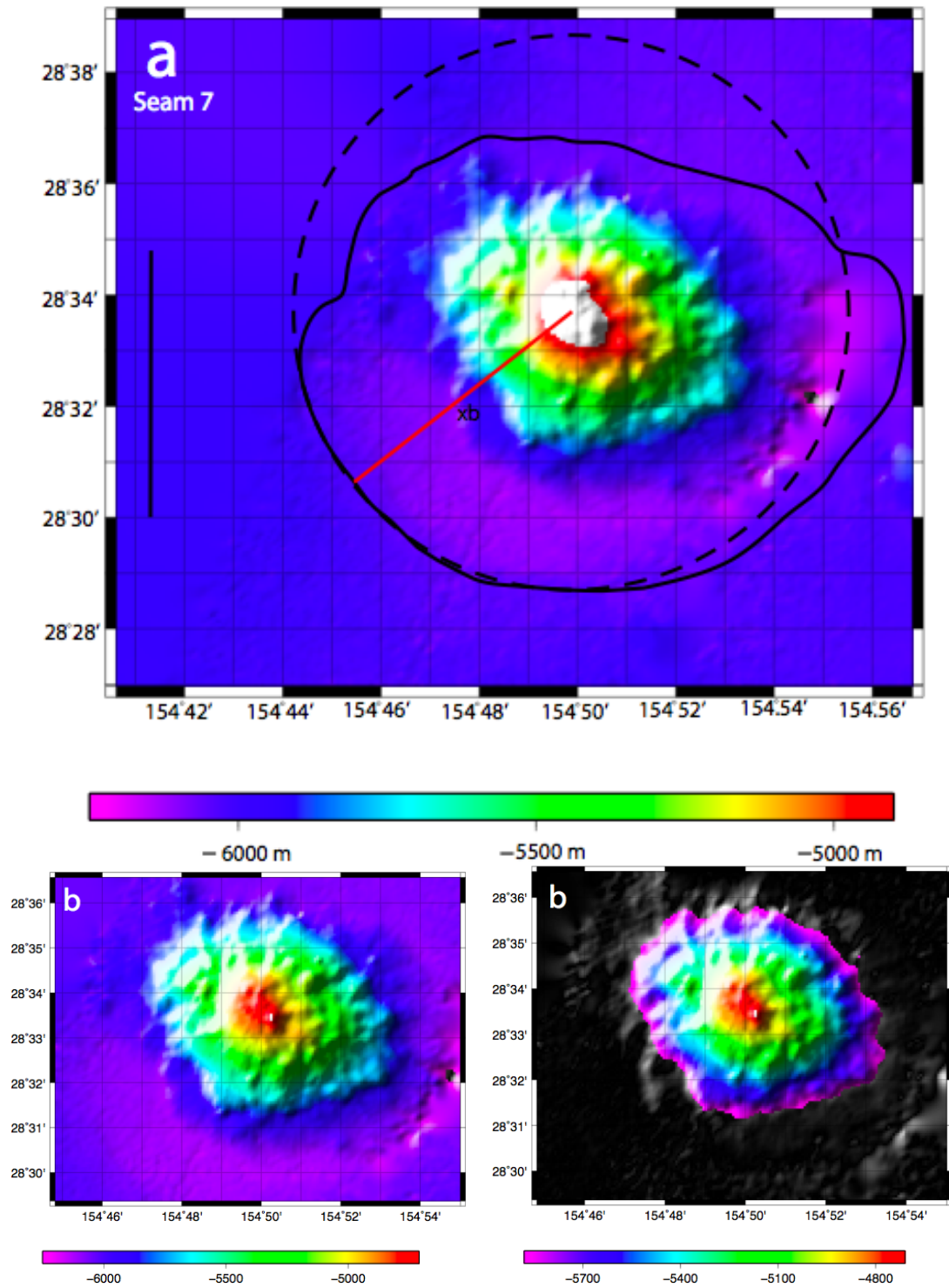


Figure A.7

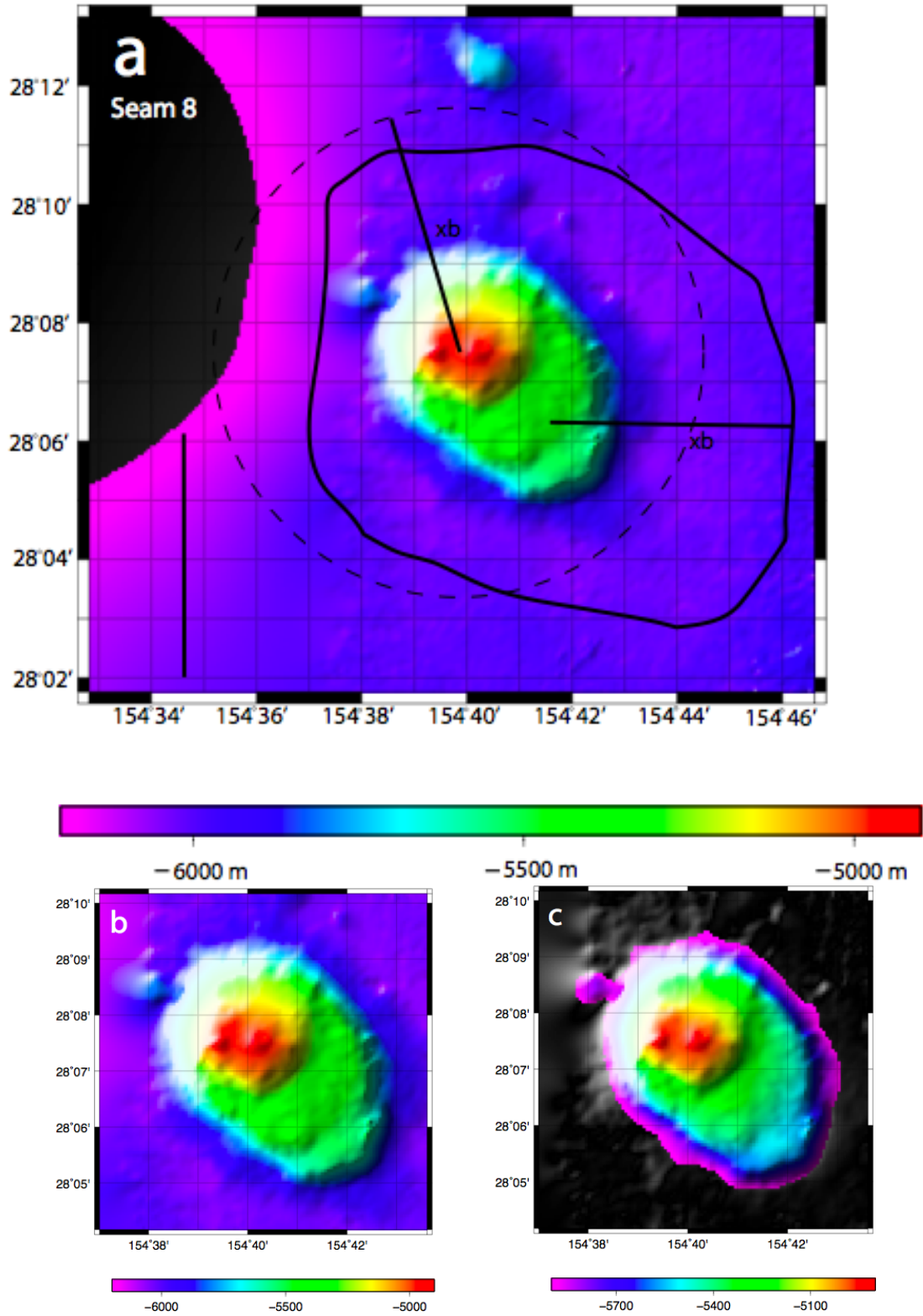
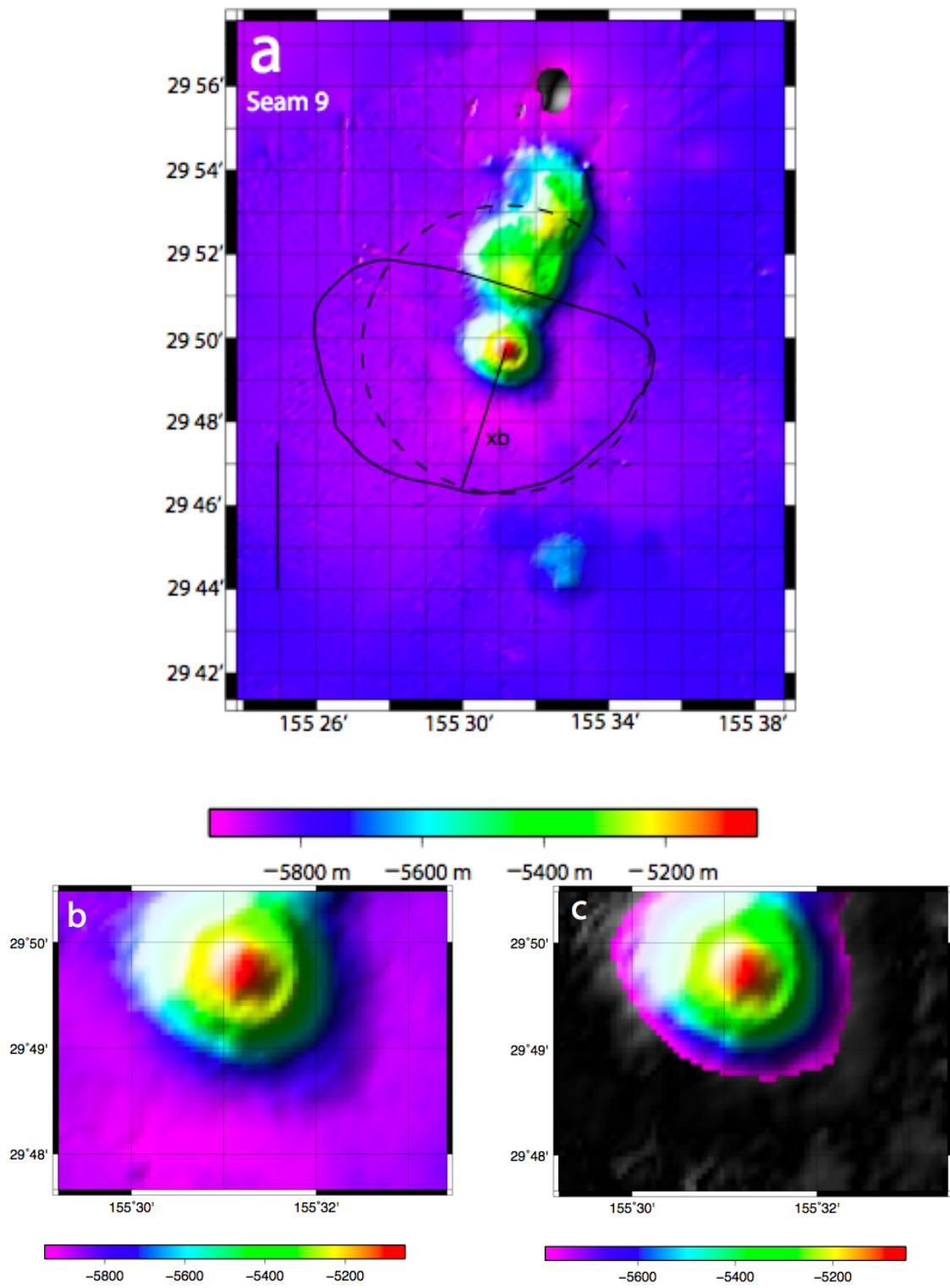


Figure A.8



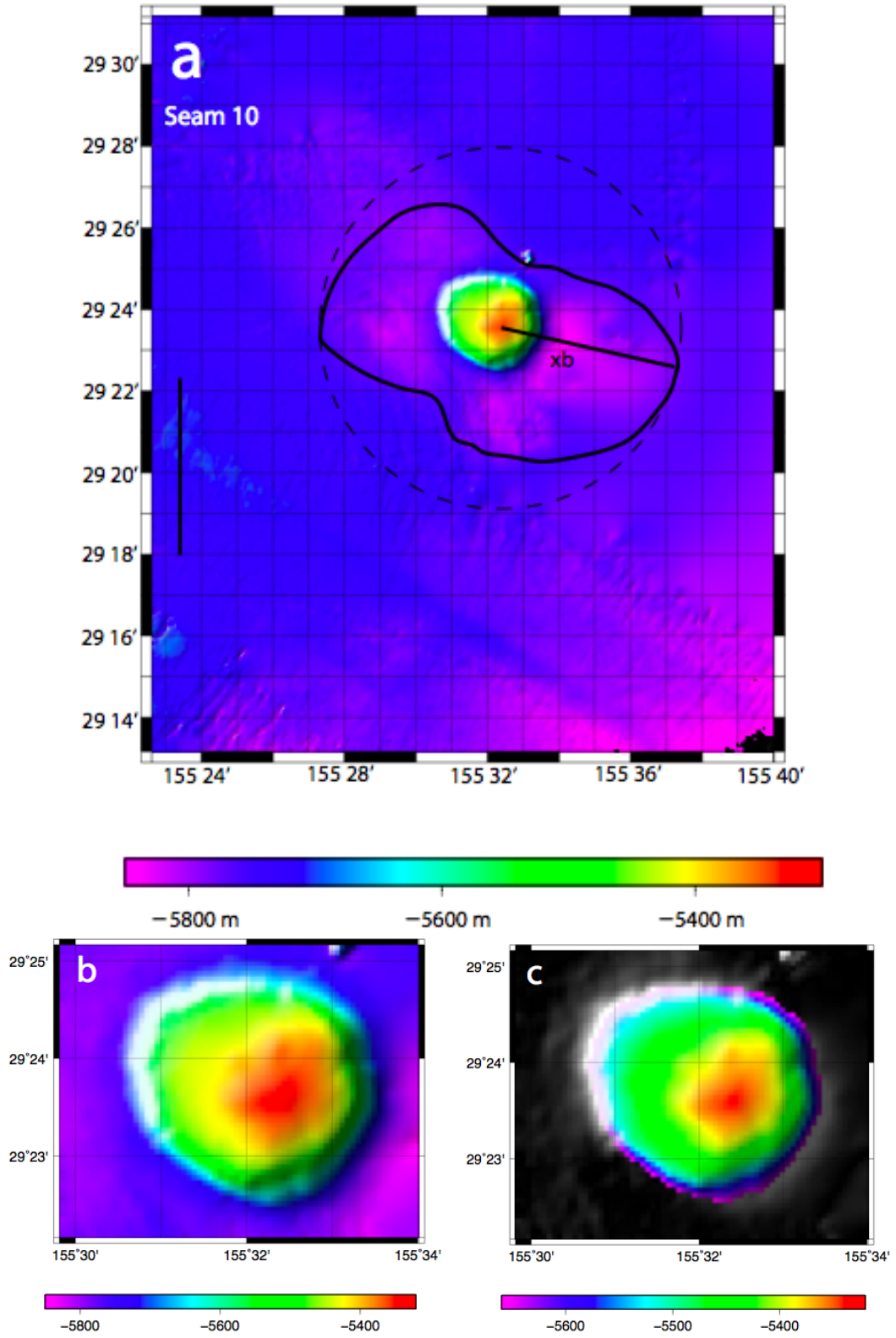


Figure A.10

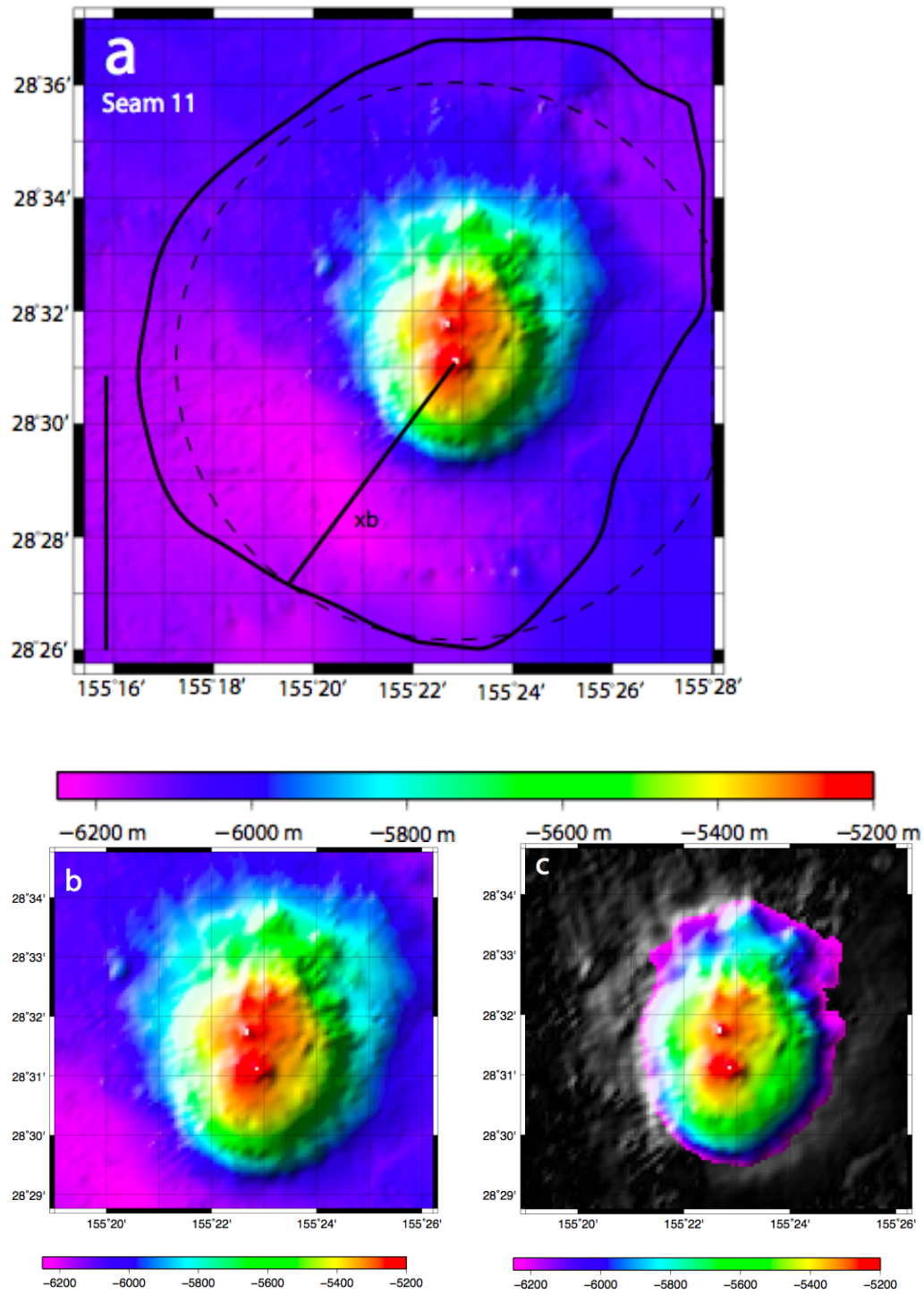


Figure A.11

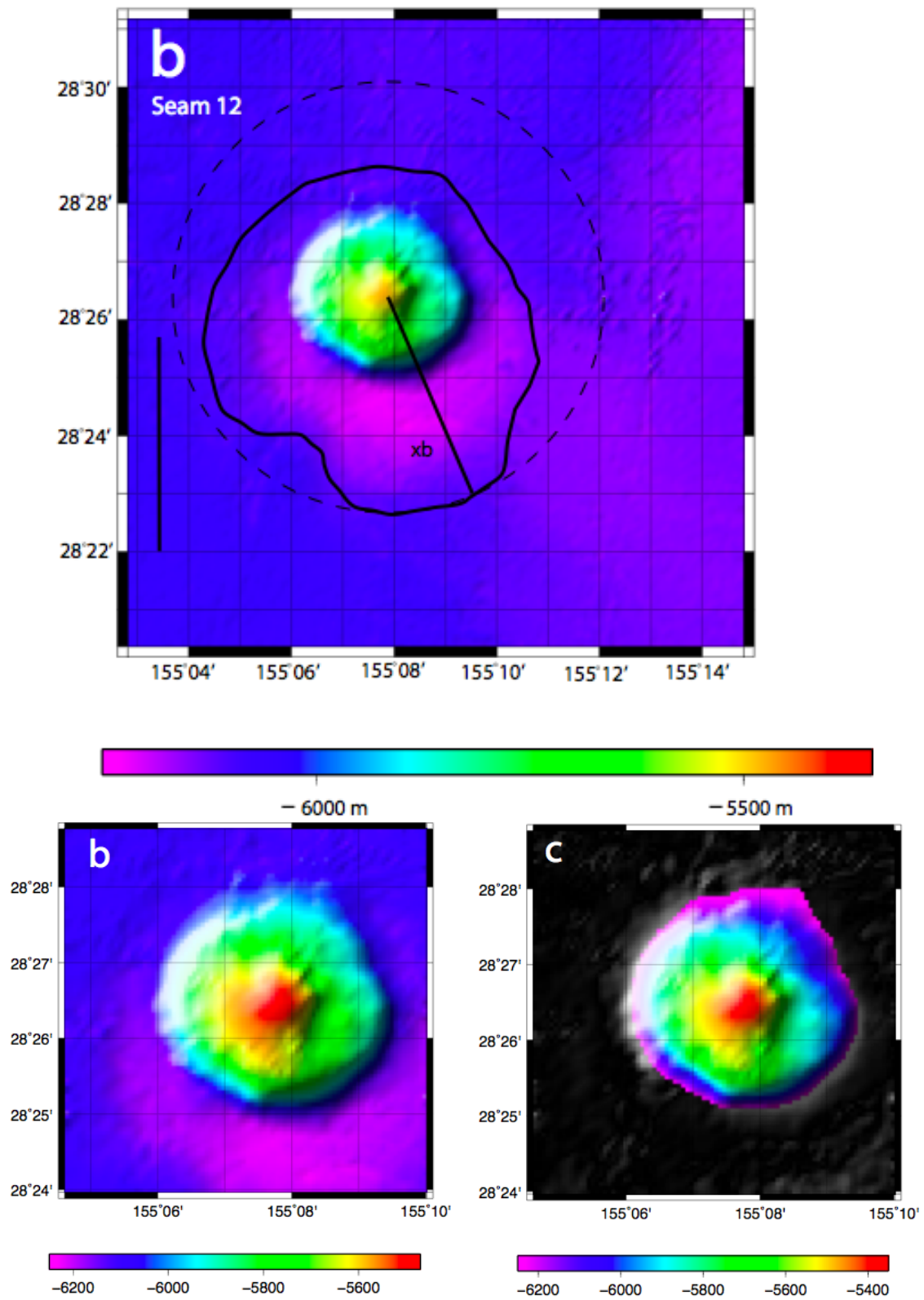


Figure A.12

APPENDIX B

Deflection profiles for all the seamounts.

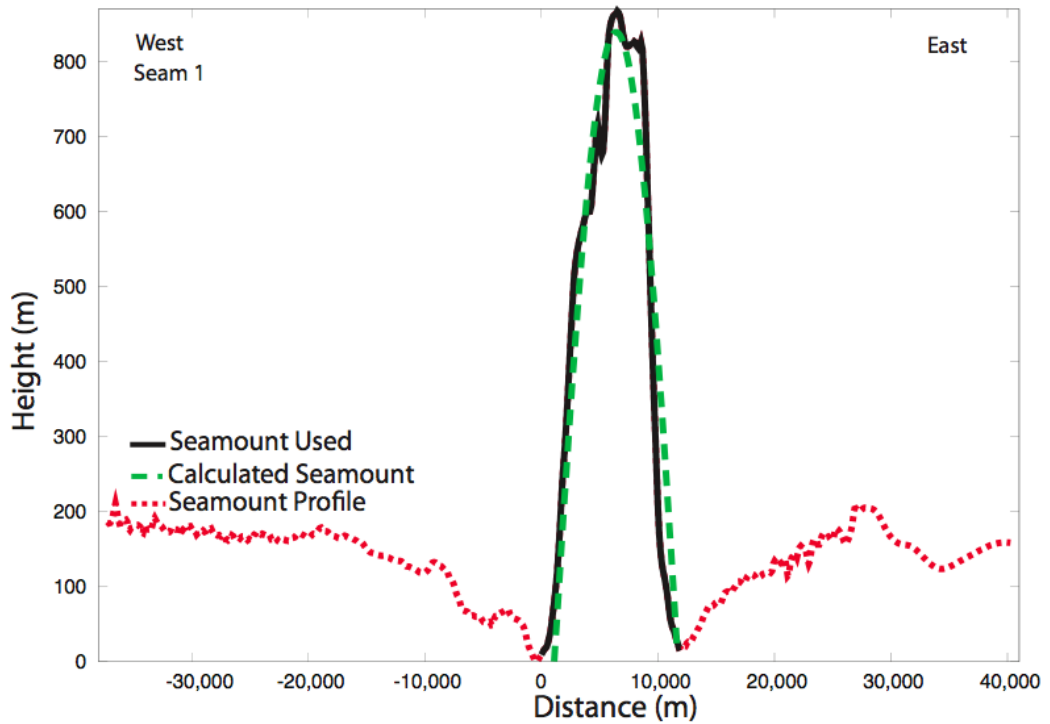
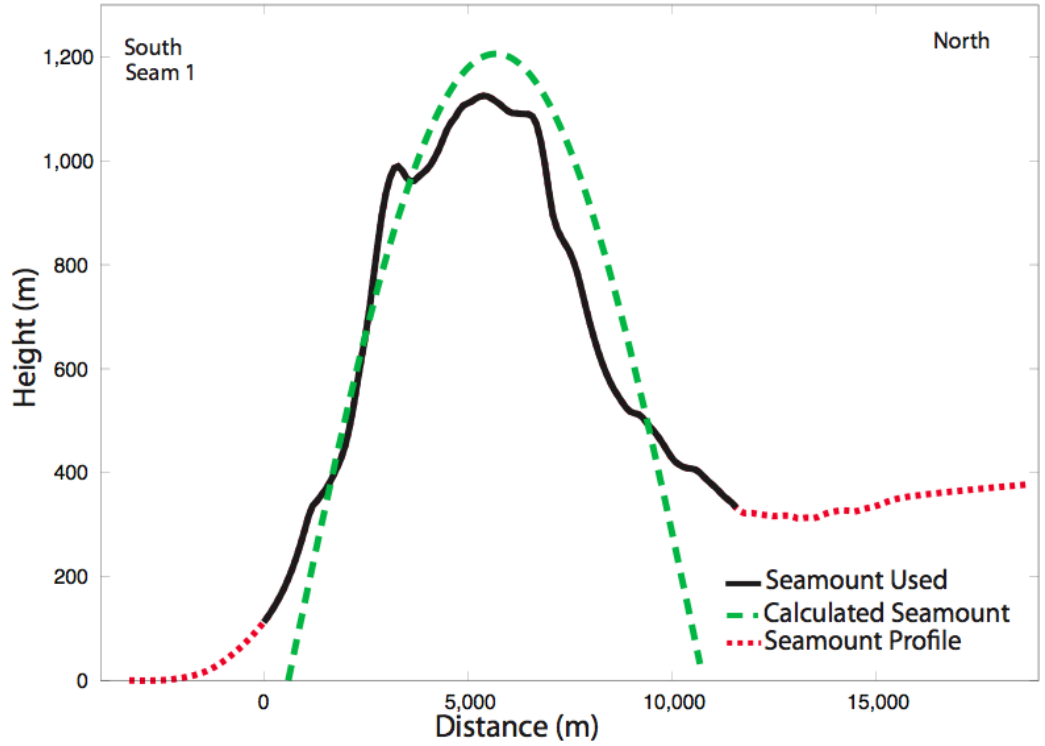


Figure B.1

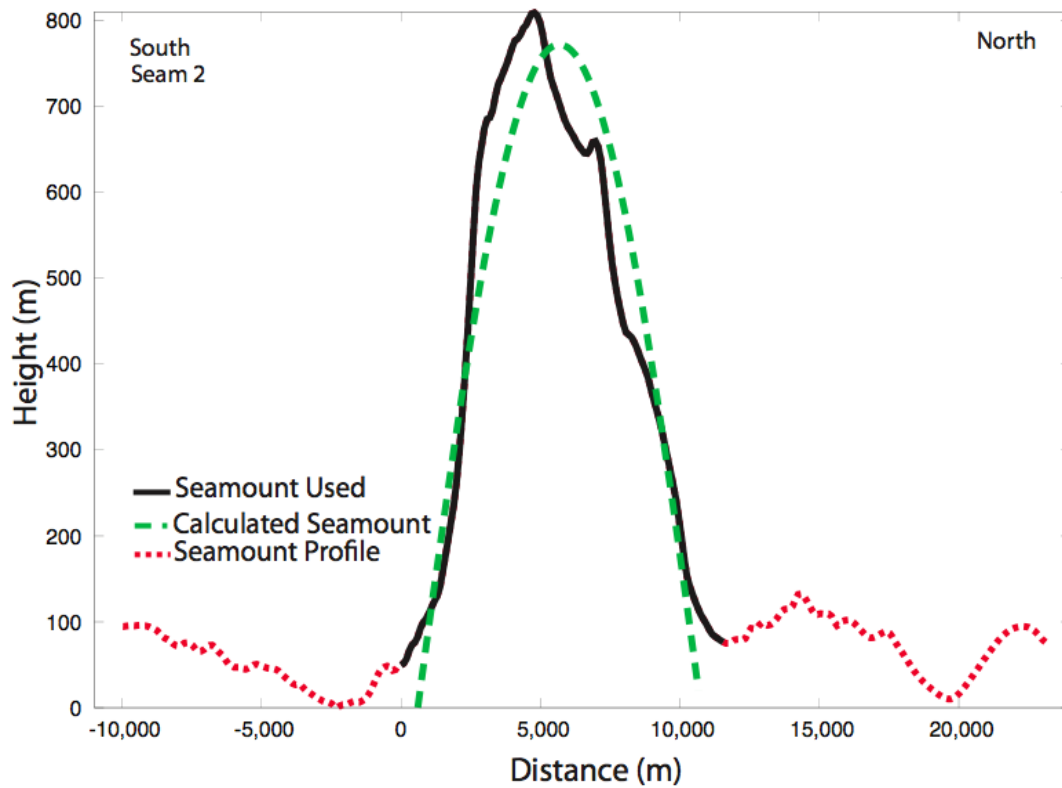
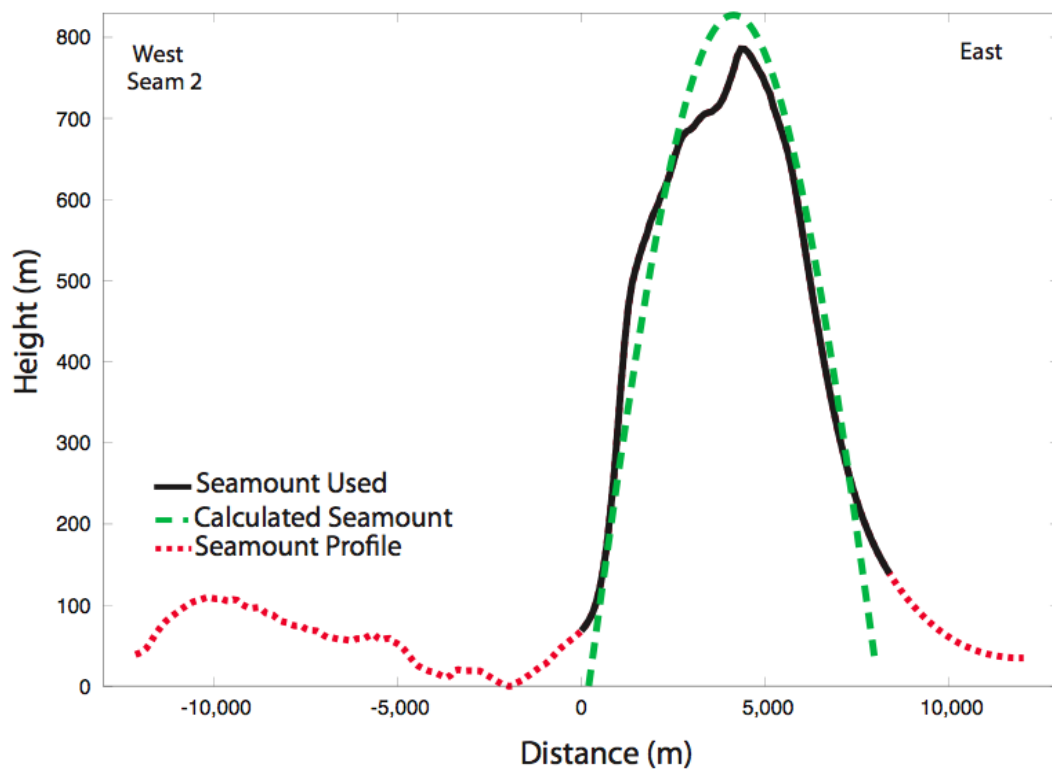


Figure B.2

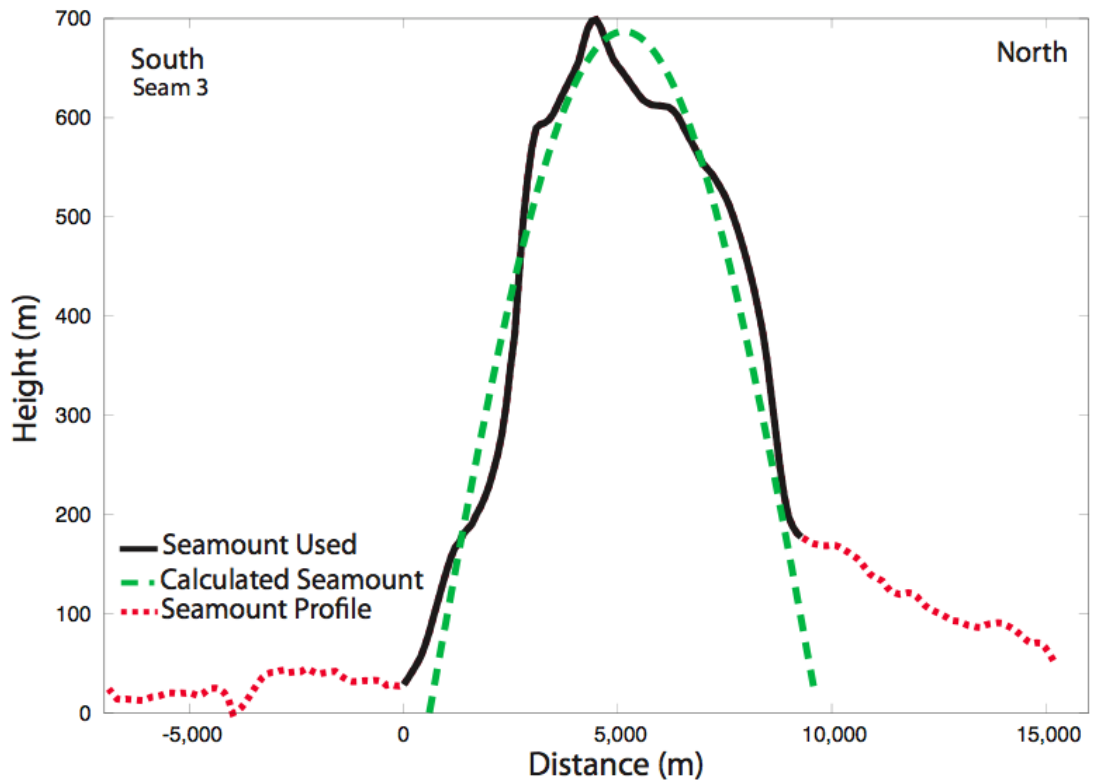
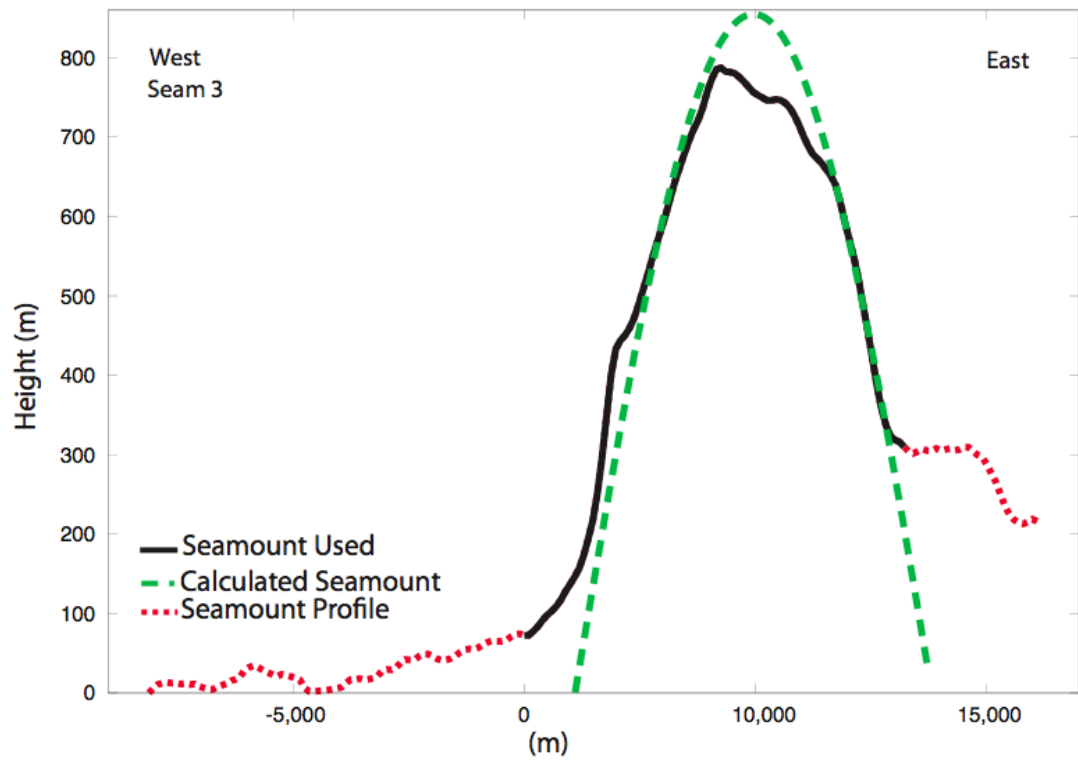


Figure B.3

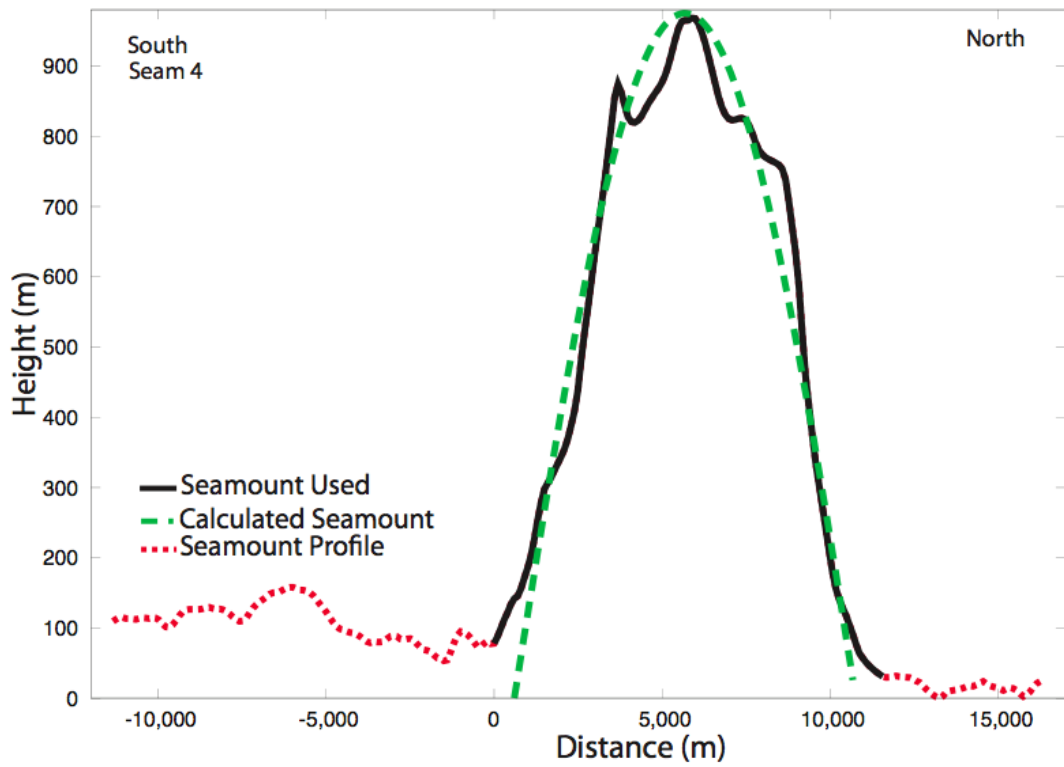
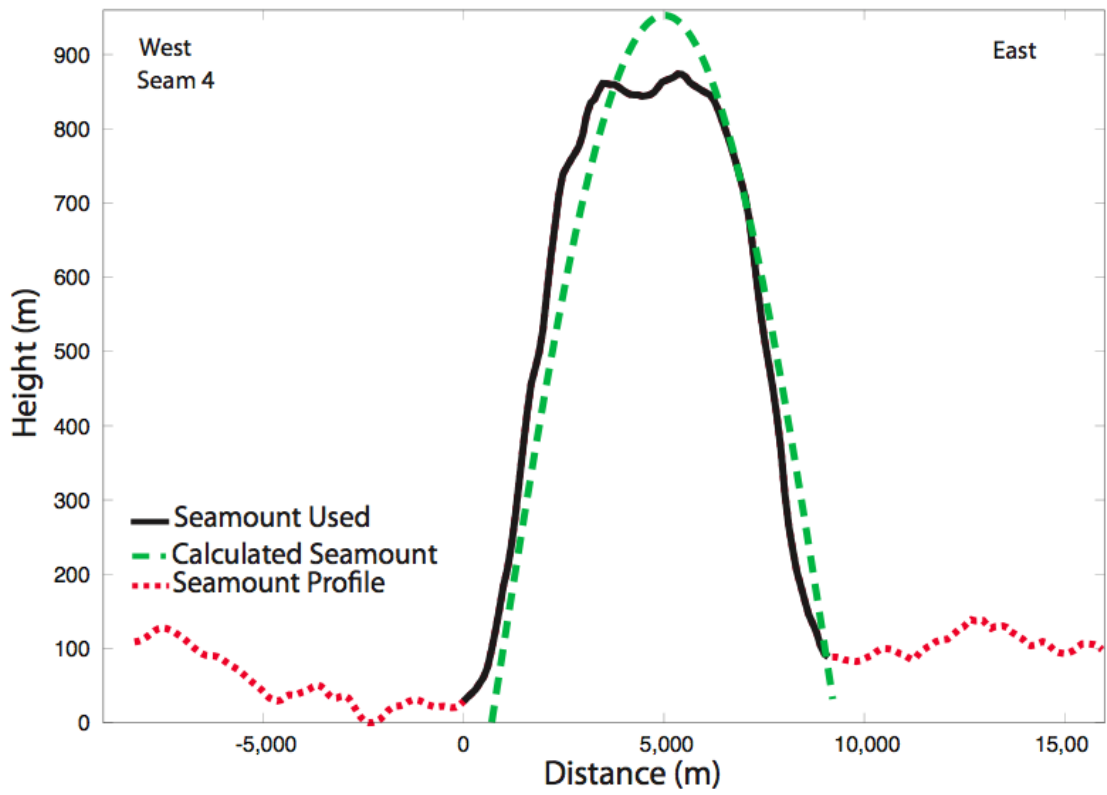


Figure B.4

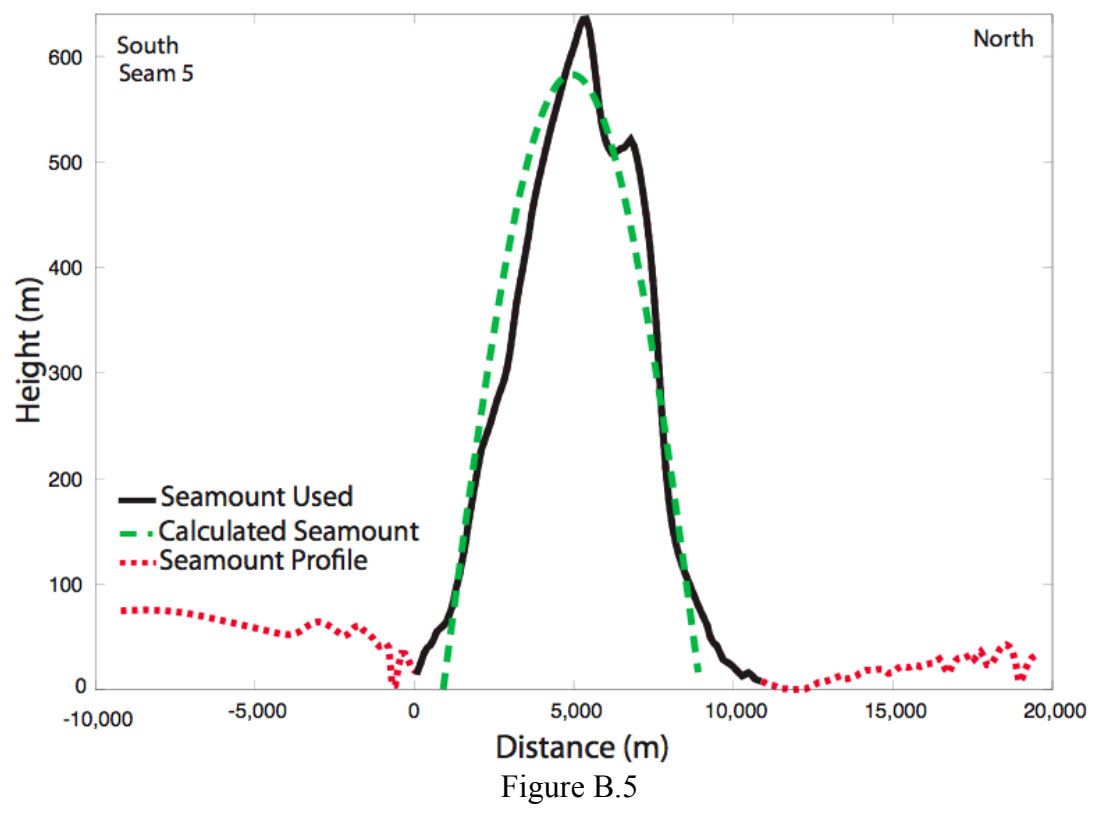
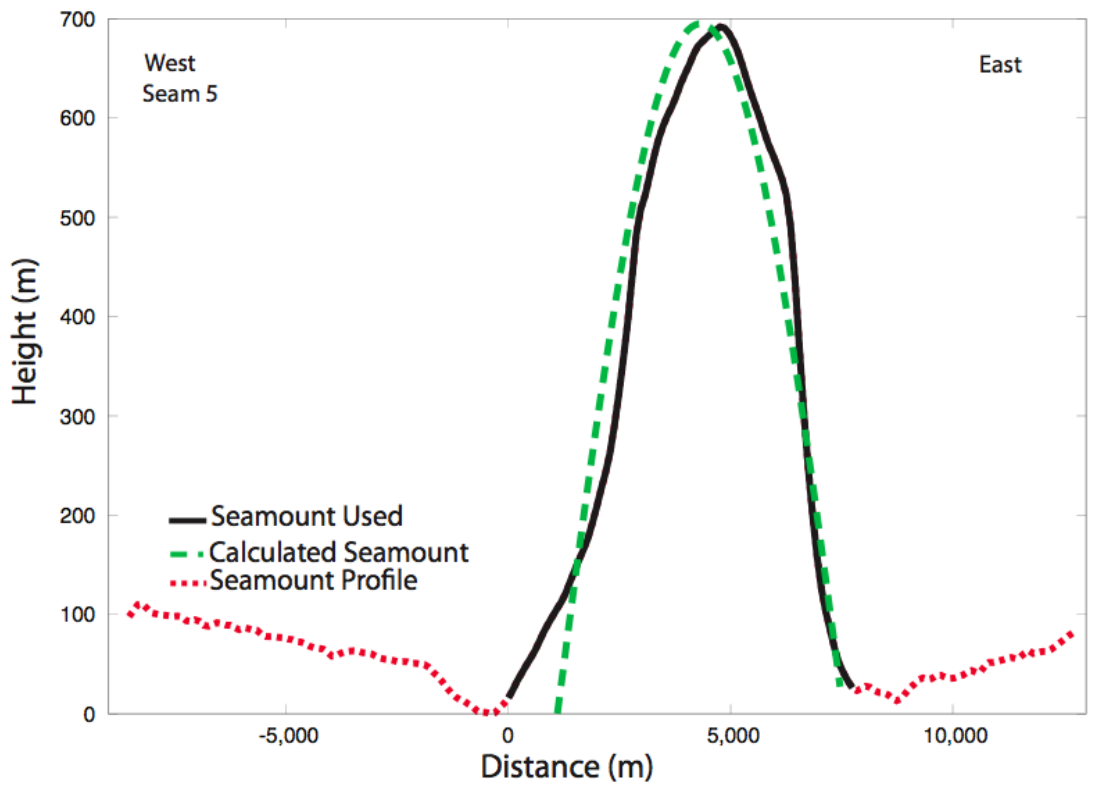


Figure B.5

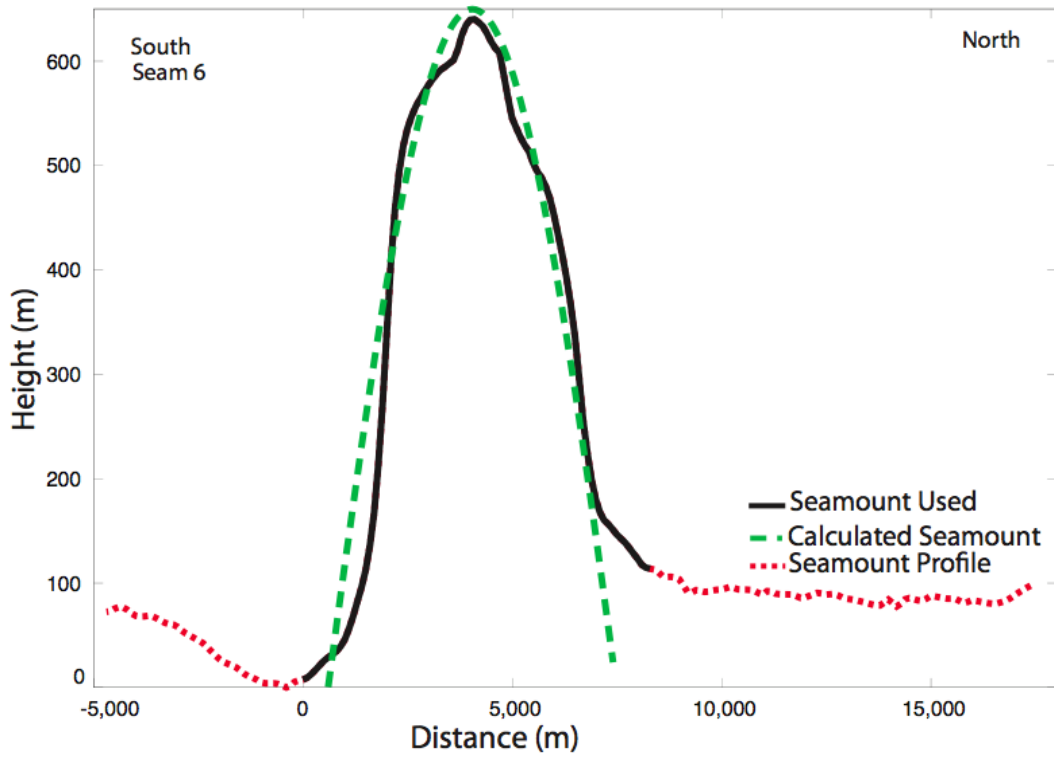
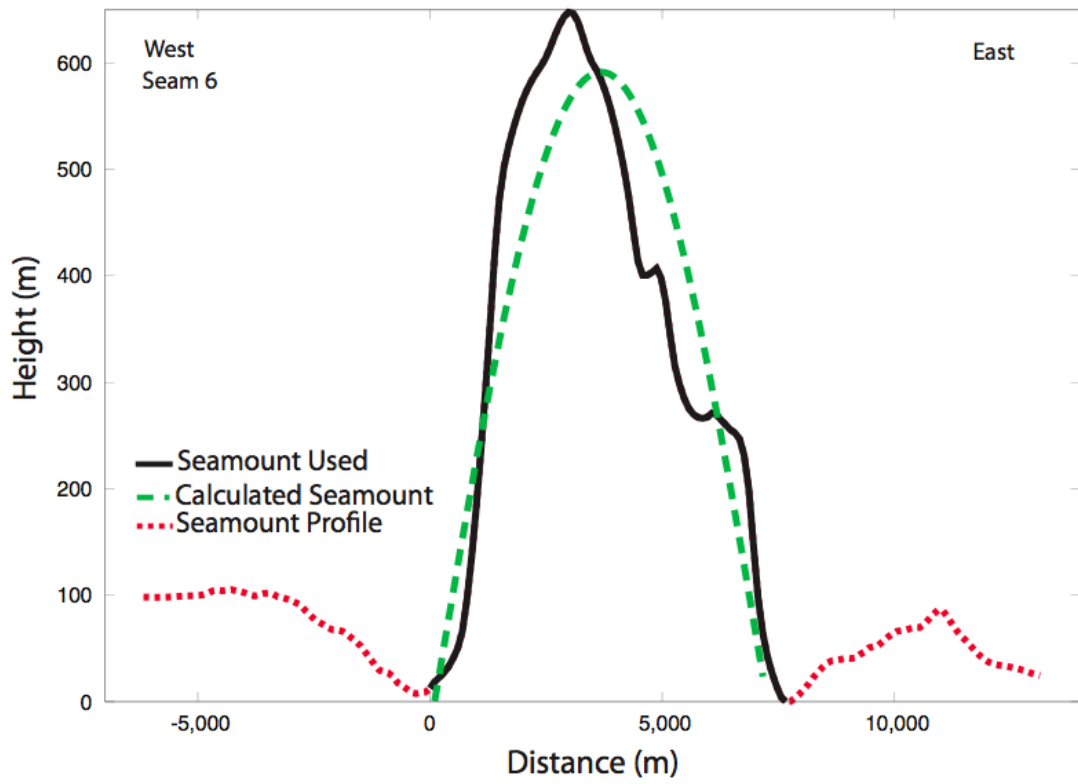


Figure B.6

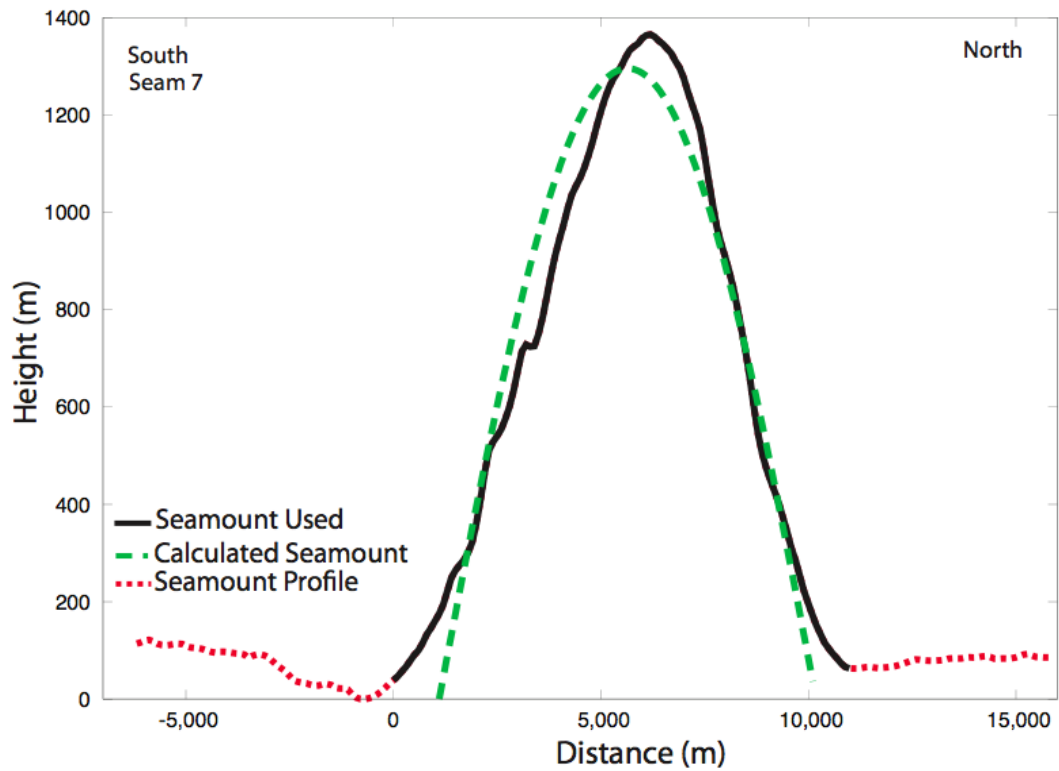
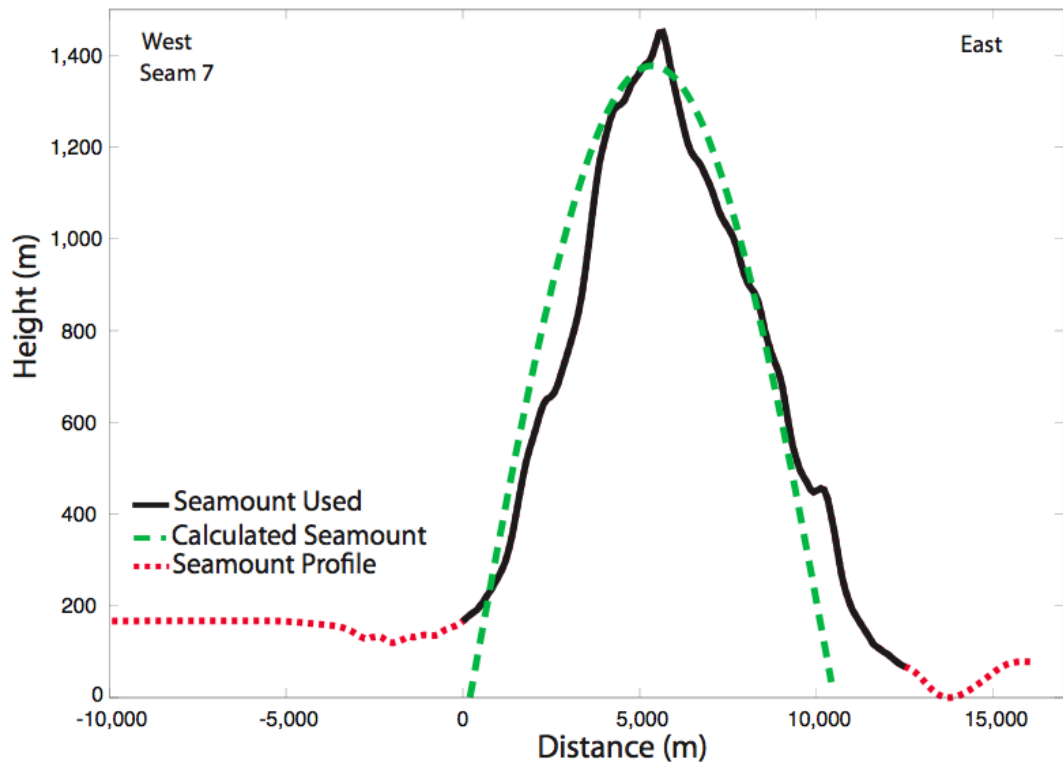


Figure B.7

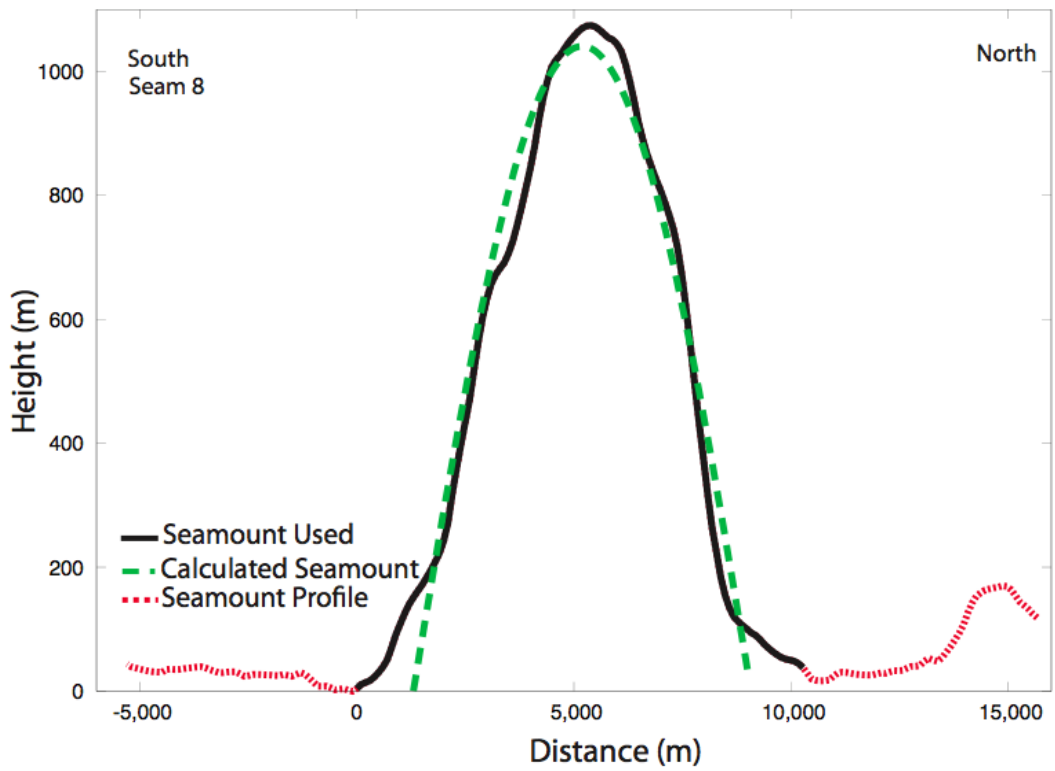
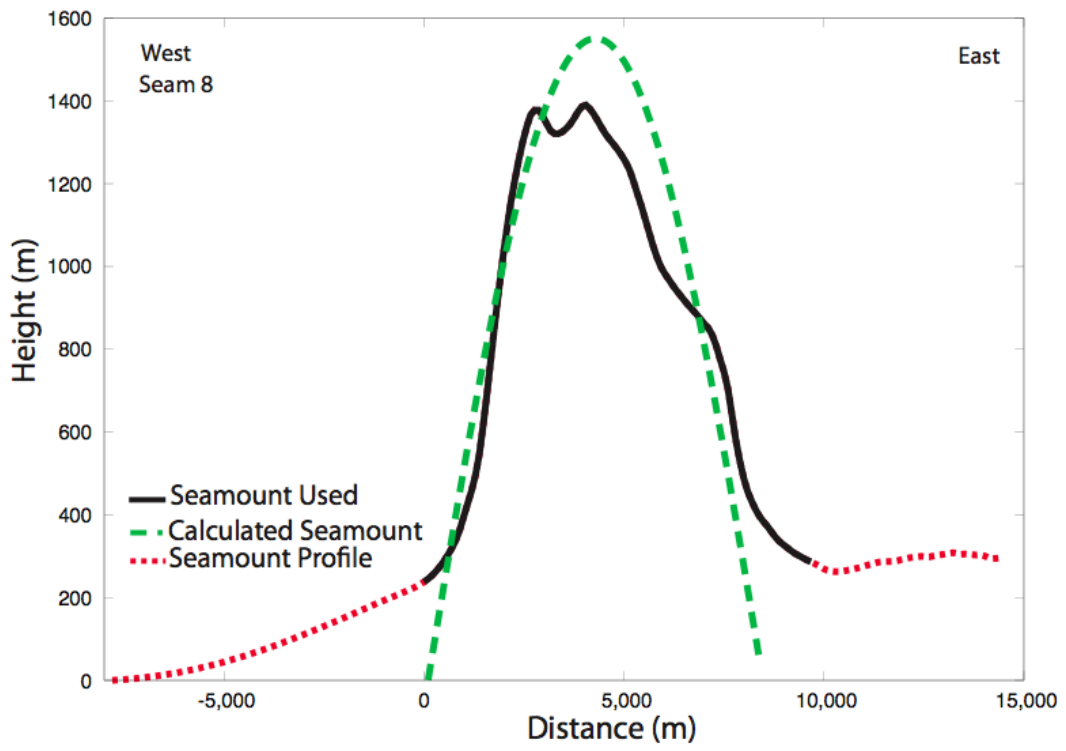


Figure B.8

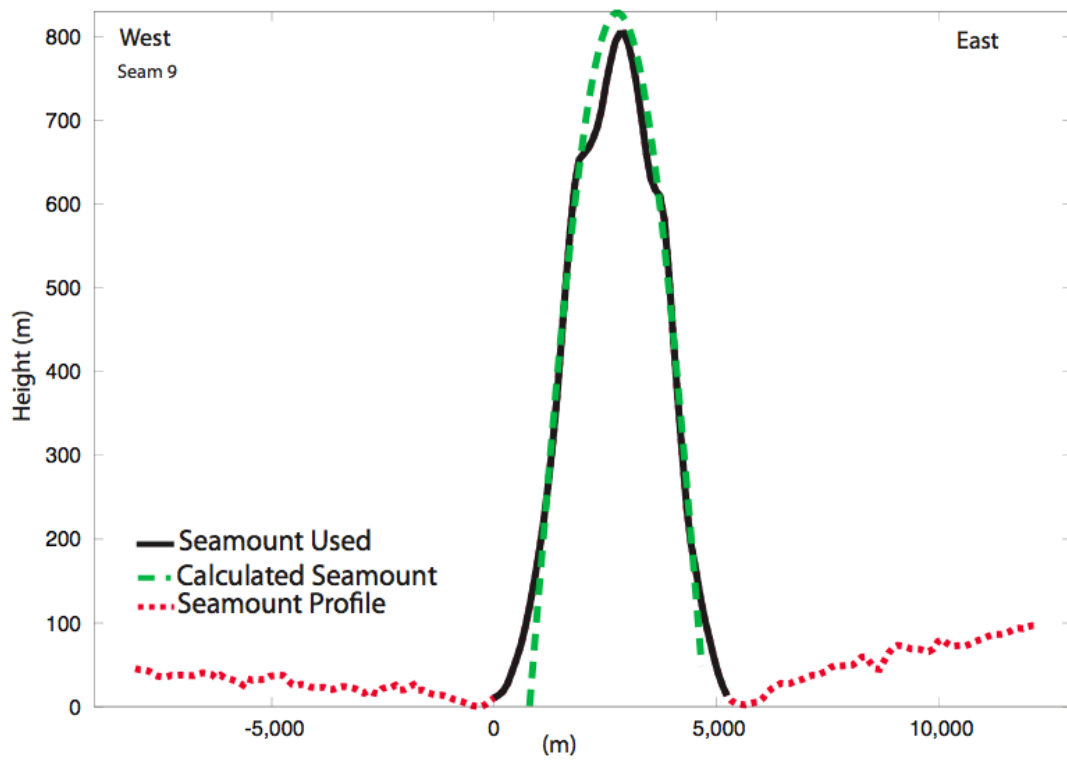


Figure B.9

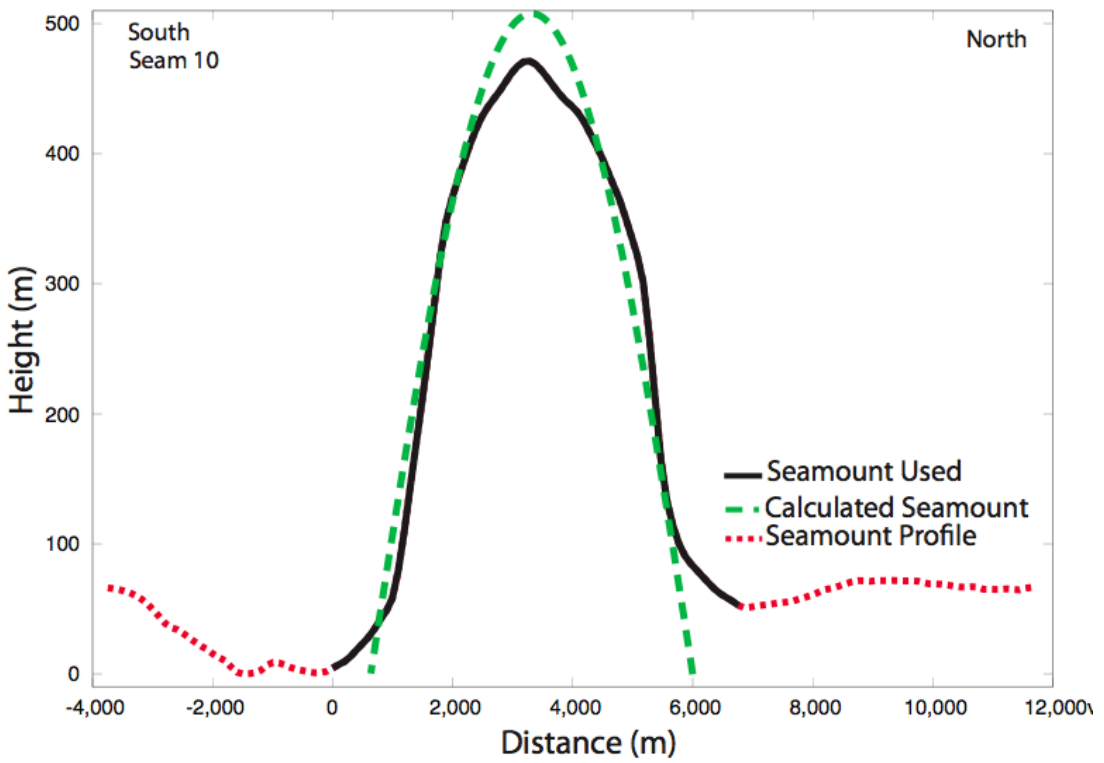
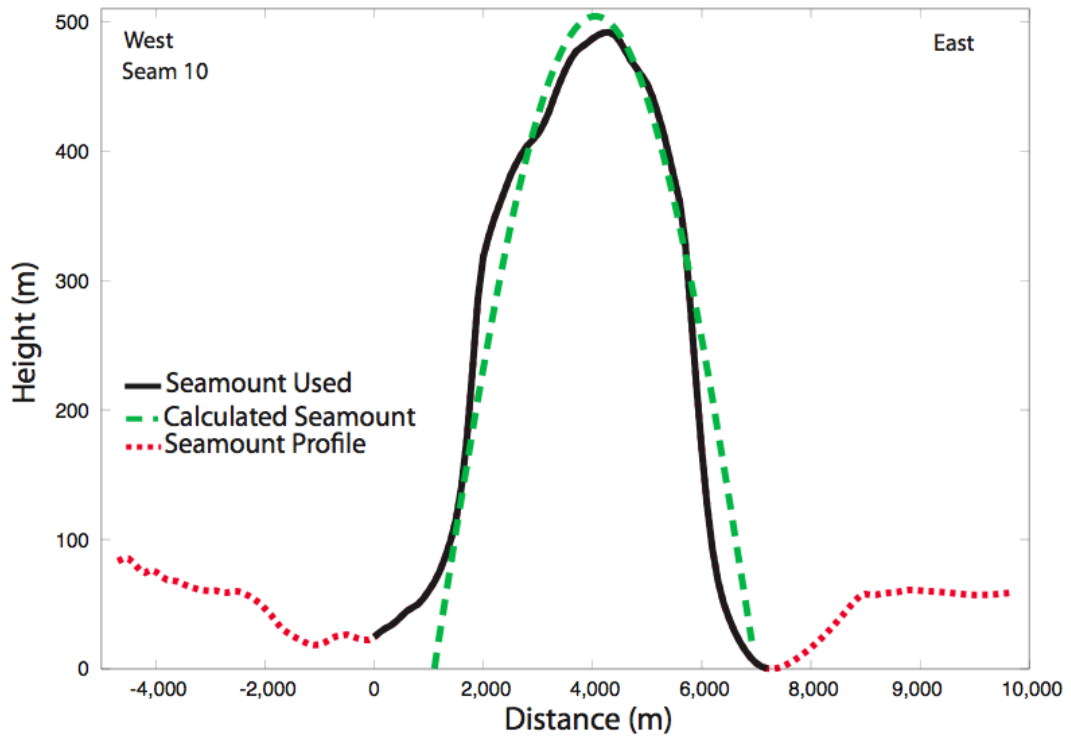


Figure B.10

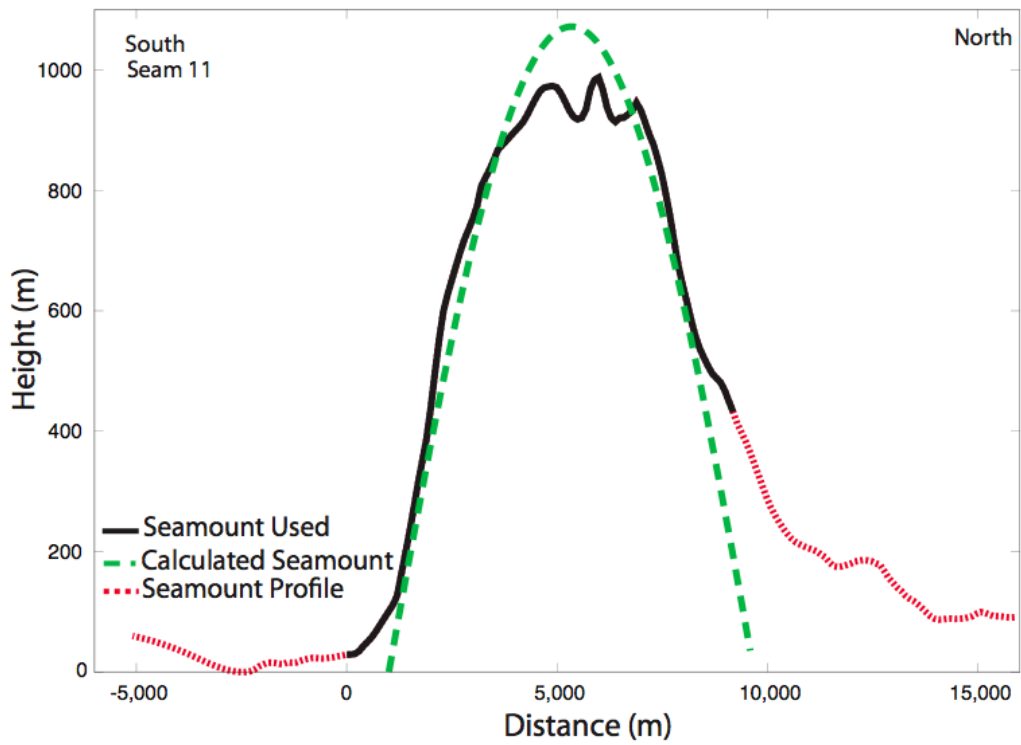
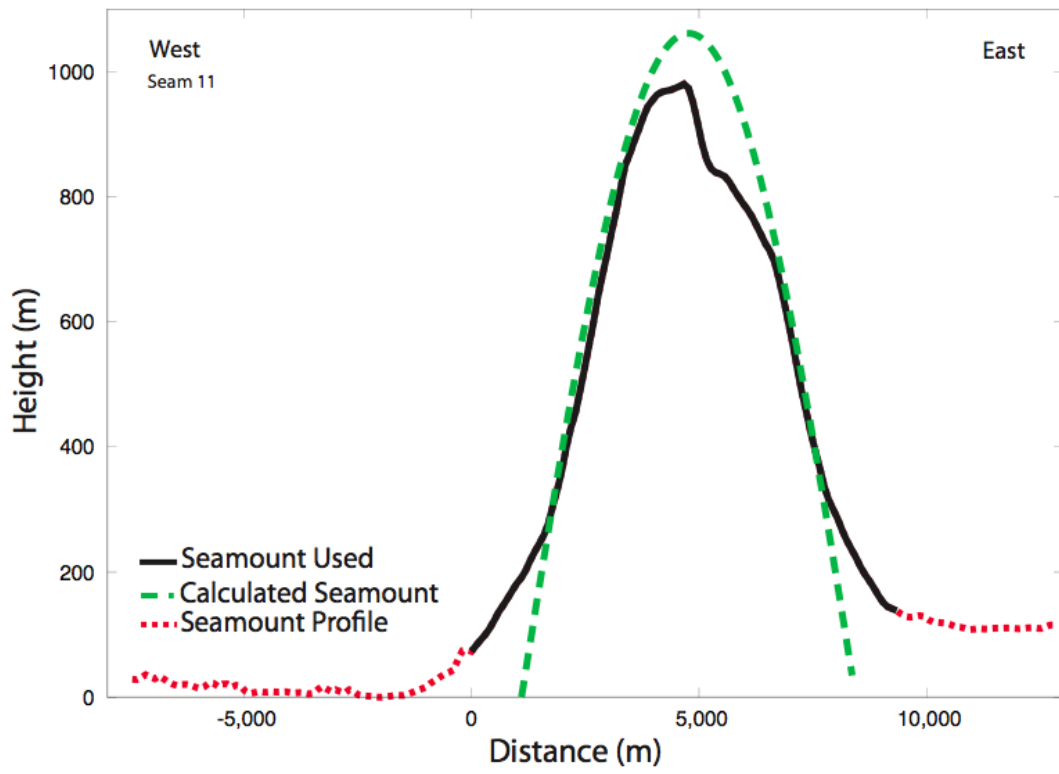


Figure B.11

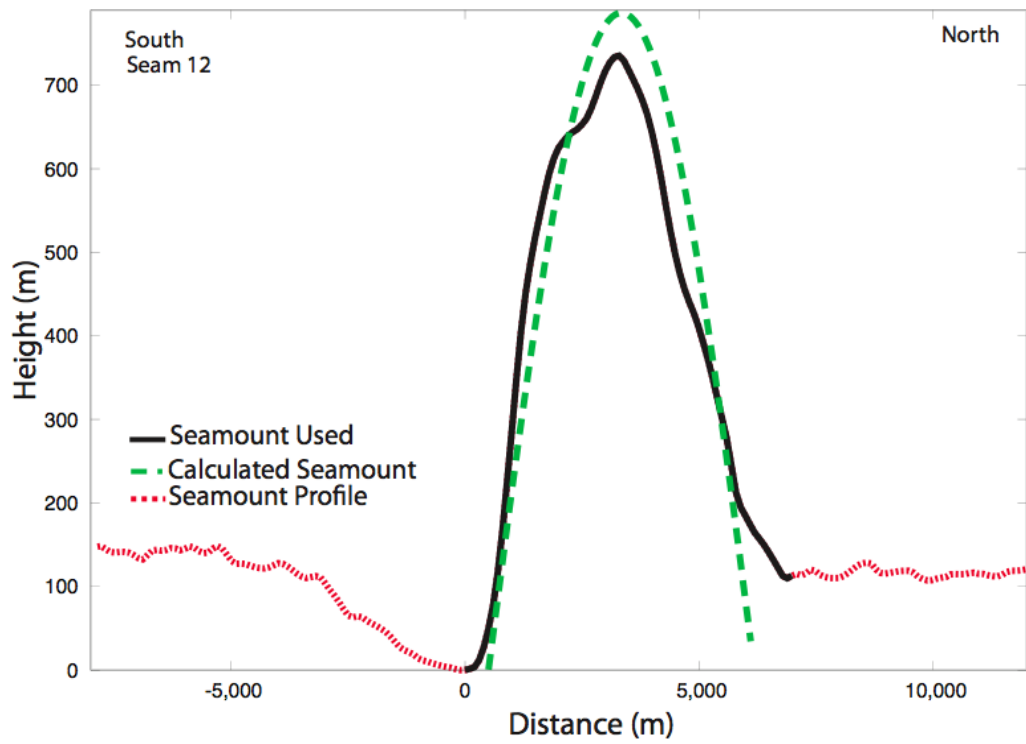
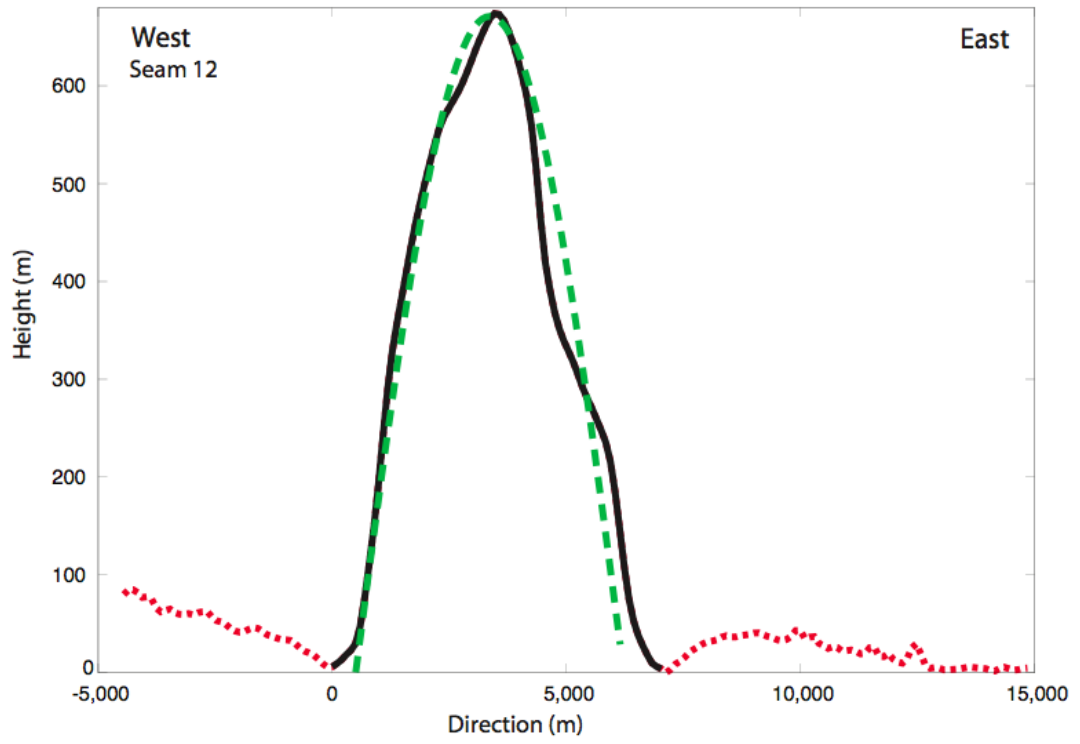


Figure B.12

APPENDIX C

Figures of seamounts used for calculation of the elastic thickness. Area under curves (green dashed and solid black) are within 1% of each other.

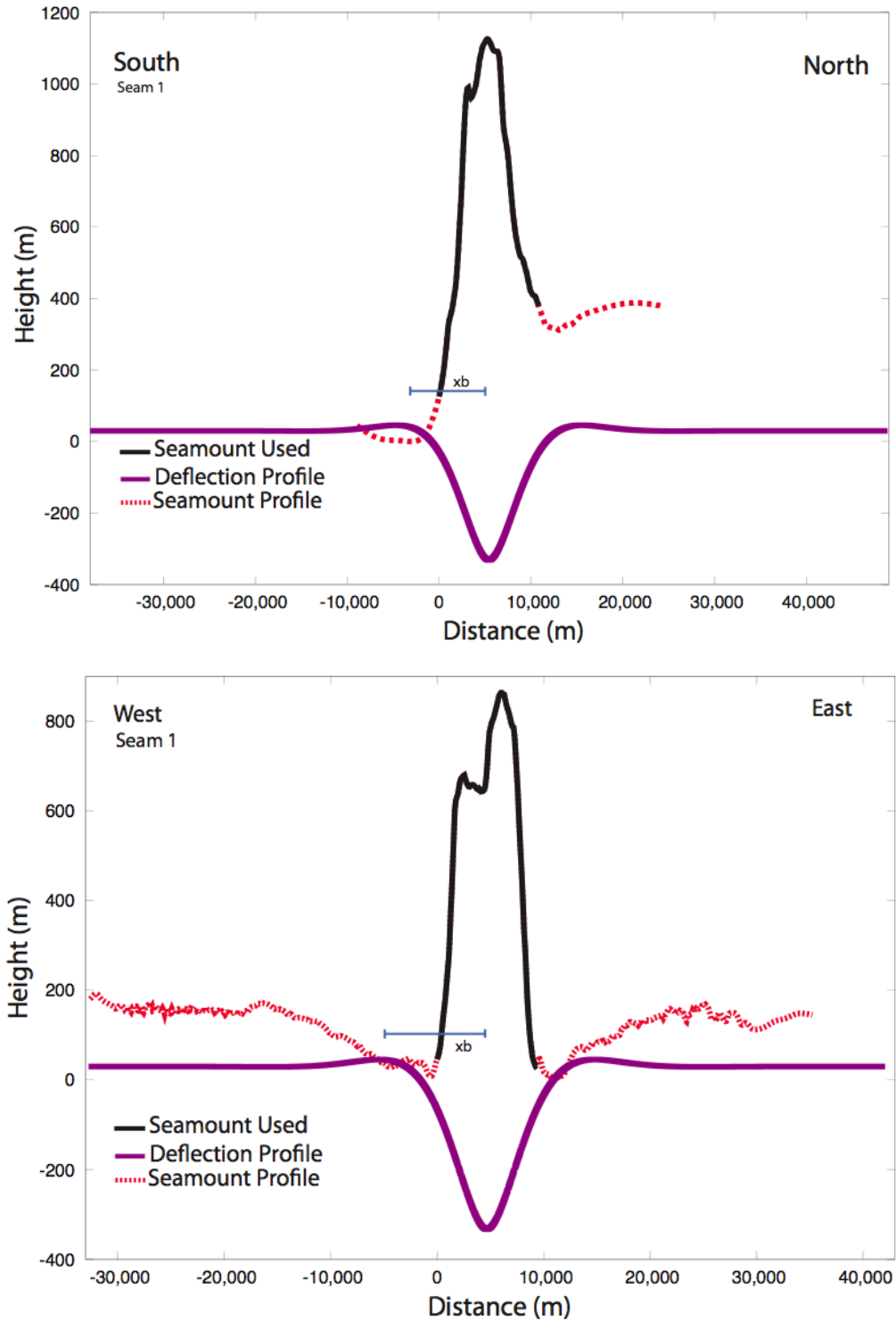


Figure C.1

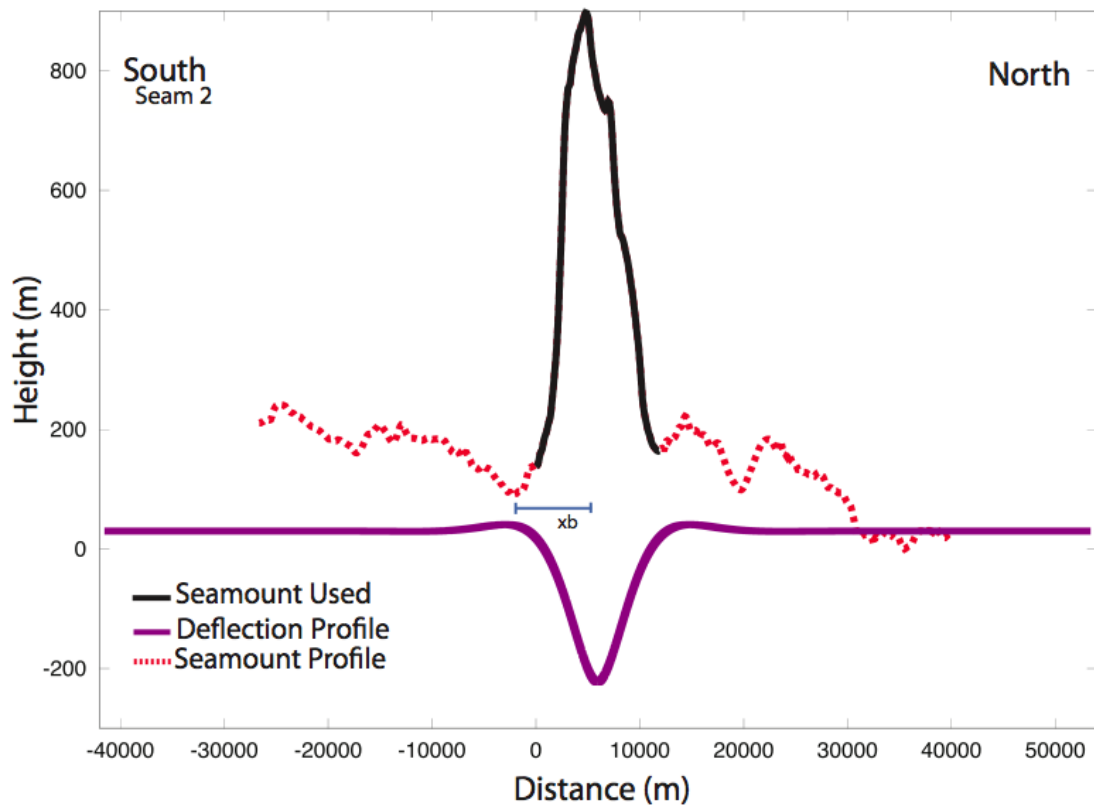
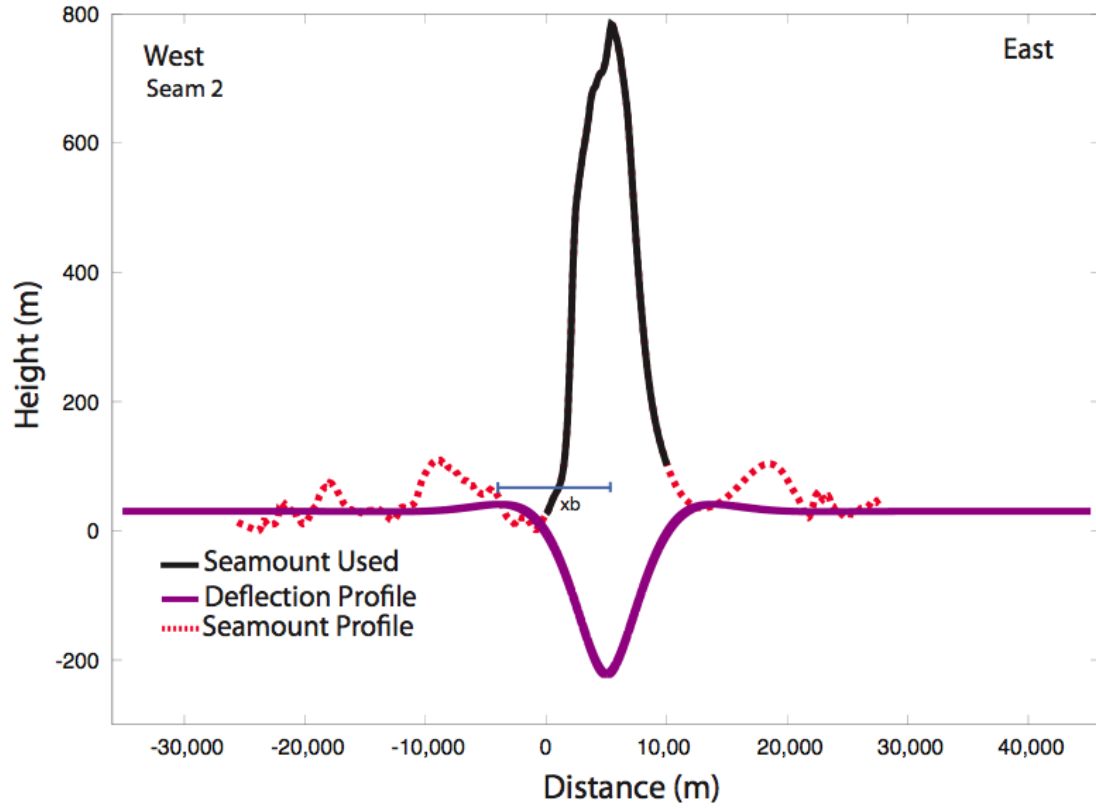


Figure C.2

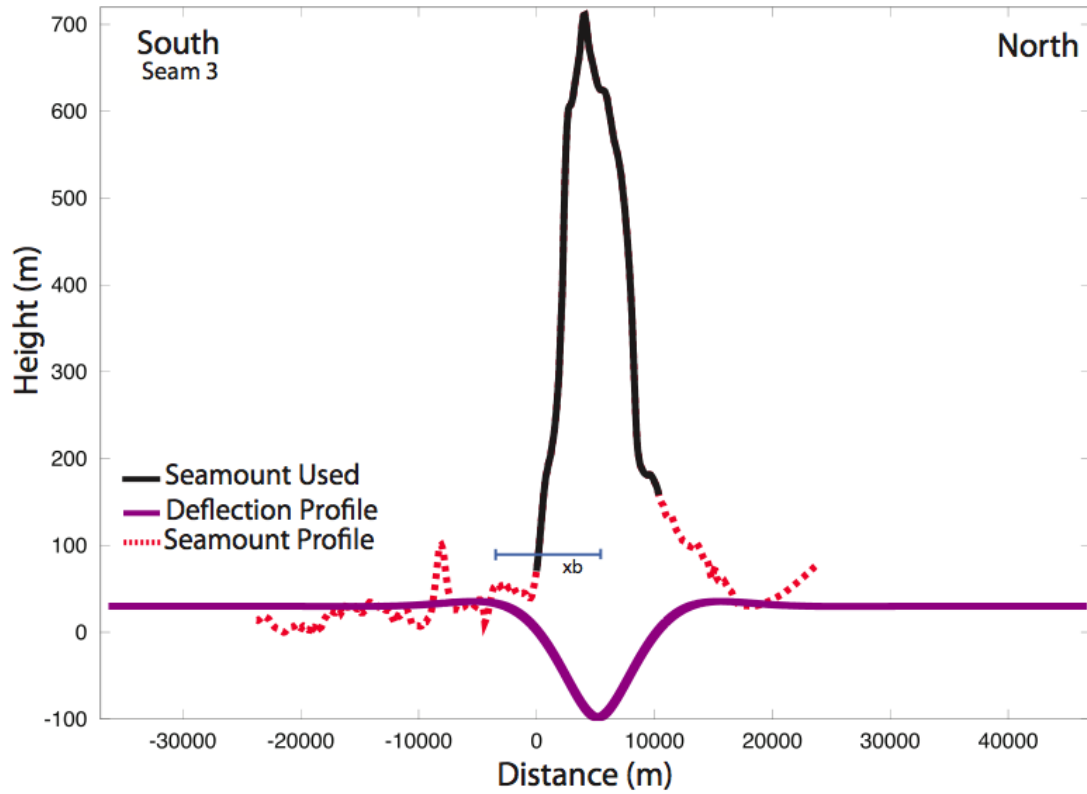
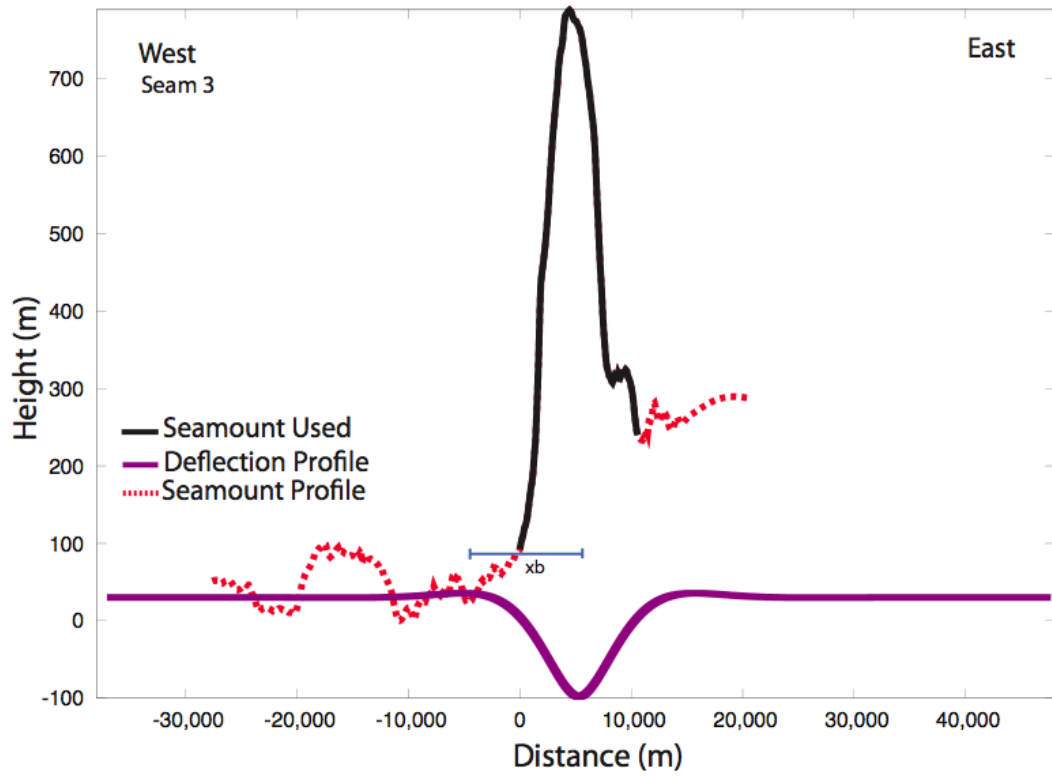


Figure C.3

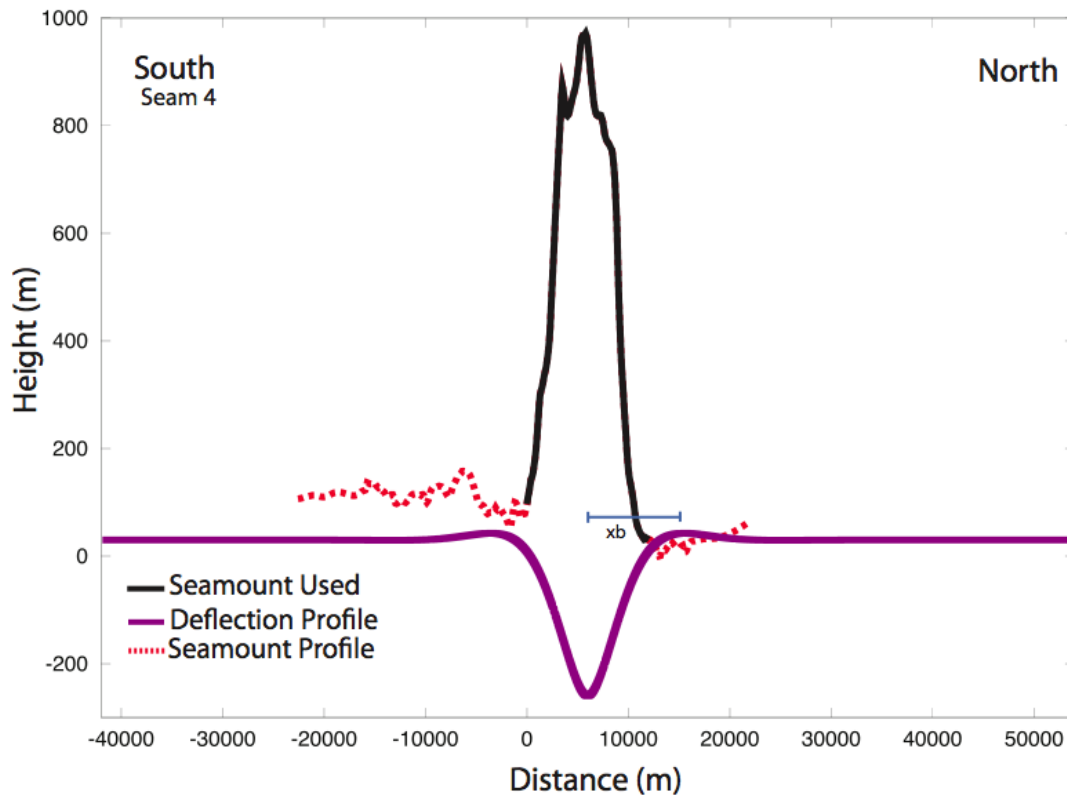
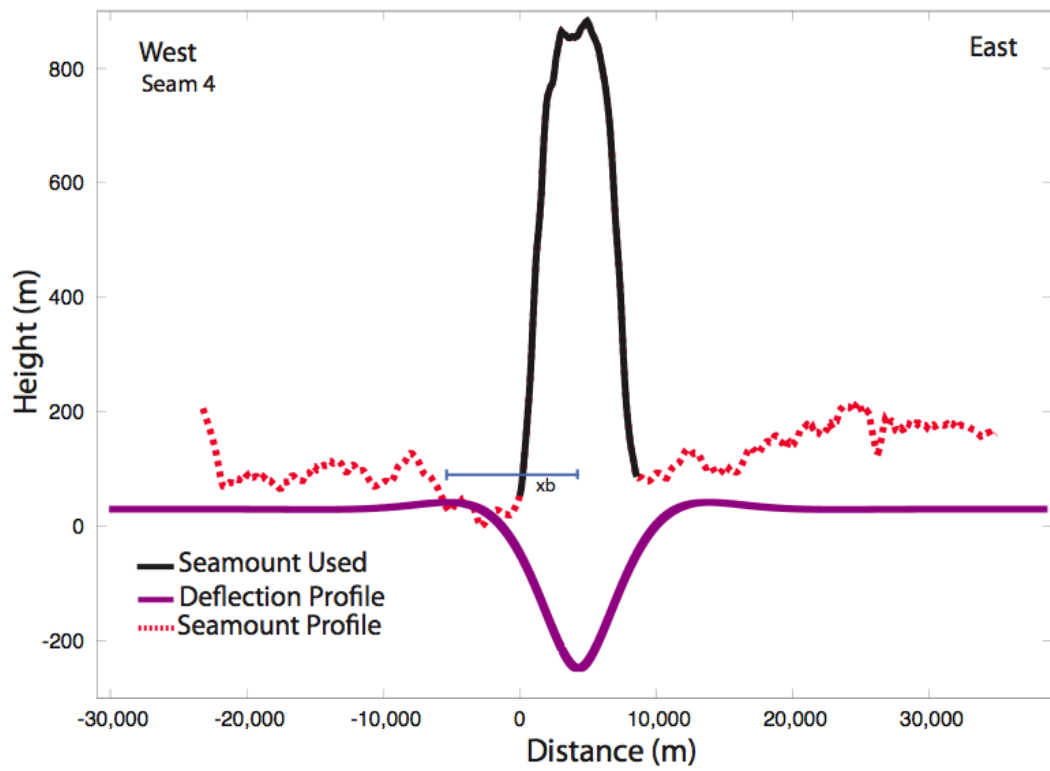


Figure C.4

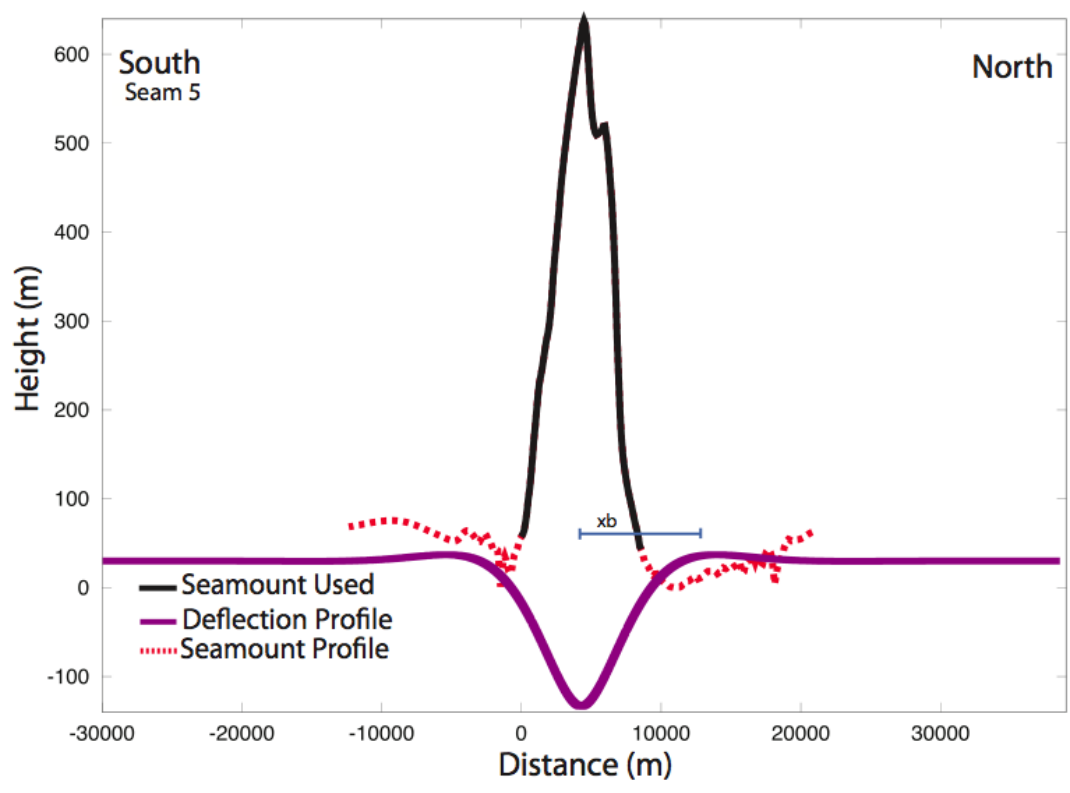
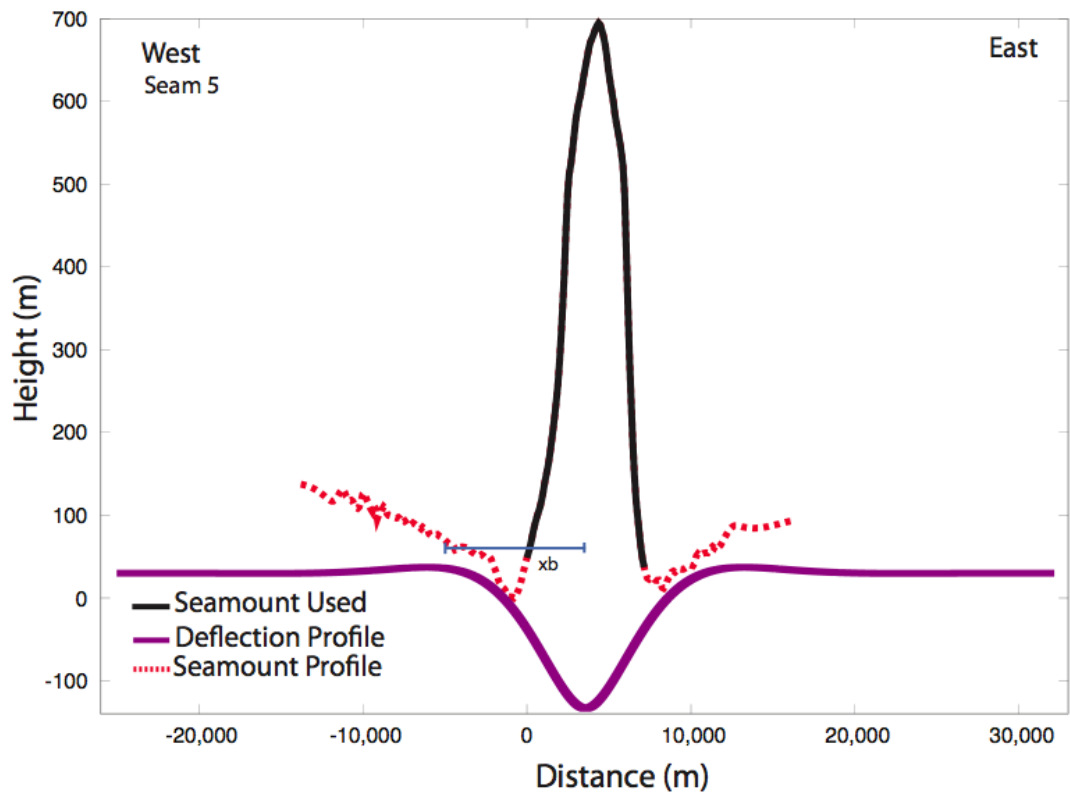


Figure C.5

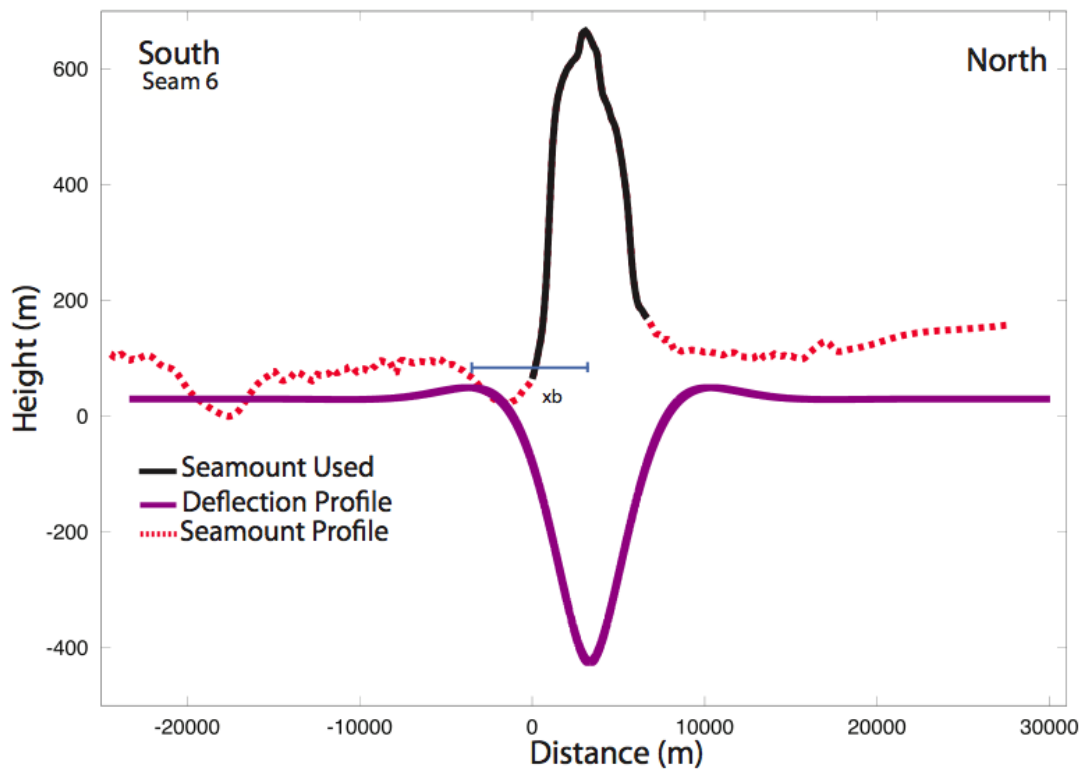
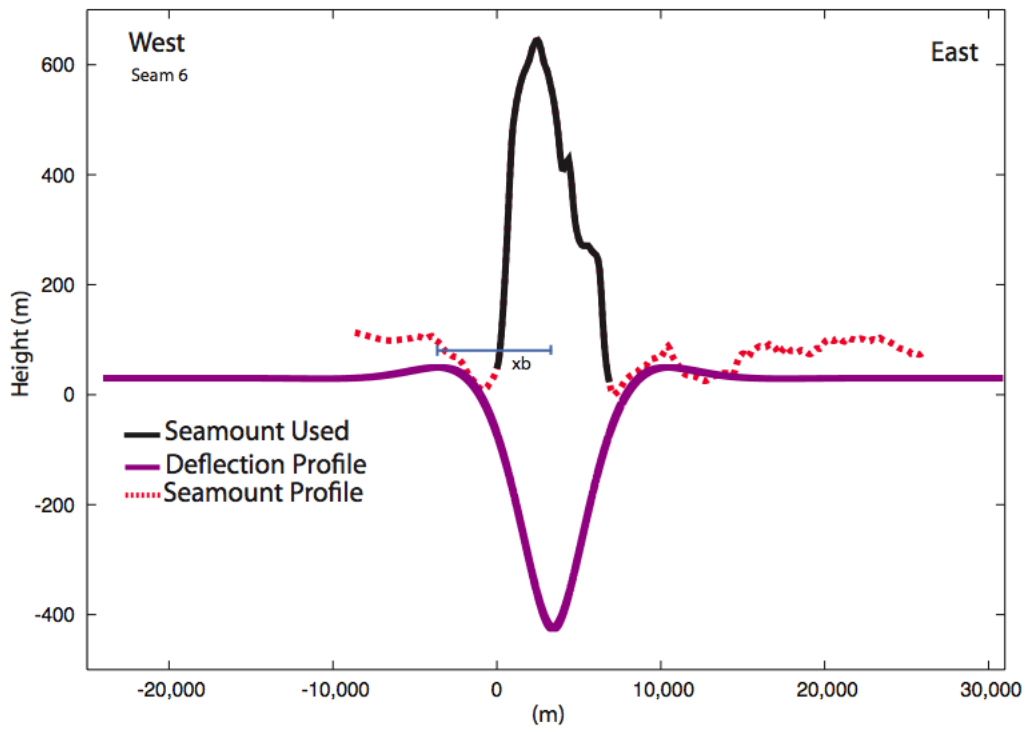


Figure C.6

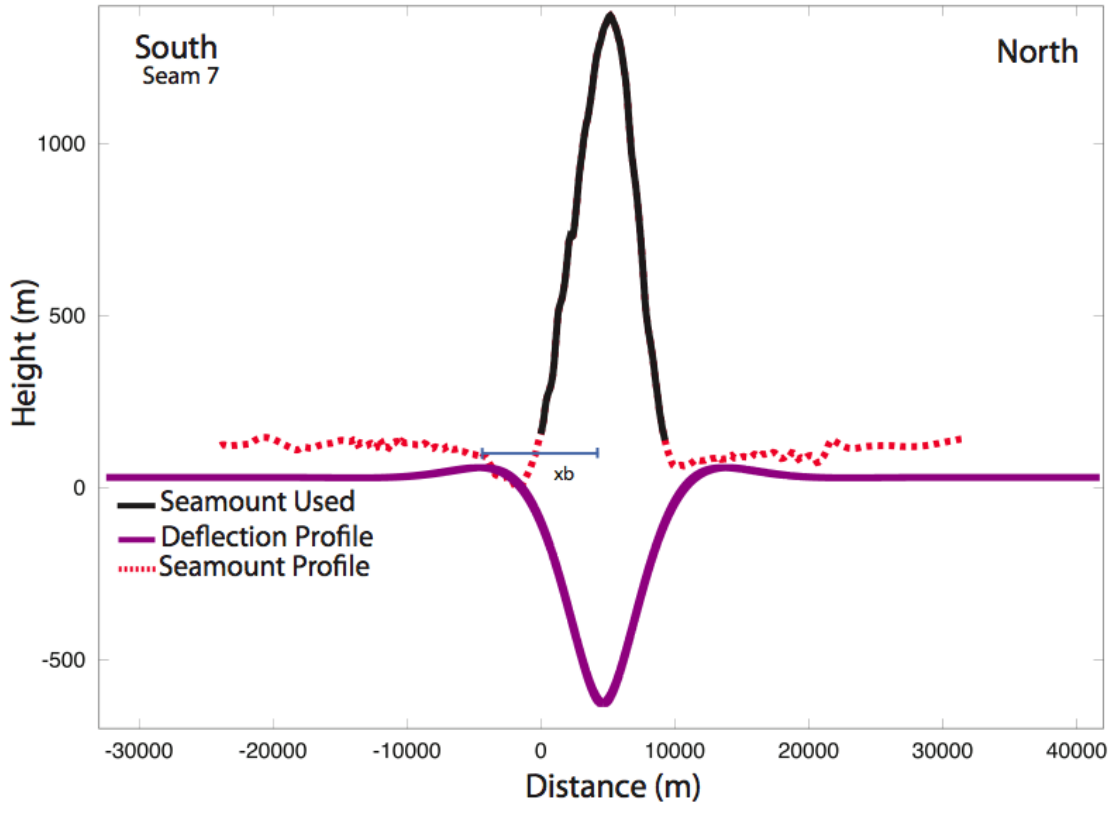
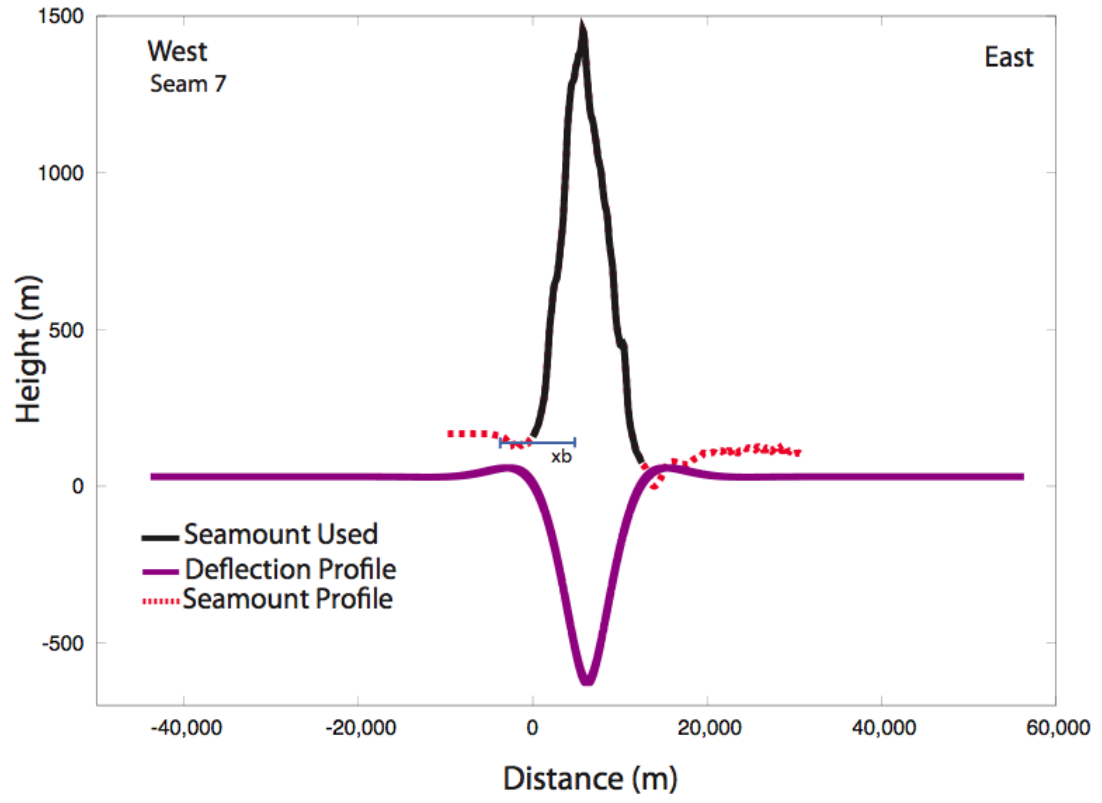


Figure C.7

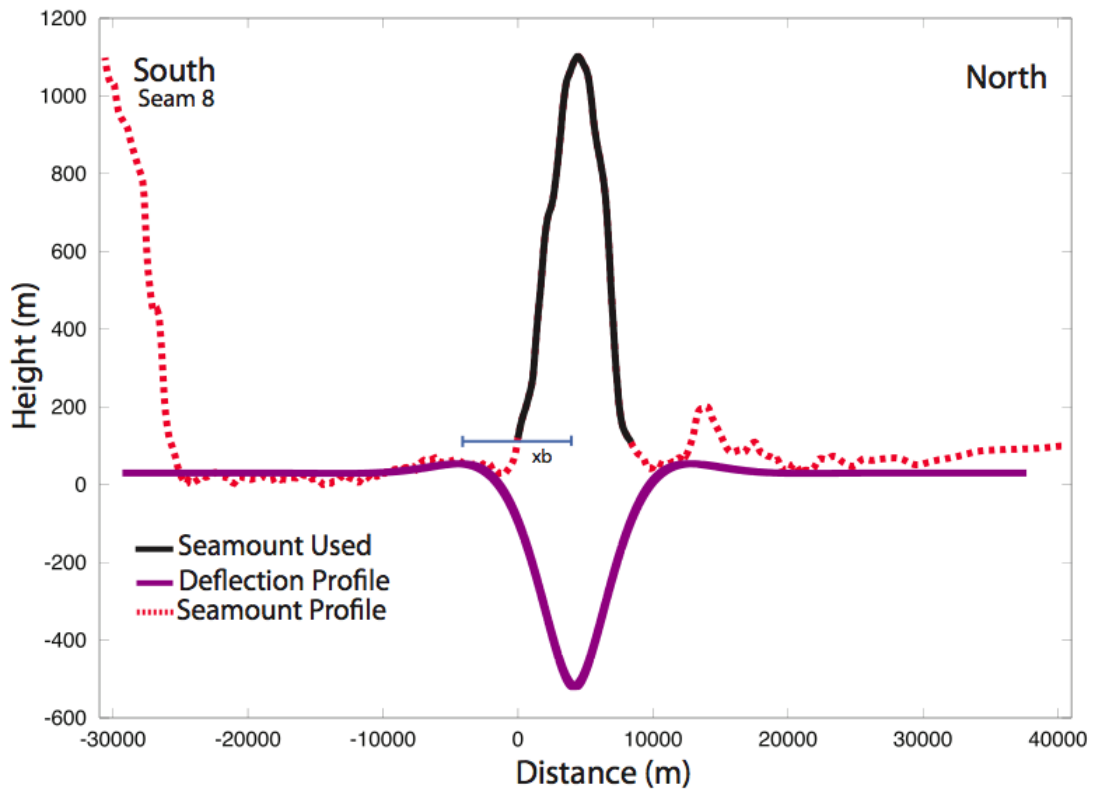
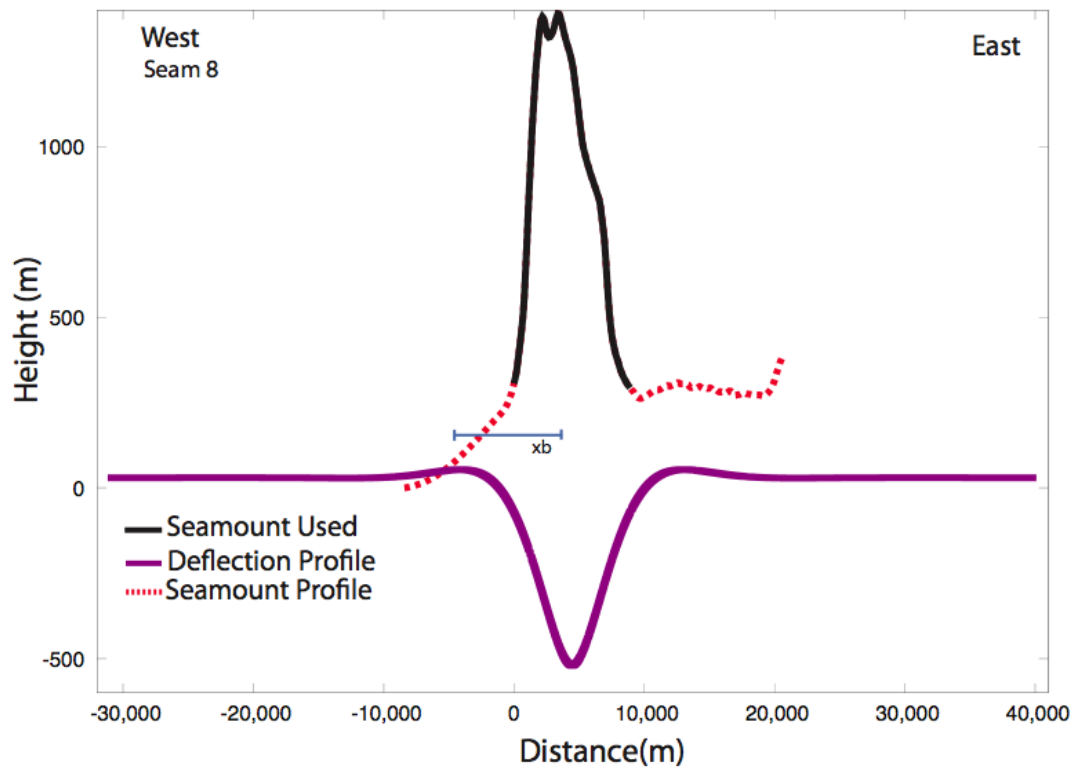


Figure C.8

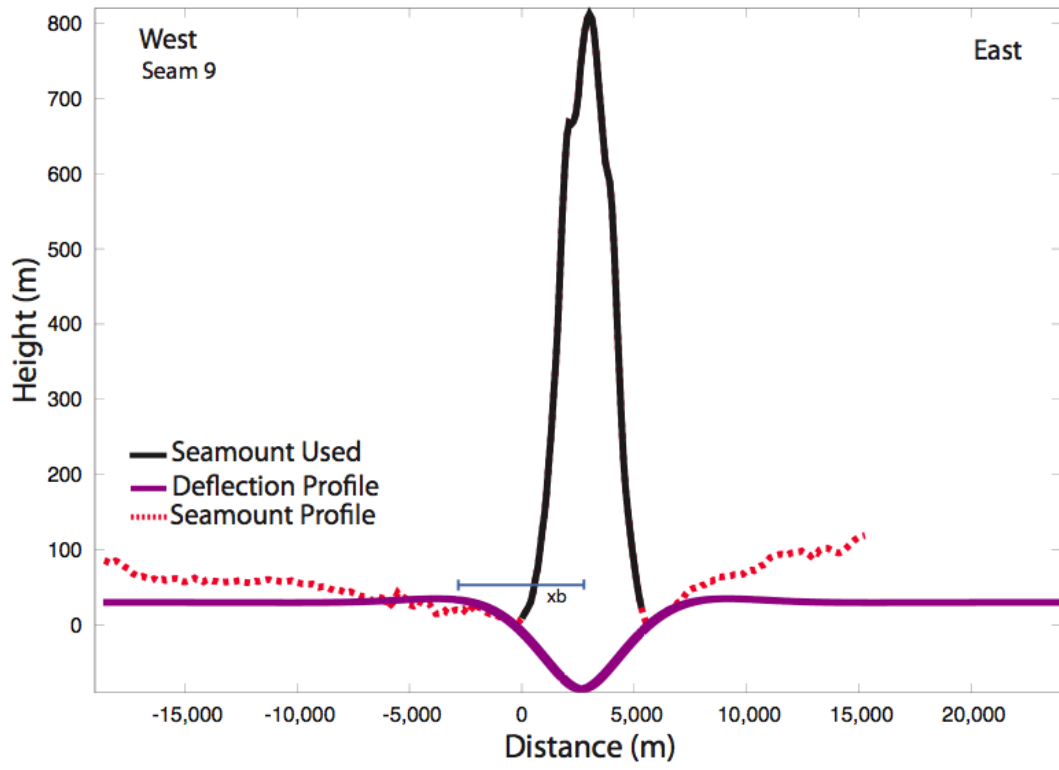


Figure C.9

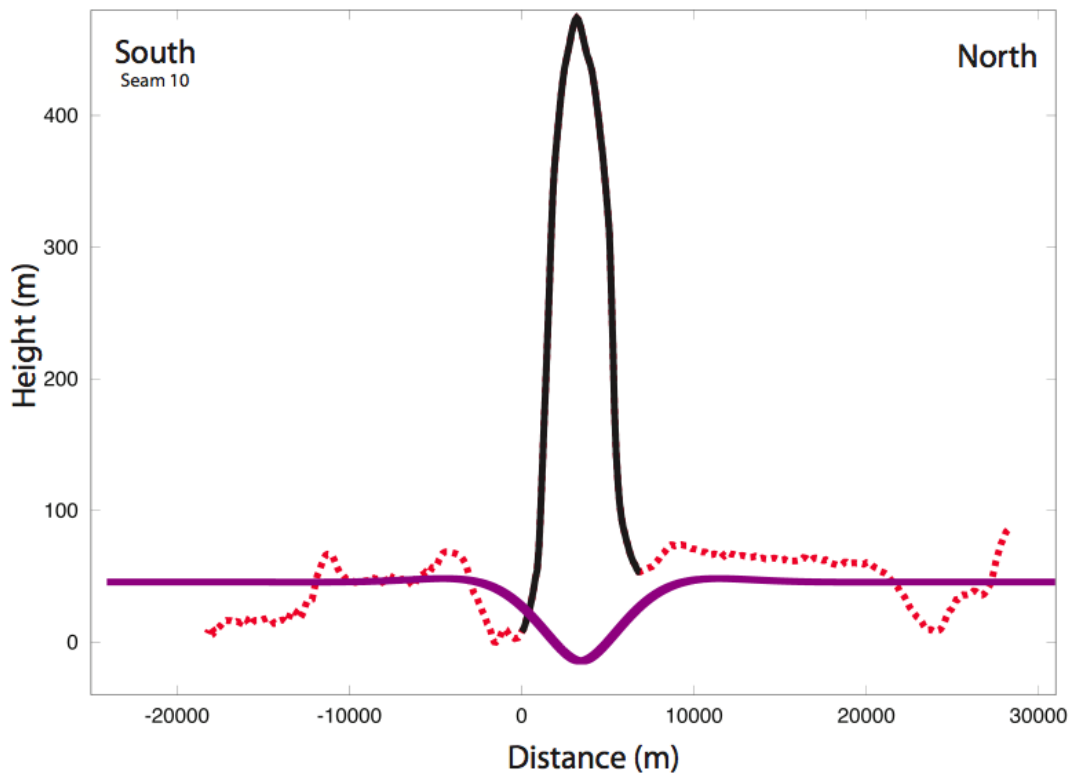
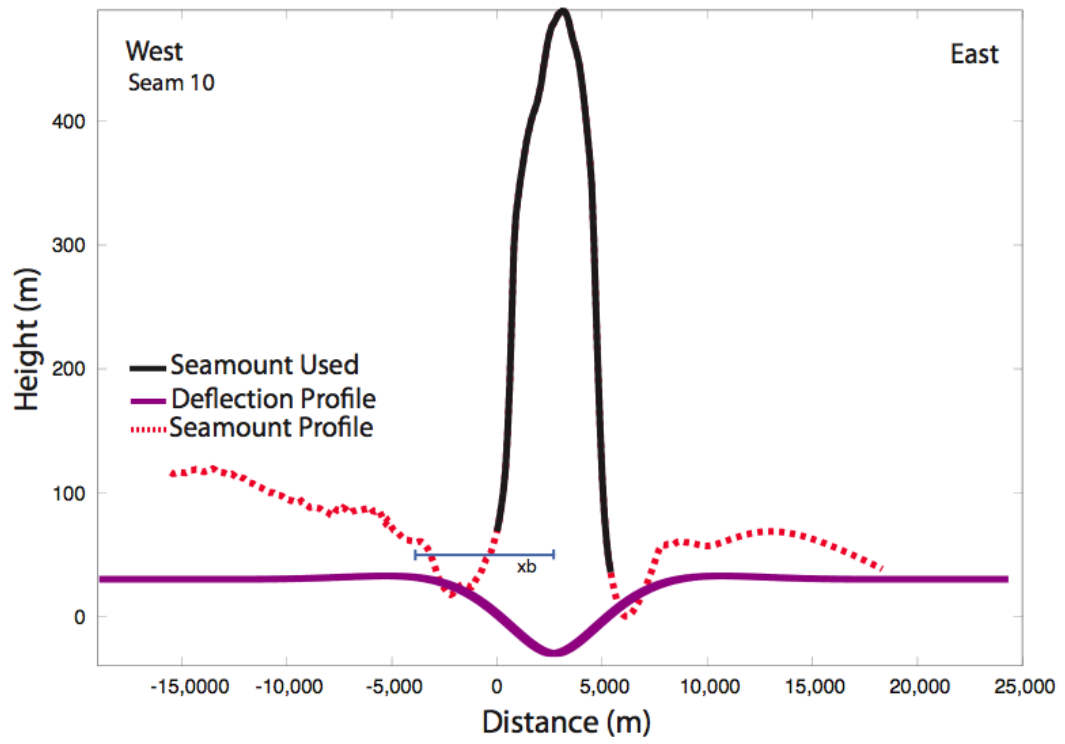


Figure C.10

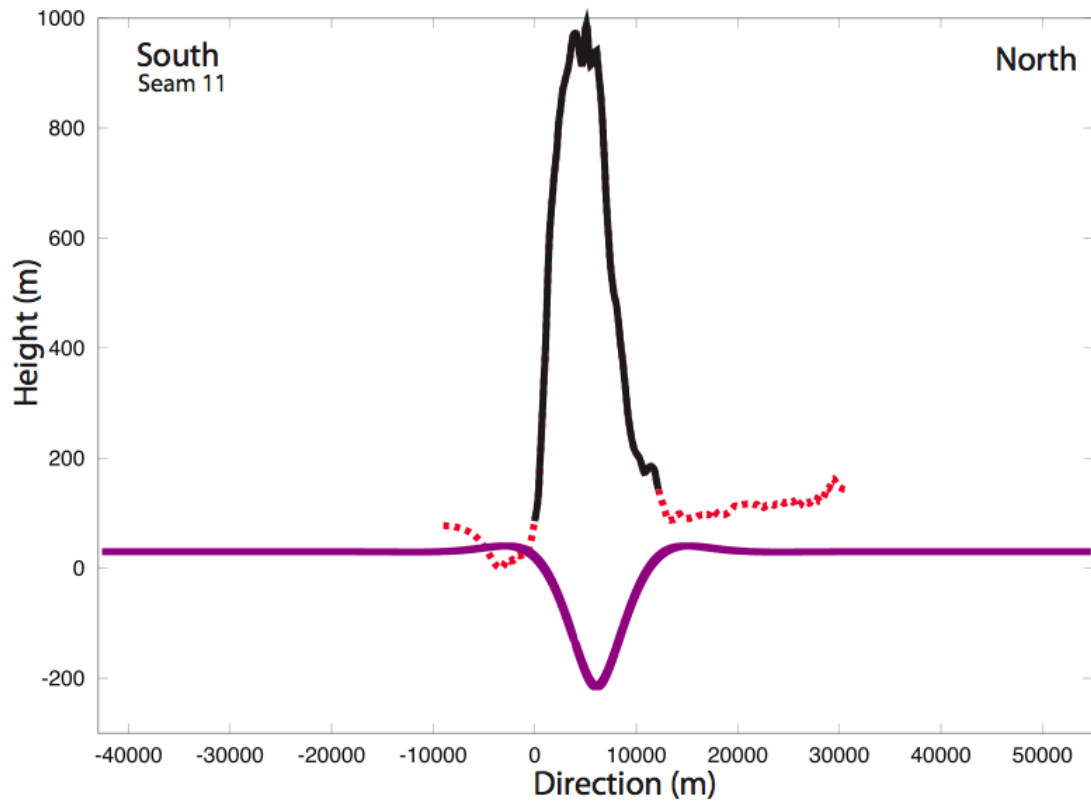
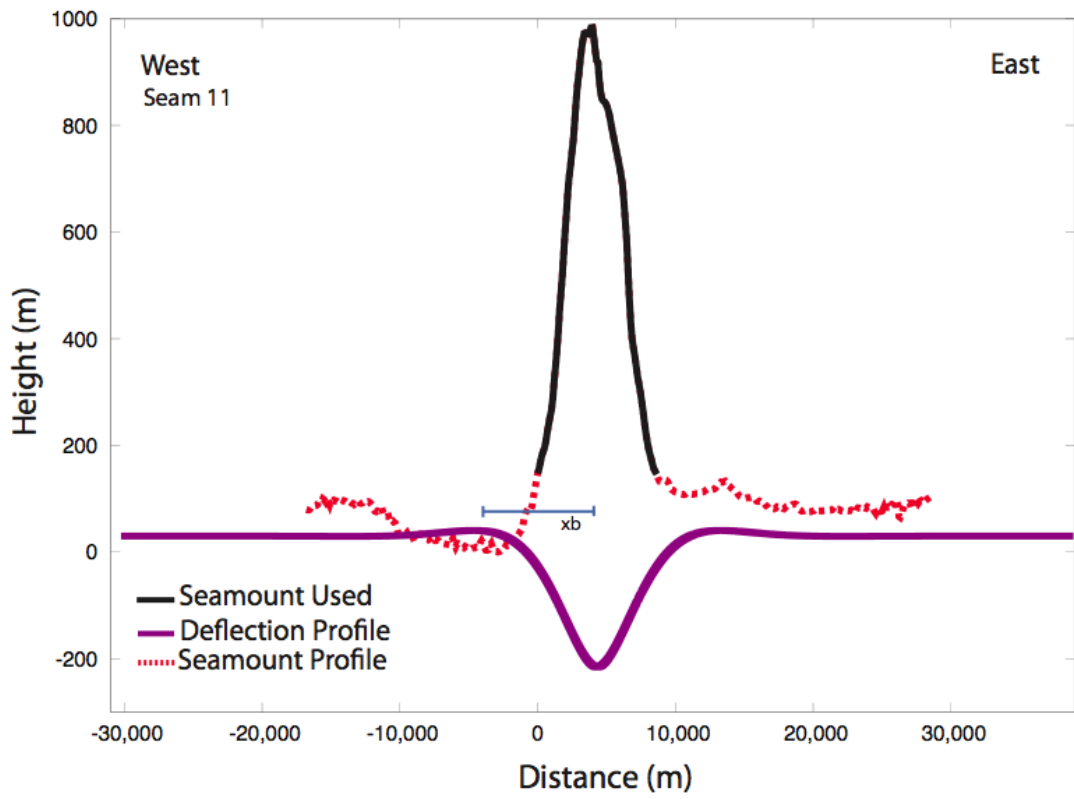


Figure C.11

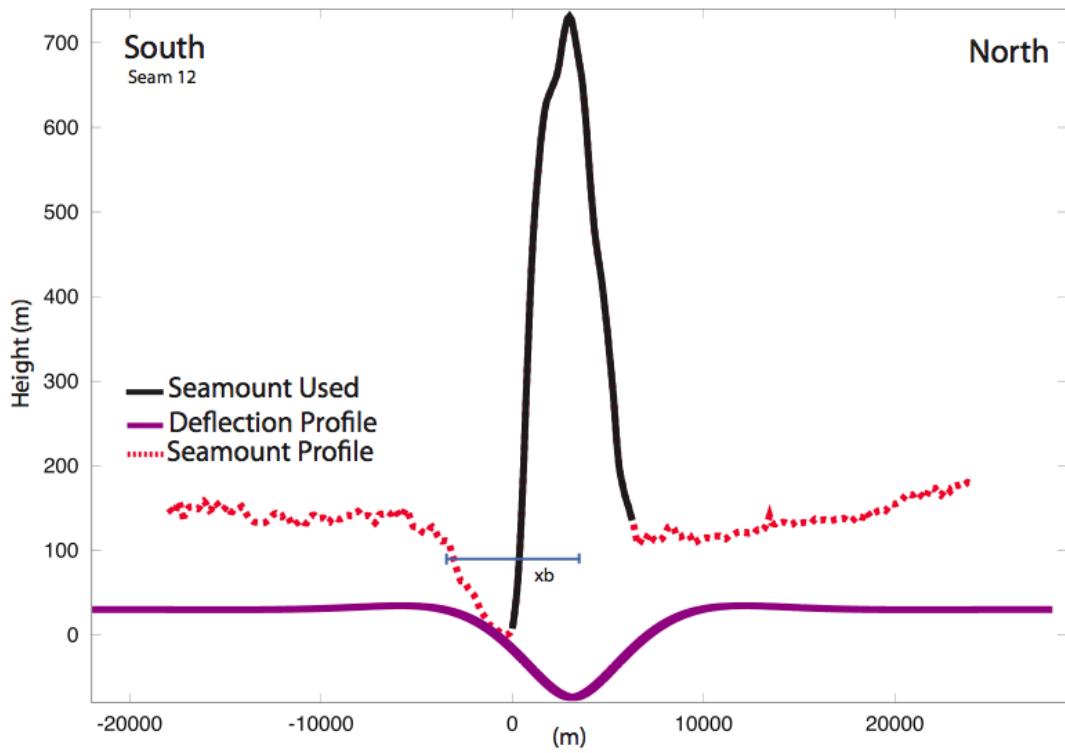
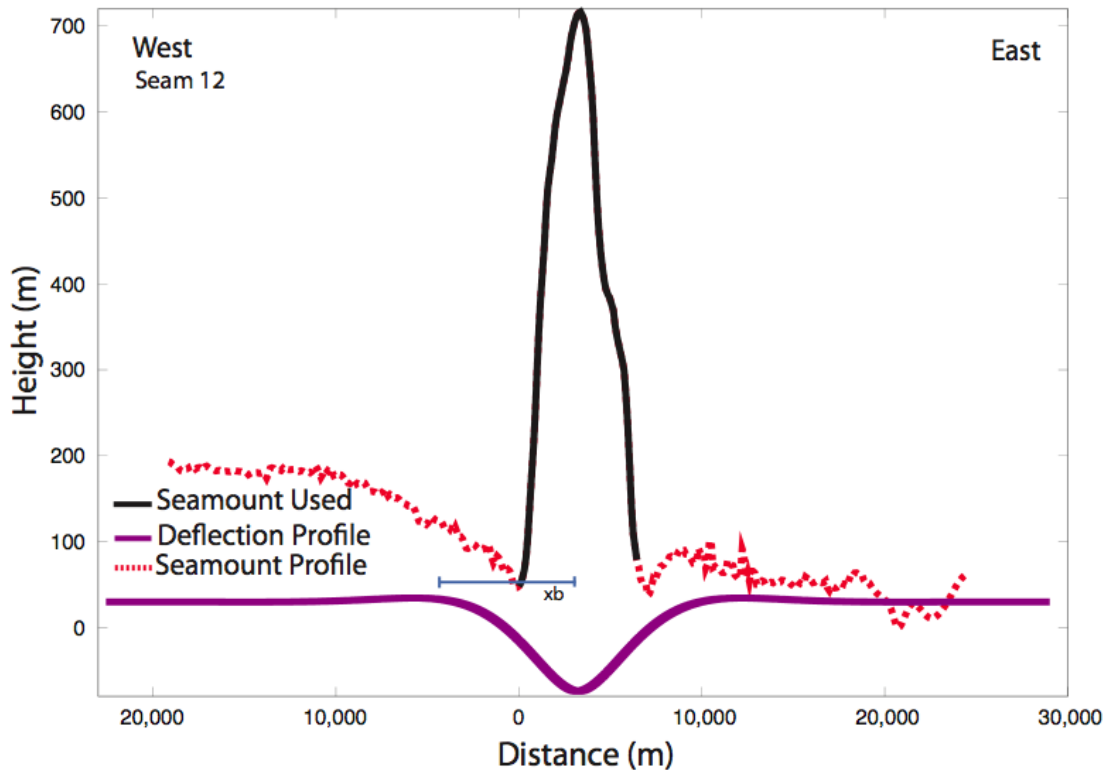


Figure C.12

Appendix D

Tables showing the most important parameters observed and calculated from seamount geomorphology.

Seamount	Lat	Lon	h_o (m)	x_b (m)	w_o (m)	Seamount Shape
1	27.48	147.89	1029	10130	363	Elliptical
2	27.63	149.87	827	8893	252	Circular
3	28.30	150.58	854	10423	128	Circular
4	28.05	152.03	952	9550	290	Circular
5	28.65	154.22	694	9672	163	Elliptical
6	28.75	154.93	591	7015	455	Elliptical
7	28.56	154.83	1377	9145	657	Circular
8	28.13	154.67	1551	8590	550	Elliptical
9	29.83	155.52	828	6490	115	Circular
10	29.39	155.54	504	7991	60	Circular
11	28.52	155.38	1061	8978	245	Circular
12	28.44	155.13	671	6848	104	Circular

Table D.1

Seamount	V (km³)	T_e N-S (m)	T_e E-W (m)	T_e Average (m)
1	22.85	3630	2685	3158
2	13.71	3520	2295	2908
3	11.03	3160	2855	3008
4	18.50	3635	2570	3103
5	11.64	3410	2260	2835
6	12.80	1775	1470	1623
7	35.27	2860	3355	3108
8	26.23	2585	2645	2615
9	4.30	1605	1605	1605
10	3.46	2385	2585	2485
11	14.45	2910	2920	2915
12	7.14	2420	2295	2358

Table D.2